Materials and Devices for Photoelectrochemical and Photocatalytic Water Splitting

A thesis presented to University College London in partial fulfilment of the requirements of the degree of Doctor of Philosophy

Penelope Carmichael

Supervised by

Professor Ivan Parkin

Materials Chemistry Centre, UCL, Department of Chemistry

2015

Declaration

I, Penelope Carmichael, confirm that the work presented in this thesis is my own. Where information has been derived from other sources, I confirm that this has been indicated in the thesis.

For my mother.

"If you want to have good ideas, you must have many ideas. Most of them will be wrong. What you have to learn is which ones to throw away".

-Linus Pauling

Abstract

This thesis is concerned with the development of materials and devices for photo-driven water splitting. In the introductory chapter, a comprehensive review of photo-driven water splitting is given and the concept of device design is investigated. Three different systems for photo-driven water splitting were then explored over three experimental chapters. The first experimental chapter explores the application of titanium dioxide and anion-doped titanium dioxide in a water splitting photodiode. Non-doped, B-doped and B,N-doped TiO_2 films deposited using atmospheric pressure chemical vapour deposition (APCVD) on steel and fluorine doped-tin oxide substrates were investigated. The physical properties and photocatalytic water splitting activities of the films were then compared. In the second experimental chapter of this thesis, the application of hematite in a PV/ PEC tandem device is explored. Hematite films were deposited using a low-temperature CVD process onto triple junction solar cells. The tandem device was then assessed for its solar-to-hydrogen efficiency using photoelectrochemical methods. The final experimental chapter explores a relatively neglected III-V semiconductor, boron phosphide. BP powders were synthesised using a metathesis reaction and their photocatalytic water reduction activity assessed. The thesis concludes with a summary of key findings of the experimental work conducted along with potential avenues for further research.

Acknowledgements

Firstly I would like to thank my supervisor, Professor Ivan Parkin, whom I consider not only a mentor, but also a friend. Your support has helped me greatly, especially in the last year. I would also like to thank my second supervisor Jawwad Darr and all of my collaborators on the project 'Nanocrystalline Water Splitting Diodes II'. I would also like to thank Dr Andreas Kafizas for giving my thesis the 'once over'. I would especially like to thank my wonderful family. My parents: Janet and Greg Carmichael, whose unwaivering support and incredible strength has kept me going. My mother is truly a source of inspiration and her strength unrivalled; I am lucky to have her. My big sisters Nicola and Louise Carmichael, who are my 'better thirds'. My husband Ben Rogers, you are my rock and I couldn't have got this far without you. Finally I would like to thank all of my lab mates (who are too many to name but all amazing!) and the technical staff in the department. You have all made my PhD experience what it has been. From you all I have received not only great advice but great friendship too, which I treasure.

Table of Contents

List of Tables

List of Figures

1 Introduction

The aim of this thesis was to explore three different systems for photo-driven water splitting. Two types of integrated photoelectrochemical array were explored in the first two experimental chapters of this thesis and a photocatalyst suspension in the last. This thesis will provide a deeper understanding of both material selection and device type for water splitting systems.

1.1 Global Energy Outlook

"We can no longer burn our way to prosperity". These are the words of Ban Ki-moon, the United Nations Secretary-General. His challenge, to provide universal access to modern energy services, to double the rate of global improvement in energy efficiency and to double global renewable energy consumption to 30% by the year 2030, is part of a UN initiative 'Sustainable Energy for All'.[1] Reliable and affordable access to energy has been a key driver of social and economic growth, yet of a global population of 7 billion people, 1.3 billion still lack access to electricity.

Where energy supply is plentiful the challenge is a different one. Of the 15 TW of power consumed annually, nearly 85 % is derived from fossil fuel sources, Figure 1.1.[2] The high energy density, ease of storage and transportation make coal, oil and natural gas ideal sources of fuel, however fossil fuels cannot continue to meet our energy demands indefinitely. By 2040 the global population will likely have grown to around 9 billion and with it the demand for energy will have increased by 56% as compared to the 2010 level.[3] Even at the current consumption rate, estimated reserves range from 150 to 400 years for coal, 40 to 80 years for oil and 60 to 160 years for natural gas.[4] Dwindling reserves coupled with uncertain energy security for those countries lacking fossil fuel resources highlight the need to develop viable alternative energy sources.

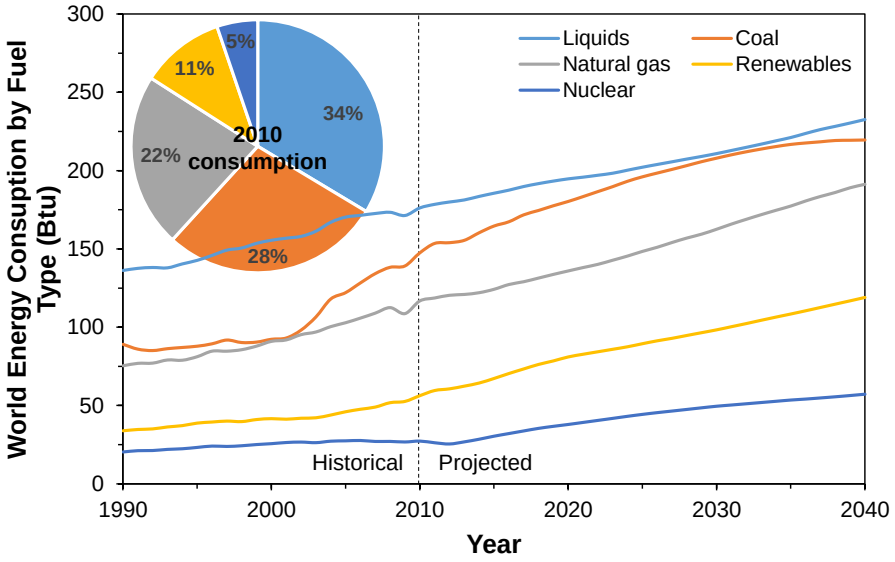

Figure 1.1 World energy consumption by fuel shown in Btu, (British thermal units). Liquids refers to petroleum and other liquid fuels and renewables includes hydropower, biomass, solar, geothermal, waste and tidal). Data adapted from[3]

Of greater concern is the environmental impact caused by the release of greenhouse gases from burning carbon-based fossil fuels, in particular carbon dioxide. The concentration of atmospheric CO_2 has been shown to correlate with the global mean temperature over hundreds of thousands of years, Figure 1.2, and is currently increasing at an unprecedented rate. Since the beginning of the industrial revolution, atmospheric CO_2 levels have steadily increased from 280 ppm, reaching the 400 ppm mark globally for over a month for the first time since records began in March 2015.[5] With CO_2 levels rising at a rate of around 2 ppm per year, it will not be long before they reach 450 ppm, carrying a high risk of global warming by more than 2°C relative to pre-industrial levels. Such a rise is likely to produce a devastating impact on ecosystems and human society,[6] and in order to be avoided, a third of oil reserves, half of gas reserves and over 80% of coal reserves should not be used before 2050.[7]

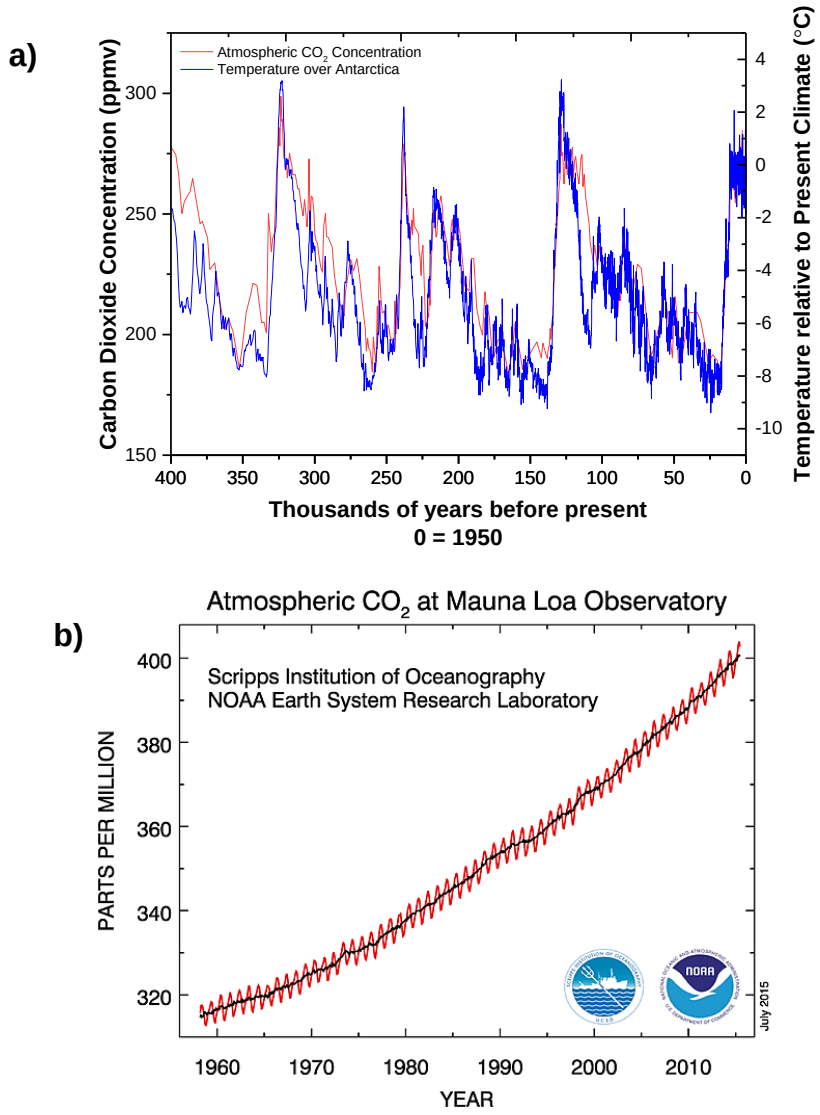

Figure 1.2 Historic and recent trends in the atmospheric CO_2 concentration. a) Temperature and CO_2 records from Vostok ice core (Data adapted from[8]) and b) atmospheric CO_2 concentrations recorded at the Mauna Loa Observatory, 1960-present. Reproduced with permission from[9]

Although it is thought we will still rely on fossil fuels for more than 75% of our power in 2040,[3] renewable energy is gaining traction. In 2013 the capacity of new renewable electricity installations exceeded those of fossil fuel installations for the first time ever, with 143 GW of renewable electricity capacity installed compared with 141 GW of plants that burn fossil fuels.[10] There is also increasing public pressure on politicians and businesses to implement renewable energy solutions and withdraw investment from companies profiting in oil, gas and coal. As of July 2015, 253 organisations with a combined value of over $61bn, (including universities, religious institutions, charitable foundations and governmental organisations) have divested from fossil fuel companies.[11]

1.2 Renewable Energy Sources

The renewable energy sector is experiencing a coming-of-age. Globally, renewable energy sources account for 13.2 % of our primary energy supply and around 22% of our electricity supply, but this is projected to increase by a factor of 3 by the year 2040.[12] If we are to commit to avoiding an increase in the atmospheric CO_2 concentration to 450 ppm, (which is predicted to have a devastating impact on ecosystems and human society) then this growth will be by a factor of 3.5. To achieve this, low-carbon technologies must be deployed rapidly on a global scale. Table 1.1 displays the estimated power generation capacities of several renewable energy sources.

Fortunately renewable energy technologies have the potential to be used on a large scale as resources are spread globally, in contrast to conventional sources such as gas, coal and oil, which are more geographically concentrated. All countries in the world have at least one abundant renewable resource and many countries have a range of different resources. Any future energy infrastructure will likely rely on a mixture of technologies, depending on which resource is locally abundant. In one forecast, by 2040 the Middle East will rely on solar technologies for more than 50% of their power generation, but in regions with lower insolation such as the European Union, alternative resources such as wind power will make up a greater part of the energy mix as displayed in Figure 1.3.

Energy source	Power (TW)	Remarks
Wind	4	Represents 10-15 % of global potential for on- and off-shore installations
Hydroelectric	1-2	Remaining untapped potential is 0.5 TW
Tidal	<2	-
Geothermal	12	Only a small fraction of this can be exploited
Biomass	10	Requires 10 % of the earth's surface to be covered in switchgrass
Solar	>20	Requires 0.16 % of the earth's surface to be covered with 10 % efficient solar cells

Table 1.1 Global power generating capacities of several renewable energy sources[4, 13]

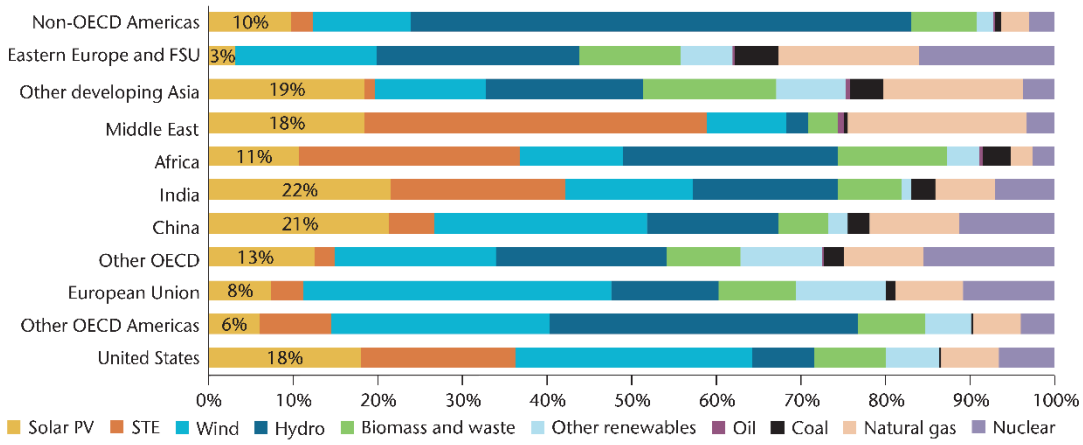

Figure 1.3 Predicted 2050 power generation by region (STE = solar thermal energy). Reproduced with permission from[14]

Of the available renewable sources, solar energy has the greatest potential to meet our future energy demands, with around 120,000 TW insolation reaching the earth's surface each year.[13] There are several established technologies to convert sunlight into more useable forms of energy, the most prevalent of which are solar photovoltaic cells. Photovoltaic cells are comprised of semiconducting materials exhibiting the photovoltaic effect, which when connected to an external circuit convert light directly into electricity by the creation of electron and hole pairs. Currently the solar cell industry is one of the world's fastest growing markets, expanding of a rate of about 40 % a year. In 2014 a record 40 GW of capacity was added, to bring the global total installed capacity to 177 GW.[15] Intensive research and industrial innovations have led to a rapid decrease in the average cost of PV arrays which if continued, will lead to cost-competiveness with fossil fuels in the next 1-2 decades in the United States.[16]

1.3 Solar Fuels

The falling price of photovoltaic technology and imperative to reduce greenhouse gas emissions will see solar energy become an important component of the global energy mix in the coming years. It is estimated that by 2050, solar energy could be the single largest source of electricity ahead of fossil fuels, wind, hydro and nuclear.[14, 17] As the contribution of solar energy to the total energy mix increases, it will become challenging for the electricity network to manage the intermittent nature of solar power, both daily as well as seasonally. Figure 1.4 shows the calculated solar radiation in London over the

course of a day at different times of year. The maximum available power in summer is greater by a factor of ~2 than in winter and there are twice the hours of sunlight.

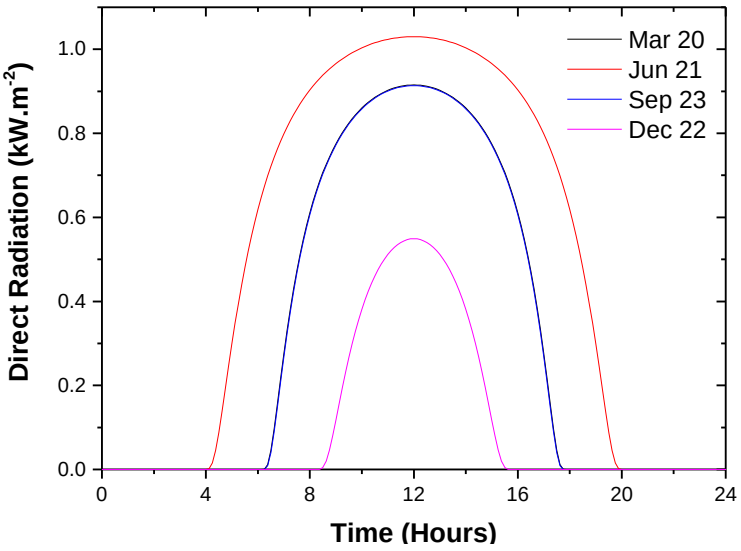

Figure 1.4 Calculated maximum amount of direct solar radiation at 51° N (London) over a period of a day at different times of year (March 20 = spring equinox, June 21 = summer solstice, September 23 = autumnal equinox, December 20 = winter equinox). Data adapted from[18]

If solar energy is to provide a significant portion of our total power, large-scale storage solutions must be implemented. Currently pumped-hydroelectrical systems account for more than 99% of storage capacity worldwide, (total 127 GW capacity), but have limited geographical distribution.[19] Alternative storage technologies include solar-thermal storage, batteries and compressed air, but none of these technologies are appropriate on a terawatt scale. It is far more practical to take inspiration from nature and directly convert solar energy into a chemical fuel which can be stored and then used as required. Termed 'artificial photosynthesis', the process of converting sunlight into a fuel using man-made materials has been the source of intense scientific research in recent years.

In plant photosynthesis, carbon dioxide and water are converted to carbohydrates and oxygen using sunlight to drive the process. Light is harvested at two photosystems, PS I and PS II, which are connected in series by an electron transfer chain creating a 'Z-scheme', Figure 1.5. At PS II the first photon absorption occurs and the resultant hole drives water oxidation at an oxygen evolving site, which consists of a magnesium-calcium oxide cluster.[20] The photoexcited electron is shuttled through a series of steps to PS I, where a second absorption occurs and the electron is used to fix a proton to

nicotinamide adenine dinucleotide phosphate, $NADP^+$, to form NADPH. The strongly reducing NADPH in turn reduces CO_2 to the resulting carbohydrate. Over the life time of a plant the process of natural photosynthesis operates with an efficiency of around 1%.[21]

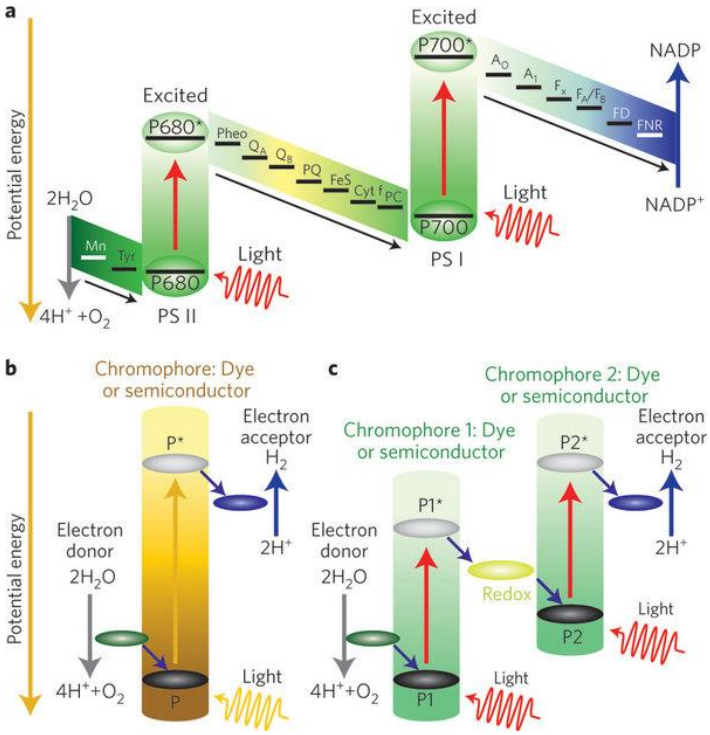

Figure 1.5 Comparison between natural and artificial photosynthesis. The so-called Z-scheme of natural photosynthesis is shown in a) and is driven by the absorption of two photons, one at PS II and the other at PS I. A single step artificial photosynthesis scheme is shown in b) and a two-step process with redox mediator in c), both for the application of water splitting. Reproduced with permission from[22]

Photosynthesis has been exploited by countries such as Brazil, where sugar cane is used as a feed-stock for producing ethanol (biofuel). However, the relatively low solar to biomass energy conversion efficiencies has constrained biofuel production to economies with enormous amounts of arable land.[23] As an alternative, bio-inspired approaches – deemed artificial photosynthesis – have shown great promise, where materials that use sunlight to drive the synthesis of molecular fuels have been developed.[22] Artificial photosynthesis aims to mimic the main stages of photosynthesis: light harvesting, charge generation and separation, and catalysis. Semiconductor materials are often selected as simple artificial photocatalysts as they can capture solar photons via excitation of an electron from the valence to the conduction band. Charge separation is inbuilt between their valence and conduction bands and generates the power required for driving chemical reactions at their surfaces, or at the surface of a co-catalyst, Figure

1.5b. Inorganic materials are usually photochemically stable making them good candidates to develop robust technology for large-scale solar fuel production. The photosynthetic Z-scheme can be mimicked by pairing two semiconductors coupled either with or without a redox mediator. Similar to natural photosynthesis, the oxidation and reduction reactions occur at different sites, Figure 1.5c.

Significant progress has been made in the artificial photosynthesis field producing two important types of fuel: carbon based fuels and hydrogen. At a first glance producing high energy density carbon-based fuels such as methanol or methane by direct photoreduction of CO_2 would be ideal. Carbon dioxide could be captured at fossil fuel based plants thereby closing the CO_2 loop, however this is associated with a significant energy penalty. Moreover, the photoreduction of CO_2 to methanol or methane is extremely challenging, proceeding via six- and eight-electron transfer steps respectively, thus current device efficiencies are generally very low. Photoreduction of CO_2 to useable fuels generally proceeds with efficiencies less than 1%.[24]

Photo-driven water splitting to produce hydrogen on the other hand, has reported device efficiencies up to 18 %,[25] and offers a pathway to not only a versatile fuel, but also an important industrial commodity. Industrially H_2 is used to produce fertilisers in the Haber-Bosch process, which consumes 3-5 % of the world's natural gas supply and 1-2 % of the world's total energy supply,[26] therefore the production of renewable hydrogen would have a large global impact. Currently 96 % of hydrogen is produced from fossil fuels,[27] making photo-driven water splitting is an attractive route to renewable H_2.

For use as an energy vector, hydrogen can be converted into electricity using fuel cell technology thus a renewable energy infrastructure based on sunlight, water and electricity can be imagined. unfortunately electricity generation does not address transport-related fossil fuel consumption, which accounts for around 40 % of the total fossil fuel consumption in the UK.[28] Compared to gasoline, hydrogen has a higher gravimetric density (120 vs 44 MJ/ kg) but a substantially lower volumetric density (8 vs 32 MJ/ L) resulting in a low energy per unit volume. One solution is to convert hydrogen into liquid hydrocarbon fuels using established chemistry (e.g., reverse water gas shift and Fischer-Tropsch processes), but this is still associated with the release of CO_2 into the atmosphere. If hydrogen itself is to be used as a fuel, the development and utilisation of advanced storage methods will be required.

Hydrogen can be stored either physically, such as in high pressure or cryogenic storage containers, or chemically through the formation of chemical bonds such as in metal hydrides.[29] Physical storage has thus far been the main hydrogen storage technology used in prototype hydrogen-powered vehicles. The US Department of Energy's Fuel Cell Technologies programme has already routinely demonstrated hydrogen fuel cell vehicles capable of driving 250 miles on a single 4 kg tank of hydrogen, which are twice as efficient as today's gasoline vehicles.[30]

1.4 Photo-driven Water Splitting

Though conceptually simple, splitting water into its component parts is no small task. The reaction is associated with a large Gibbs free energy change, $\Delta G^0 = +237$ kJ/ mol, which according to the Nernst equation corresponds to $\Delta E^0 = 1.23$ V. The reduction half-reaction to produce hydrogen proceeds via a 2-electron transfer reaction while 4-electrons are involved in the oxidation of water to form oxygen. The overall water splitting reaction is as follows:

$$2H_2O \rightarrow 2H_2 + O_2 \tag{1.1}$$

In acidic electrolyte the oxidation and reduction reactions can be written as:

$$2H_2O + 4h^+ \rightleftharpoons O_2 + 4H^+ \qquad E^0_{ox} = -1.229 \text{ V vs NHE} \tag{1.2}$$

$$2H^+ + 2e^- \rightleftharpoons H_2 \qquad E^0_{red} = +0.000 \text{ V vs NHE} \tag{1.3}$$

For an alkaline electrolyte the oxidation and reduction reactions can be written as:

$$4OH^- + 4h^+ \rightleftharpoons 2H_2O + O_2 \qquad E^0_{ox} = -0.401 \text{ V vs NHE} \tag{1.4}$$

$$4H_2O + 4e^- \rightleftharpoons 2H_2 + 4OH^- \qquad E^0_{red} = -0.828 \text{ V vs NHE} \tag{1.5}$$

Water splitting was first carried out in the 18th century using electrolysis,[31] whereby an electrical current is passed through two electrodes submerged in a conductive water source. In an artificial photosynthetic scheme, electrolysis can be achieved using

electricity generated in PV panels, or alternatively by means of a photoelectrochemical cell or photocatalyst.

1.4.1 Photoelectrochemical Water Splitting

Photoelectrochemical water splitting was first demonstrated by Honda and Fujishima, whose basic cell consisted of an n-type rutile photoanode and platinum cathode. In a photoelectrochemical cell, (PEC), electrons and holes generated in a semiconductor upon illumination drive the electrolysis reactions at the interface of the semiconductor and electrolyte, (or at the surface of a co-catalyst), Figure 1.6.[32]

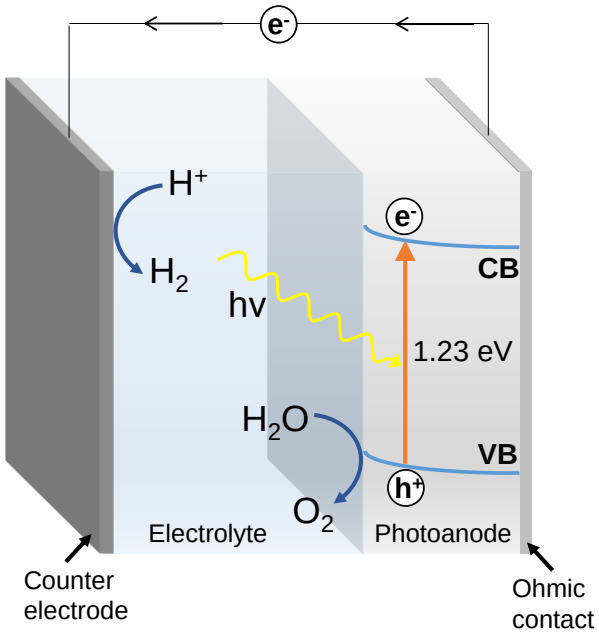

Figure 1.6 Simplified diagram of a water splitting n-type photoelectrode

In order to split water without the assistance of an external bias, a semiconductor must have band positions that straddle the water redox potentials of H^+/ H_2 (0 V vs NHE) and O_2/ H_2O (1.23 V vs NHE), thus there is a minimum band gap requirement of 1.23 eV. Although there are some materials that theoretically meet these criteria, Figure 1.7, examples of single materials that split water unassissted are rare. A commonly cited semiconductor which is known to split water without the assistance of an external bias is $SrTiO_3$, however the large band gap of this material (3.4 eV) limits the efficiency with which solar water splitting can be carried out to less than 1%.[33]

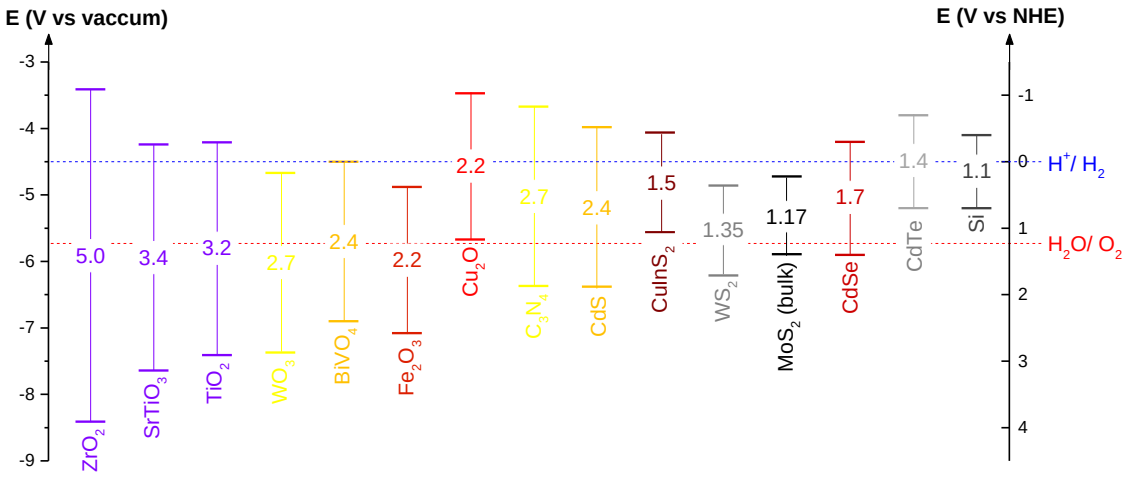

Figure 1.7 Absolute band positions at pH 0 for several semiconductors commonly used for water splitting. Data from[34]

The band gap energy of a semiconductor is a key determinant in the maximum obtainable solar-to-hydrogen (STH) efficiency. Figure 1.8 displays the maximum theoretical STH efficiency against the semiconductor band gap, assuming all photons are captured and result in the generation of current. Whilst this is a very useful guide to the potential efficiency obtainable from a particular semiconductor, the band gap alone is insufficient to describe water splitting capability. Various entropic losses mean that this value is unlikely to be reached, even in an optimised system.

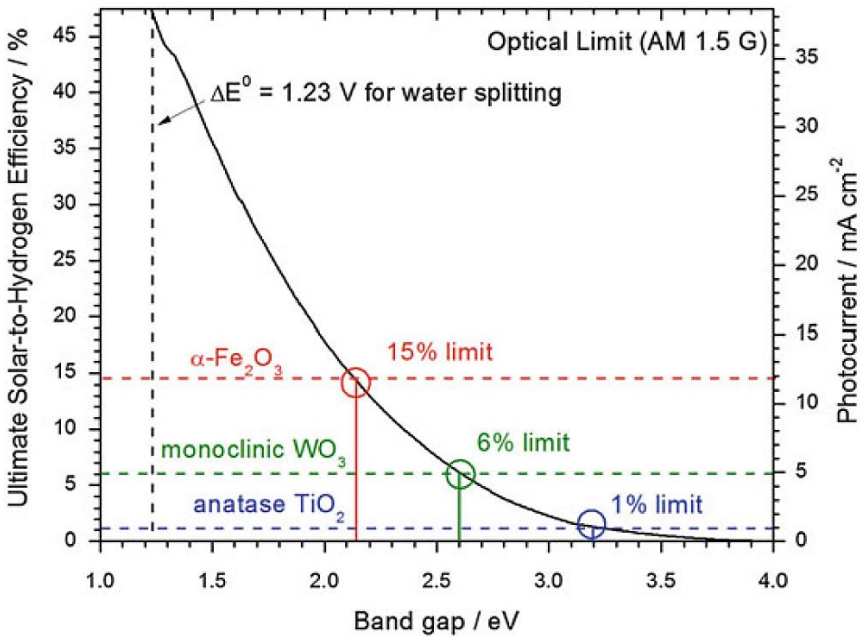

Figure 1.8 Theoretical maximum solar-to-hydrogen conversion efficiency and photocurrent as a function of the material band gap. Reproduced with permission from[35]

1.4.2 Device Designs for Photo-driven Water Splitting

Solar-driven water-splitting devices require at minimum a light absorber, fuel-forming electrocatalysts, an electrolyte, and a means to separate the products. The majority of proposed device designs fall into one of three categories: combined 'PV+electrolyser' systems, integrated photoelectrochemical arrays and photocatalyst suspensions, which differ in complexity and projected cost, Figure 1.9.

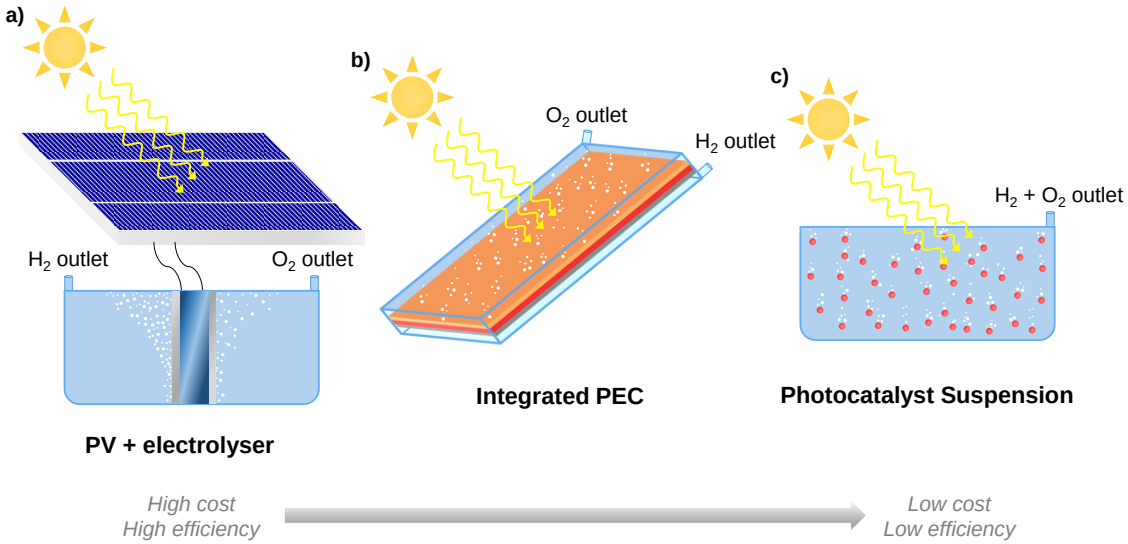

Figure 1.9 Schematic of three device architectures for solar-driven water splitting

Of the three types of proposed device, the PV+electrolyser approach is most technologically mature and the closest to market. A commercially available solar cell is coupled with a commercial electrolyser either directly or through the grid, Figure 1.9a. If the two components are connected directly, the need for an inverter is removed. This lowers the overall cost of the device, which is currently a limiting factor in adopting this technology. Estimated costs for hydrogen produced with PV+electrolysis exceed $8/ kg, well above the $2–4/ kg target set by the US Department of Energy for future hydrogen production pathways.[4] However this cost will continue to fall along with the cost of PV modules.

Regardless of the current price limitations in utilising PV+electrolysis as a pathway to renewable hydrogen, it currently has the highest reported STH, with optimised devices achieving between 12-18 % STH.[25, 36, 37] Devices also have excellent durability due to the physically separate PV and electrolyzer modules. As a result,

strongly alkaline or acidic electrolytes can be used without compromising the stability of the device.

In integrated photoelectrochemical systems, the photoabsorber is placed directly in the electrolyte, Figure 1.9b, with oxidation and reduction reactions taking place at the semiconductor electrolyte interface. Simple and elegant in concept, a PEC system combines the harnessing of solar energy and the electrolysis of water into a single device and has the potential to produce much cheaper H_2/ kg than PV+electrolyser systems. If constructed as a monolithic device, fewer packaging components are required, (frame, glass, connections, etc.) as compared to a PV-electrolysis system. For an optimised photoelectrochemical cell integrated into a tracking concentrator array, the cost for hydrogen production is estimated to be \$4.10/ kg.[38]

Despite the promise of photoelectrochemical water splitting, practical devices remain elusive due to the strict constraints on the semiconductor material. For a semiconductor to split water unassisted in a PEC device, it must efficiently absorb sunlight, separate the generated charge, create sufficient photovoltage to split water, have band positions that straddle the water redox potentials and remain stable in solution under irradiation. It is difficult for a single semiconductor to meet these requirements and so multijunction devices have been investigated with particular success. PEC multijunction devices based on III-V semiconductors have shown efficiencies as high as 12.4 % STH, approaching the efficiencies achieved by PV+electrolyser devices.[39] Unfortunately, these III-V devices lack long term stability, degrading over the course of a day.

This problem is common to many photoelectrochemical cells as very few semiconductors are sufficiently stable under operating conditions. The lack of stability is inherent to the semiconductor/ electrolyte interface where the local pH can be very high or low and there can be many free-radicals present. Some semiconductors undergo photoanodic or photocathodic corrosion in preference to water. Cadmium sulphide, for example is oxidised by photogenerated holes at the semiconductor electrolyte interface:[40]

$$CdS + 2h^+ \rightarrow Cd^{2+} + S \qquad (1.6)$$

One option is to only utilise inherently stable semiconductors in a PEC device. Generally oxide materials are resistant to photocorrosion, and in particular the d^0 and d^{10}

oxides have been shown to have excellent stability.[41] Oxide semiconductors however have their own set of limitations such as poor charge carrier transport in the case of Fe_2O_3 and large band gap in the case of TiO_2. For unstable materials, chemical species which offer a more favourable redox pathway can be added to solution to supress photocorrosion.[42] In the case of CdS, a S^{2-}/SO_3^{2-} redox couple is commonly used.

Alternatively, window materials can be deposited on the photoabsorber to protect the surface prone to degradation. The electric field generated within the semiconductor is coupled with water-splitting catalysts through ohmic contacts, typically transparent conducting oxides (TCOs). Simple photoelectrode materials such as Cu_2O, GaAs, Si and GaP which otherwise undergo rapid photodegradation have been protected with ALD-TiO_2 layers in some cases extending device lifetime to over 100 hours.[43, 44]

One advantage of coupling photoactive materials with electrocatalytic surfaces through TCO contacts is that provided sufficient photovoltage is created to split water, the band edges of the semiconductor need not align with the redox potentials of the water splitting half reactions. Redistribution of charge in the Helmholtz layer automatically adjusts electrode potentials of the catalytic surfaces in contact with the electrolyte, as in the case of metal electrodes during the dark electrolysis of water. Multijunction PVs in particular make good candidates for such 'buried junction' type devices due to the large voltages produced by cells connected in series. Some examples include Nocera's 2.5 % efficient 'artificial leaf' where a self-healing cobalt-based catalyst was deposited onto a monolithic triple junction a-Si cell with a TCO protecting layer. The catalyst can also be distinct from the surface of the photoabsorber such as in Jacobsson's 10 % efficient CIGS based device,[45] where the catalyst was deposited perpendicularly from the photoabsorber material onto metal electrodes, reducing absorption losses from shielding by the catalyst, which can be substantial.[46]

It has been argued that in addressing the issue of stability and protecting the semiconductor surface using a buried junction, a PV + electrolysis device is essentially created. It has been shown how traditional PEC devices can be transformed through a series of steps to PV + electrolysis devices and that the two technologies should be considered under the umbrella of 'Photo Driven Catalytic Devices', Figure 1.10.[47] Either way, it is clear that the two concepts are complementary and that the most successful devices will likely be a cross-breeding of the two.

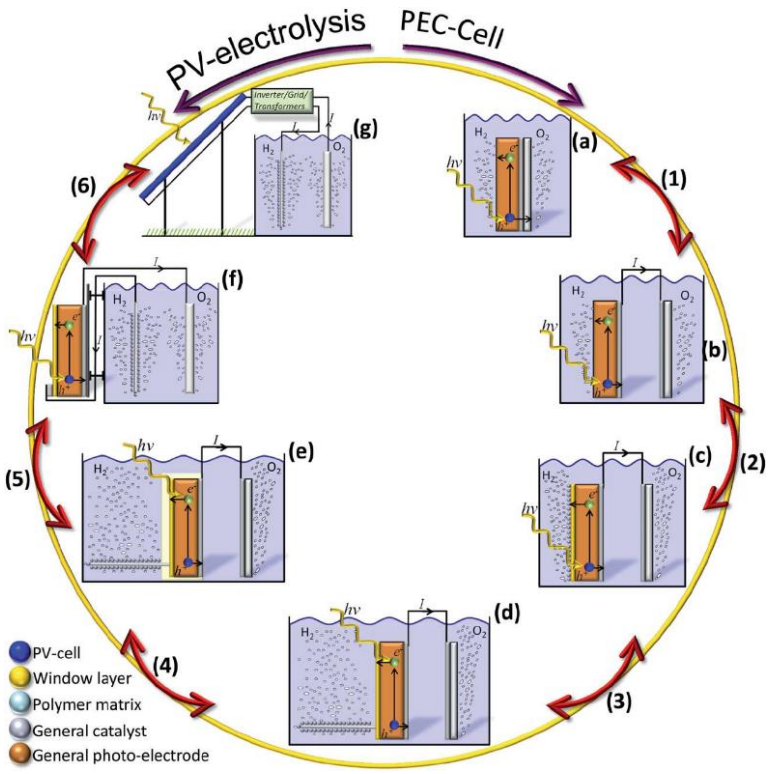

Figure 1.10 Illustration of a gradual transition in six steps from a monolithic PEC-device, (a), to a free standing electrolyzer connected to a PV-cell through the grid, (g). Reproduced with permission from[47]

The final and conceptually most simple of the three device types is the particle suspension reactor, Figure 1.9c. In this scheme semiconductor particles are dispersed in solution and are not incorporated as part of an electrode. The small dimension of the particles enables diffusion to be a sufficient mechanism for both charge separation and transport. To increase the catalytic activity, one or two co-catalysts can be loaded onto the surface of the particle, Figure 1.11a.

Proven efficiencies are somewhat low for photocatalyst suspensions with the highest reported STH being 5%,[48] but the vast majority being below 0.1%.[49] Often, the STH is so low that it is not quoted, and instead the external quantum yield (EQE) at a particular wavelength is given. It should be noted that the EQE does not account for the voltage of a reaction or product and thus cannot be considered a true power conversion. Despite the generally low efficiencies for photocatalyst suspensions, in reactor fabrication there is no need for electrodes or wiring and so this is potentially the cheapest method of producing hydrogen. Reactors can be fabricated from low cost materials such as high density polyethylene, (HDPE, which has 90% optical transmission and low hydrogen permeability),[50] and the semiconductors produced in

low cost and scalable techniques such as sol-gel or continuous hydrothermal flow synthesis.[51]

Despite the potentially low cost of photocatalyst suspension reactors, the technology is unproven and there remain important considerations that are not well understood and require further investigation. To maximise solar flux utilisation, a better understanding of the effective photon capture area per particle and optimum particle density is required. Furthermore the problem of shading, where particles that lie deeper in the reactor bed receive less light should be accounted for. Since the open circuit photovoltage decreases by a factor of (a x 2.303RT/F) per order-of-magnitude decrease in absorbed photon flux,[49] deep particles may not generate sufficient voltage to split water and instead will act as sites for the recombination of H_2 and O_2.

There are two classes of particle suspension reactor: (i) single bed photocatalyst suspension, which evolves H_2 and O_2 in the same vessel, (unless a sacrificial agent is used so H_2 is evolved in the absence of O_2), and (ii) dual bed photocatalyst suspension with a redox mediator, which evolves H_2 and O_2 in separate vessels connected by a porous bridge, Figure 1.11.

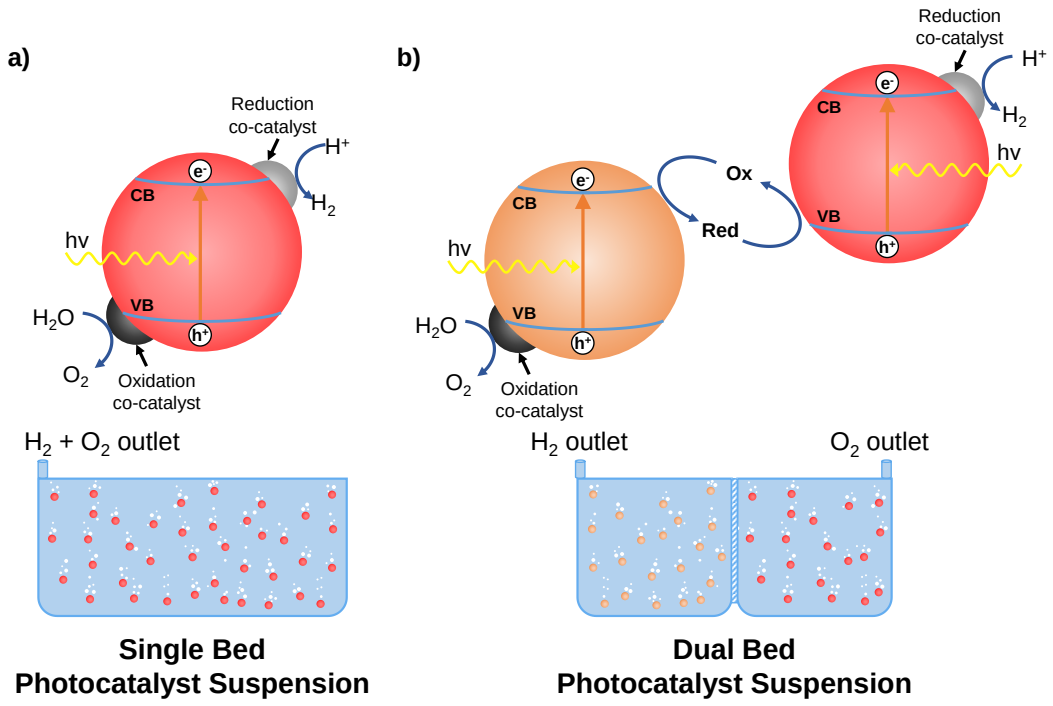

Figure 1.11 Two types of photocatalyst suspension reactor bed with schemes showing photocatalytic reactions occurring at the photocatalyst/ co-catalyst and electrolyte interface: a) single bed n-type photocatalyst suspension, b) dual bed n-type photocatalyst suspension with redox mediator and porous bridge linking the two compartments

It has been predicted that for a single bed photocatalyst suspension with 10 % STH efficiency, hydrogen can be produced for a cost competitive \$1.60/ kg; steam methane reforming, (the current cheapest method of producing hydrogen), produces hydrogen at a cost between \$1-5/ kg.[52] Despite the potential low cost of this type of photocatalyst suspension bed, it is unlikely to be commercially viable as oxygen and hydrogen are evolved in the same compartment, which can result in parasitic reactions (such as O_2 reduction) and more importantly provides a potential explosion risk in the direct reaction of H_2 + O_2 (the explosion limits of hydrogen in air are between 18 and 59%).[4] Even if the explosive gas mixture could be handled safely, a large energy expense would be needed to separate the two gases: gas separation is projected to constitute the largest fraction of single bed reactor capital costs.[38]

To prevent the co-production of hydrogen and oxygen in a single bed reactor, sacrificial reagents can be used so that hydrogen is produced in the absence of oxygen. There have been many investigations into the uses of different sacrificial reagents,[53-56] but generally for hydrogen production, electron donors such as ethylenediaminetetraacetic acid (EDTA), methanol (MeOH) and ethanol (EtOH) are used, Figure 1.12. Sacrificial reagents are most frequently chosen to provide an oxidation pathway of lower, or even negative ΔG than for true water splitting, so the process is more thermodynamically favourable.[57]

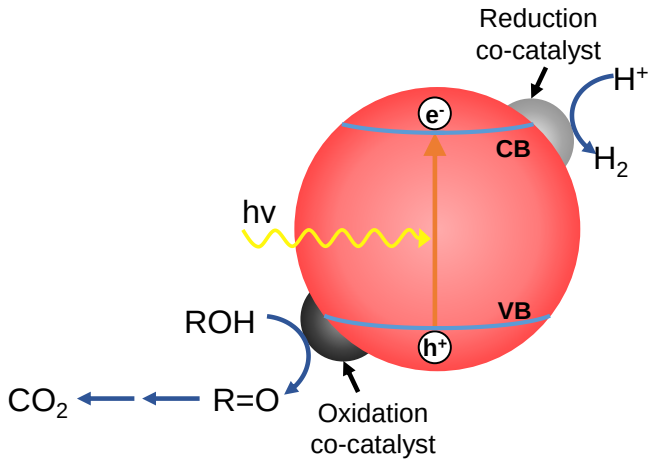

Figure 1.12 Photocatalytic water reduction on an n-type semiconductor utilising a sacrificial reagent for the oxidation half reaction. In this case an alcohol electron donor is used.

The production of sacrificial reagents represents an additional energy input, consequently this pathway for hydrogen production is only viable if readily available

chemical commodities are employed, such as biomass or waste compounds from nature or industry.[58-61] A practical demonstration of a photo-driven sacrificial system for the production of hydrogen is the Bill and Melinda Gates Foundation prize-winning sustainable toilet, developed by Michael Hoffmann et al.[62, 63] In this system, electricity generated in a PV panel is used to drive the oxidation of waste material at a TiO_2-based anode and the reduction of water at a stainless steel cathode.

In dual bed photocatalyst suspension reactors the photosynthetic Z-scheme is mimicked, Figure 1.5, albeit on a much larger scale. Oxygen and hydrogen are evolved at two different photocatalyst particles which are electronically linked using a redox mediator. The particles are suspended in separate vessels connected by an ionic bridge to allow for mediator coupling. The discrete production of oxygen and hydrogen eliminates the requirement for gas separation equipment, but reduced hydrogen production efficiency is inherent to this type of suspension bed due to ion conductivity losses and the larger solar collection area required. For this type of rector, the levelized hydrogen production cost for a 5% efficient STH system is \$3.20/ kg.[38]

1.5 Principles of Photoelectrochemical Cells: Semiconductor Theory and Characterisation

Since this thesis is concerned with the synthesis and characterisation of semiconductor materials, this section will briefly outline basic semiconductor theory, as well as some common methods utilised in determining the structure and properties of semiconductors.

1.5.1 Semiconductor fundamentals

In a solid state material atomic orbitals combine forming broad energy bands as opposed to molecular systems, which are comprised of discrete molecular orbitals. There may be several permitted energy level bands, but of particular import are the two uppermost bands which are separated by a forbidden energy gap, or band gap (E_g). These bands are known as the valance band (VB), which is filled at 0 K and the conduction band (CB), which is empty at 0 K. Filling of the bands in a solid is governed by the Pauli Exclusion Principle, thus the band may contain 2N electrons where N is the number of energy levels in a band. The Fermi level, E_F, is defined at 0 K as the

energy at which the probability of finding an electron is 0.5 and usually lies at the centre between the valence and conduction bands. The Fermi level can be regarded as the highest filled energy level in the material, as all electronic energy levels below E_F are occupied and those above E_F are likely to be empty.

Together, the E_F and E_g distinguish different classes of materials. The Fermi level position is located in the valence band for metals and the VB and CB are very close or overlap, thus metals have excellent electron conduction. Semiconductors and insulators are differentiated by the band gap energy which is typically in the region of ~1-3 eV for a semiconductor and >~4 eV for an insulators. In semiconductors and insulators, the Fermi level lies in the forbidden gap and thus neither are conductive at absolute zero.

The Fermi level of a pristine (intrinsic) semiconductor can be modified by the addition of impurities. In doped (extrinsic) semiconductors, chemical impurities introduce allowed energy states within the band gap that lie close to the energy band corresponding to that particular dopant type. In an n-type material, donor impurities create states near the conduction band, Figure 1.13a. Conversely in a p-type material acceptors create states near the valence band, Figure 1.13b. For high doping densities, the introduction of intragap states can also effect the optical properties of the semiconductor, creating new optical transitions and narrowing the bandgap.

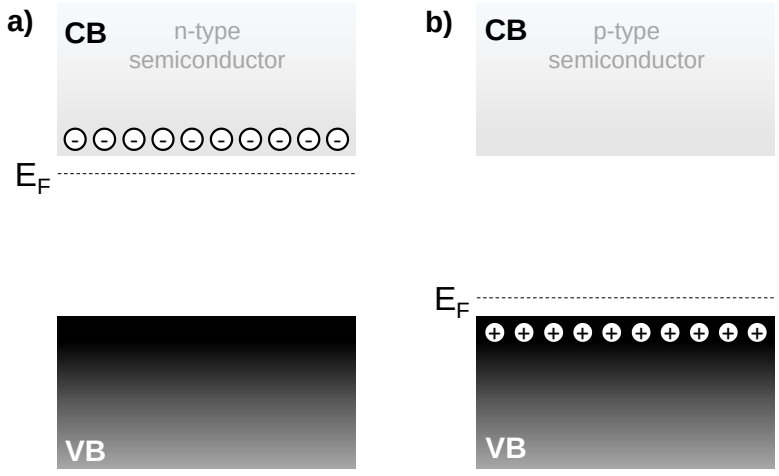

Figure 1.13 Band diagrams of extrinsic semiconductors, a) n-type and b) p-type

Semiconductors are also distinguished according to the nature of the optical transition between the valence and conduction bands. In a direct semiconductor the top of the valence band and bottom of the conduction band occur at the same value of

electron momentum. In an indirect semiconductor the maximum energy of the valence band occurs at a different value of electron momentum to the minimum energy of the conduction band. Since photons carry very little momentum, indirect transitions require absorption or emission of a phonon (i.e., a lattice vibration) and are much less likely to occur. As a consequence, the absorption coefficient of indirect semiconductors is much smaller than that of direct semiconductors – the difference can be two orders of magnitude.

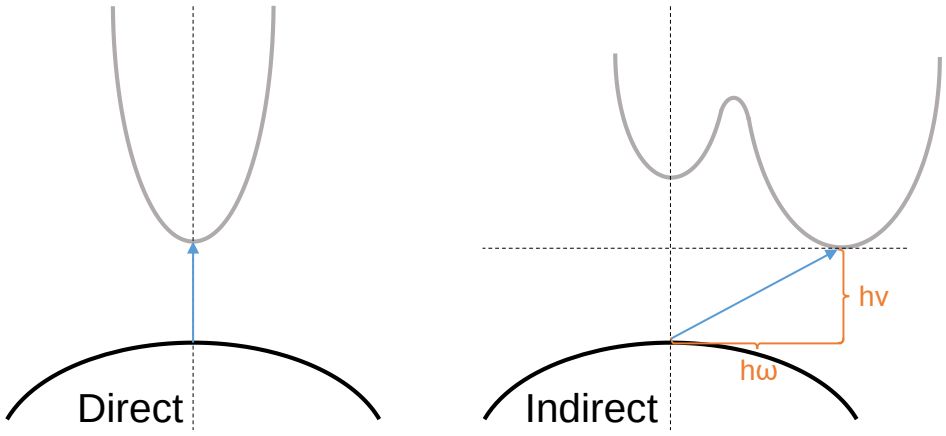

Figure 1.14 Direct and indirect optical transitions in a semiconductor. The indirect transition requires the assistance of a phonon with the energy hω

1.5.2 Experimental Techniques for the Analysis of Semiconductors

1.5.2.1 X-ray Diffraction

Probably the most important and widely used method of characterising crystalline inorganic solids is via X-ray diffraction. X-ray radiation can be used to determine the structure of a crystalline material since the characteristic wavelength of an X-ray, (~0.1-100 Å), is similar to the interatomic distances in a crystal, allowing crystal structures to diffract X-rays. An X-ray incident upon a sample can either be transmitted, or it will be scattered by the electrons of the atoms in the material. When two parallel X-rays scatter from two adjacent planes of atoms within the crystal, they can either do so constructively or destructively depending on their phase. Constructive interference occurs when two X-ray waves with phases separated by an integer number of wavelengths add to make a new wave with a larger amplitude, Figure 1.15.

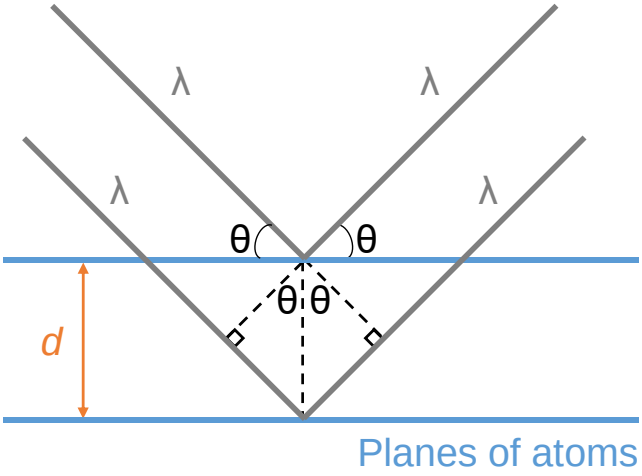

Figure 1.15 Schematic representation of diffraction of X-rays by a crystal (Bragg's Law)

The general relationship between the wavelength of the incident X-rays, angle of incidence and spacing between the crystal lattice planes of atoms is known as Bragg's Law and is expressed as:

$$n\lambda=2d\sin\theta \tag{1.7}$$

where n order of reflection, λ is the wavelength of the incident X-rays, d is the interplanar spacing of the crystal and θ is the angle of incidence. Since in a crystal atoms are arranged in a periodic fashion, the diffracted waves will consist of sharp interference maxima (peaks) with the same symmetry as in the distribution of atoms. Measuring the diffraction pattern therefore allows the determination of the distribution of atoms in a crystal.

X-ray diffraction can not only be used to identify the crystal phase of a material by comparison with data from known structures, but also to quantify changes in the cell parameters, crystal orientation, crystallite size and other structural parametersl. The average crystallite size can be estimated from the X-ray diffraction pattern by using the Scherrer equation:[64, 65]

$$B(2\theta)=\frac{K\lambda}{L\cos\theta} \tag{1.8}$$

Where B(2θ) is the line broadening at the full width half maximum (FWHM, after taking into account the instrument broadening), K is the Scherrer constant which is around 0.9, λ is the incident X-ray wavelength and L is the crystallite size.

In a polycrystalline material non-random distribution of crystallographic orientations often leads to texturing, resulting in fewer peaks in the diffraction pattern being observed than expected. The degree of preferred orientation can be estimated by comparing the observed intensities in a diffraction pattern to a bulk standard using the following equation developed by Barrett and Massalski:[66]

$$T_{c(hkl)} = \frac{I_{(hkl)} / I_{0(hkl)}}{\frac{1}{N}\left[\sum_N I_{(hkl)} / I_{0(hkl)}\right]} \quad (1.9)$$

where T_C is the texture coefficient of a given plane (hkl), I is the measured intensity, I_0 is the intensity of a bulk powder and N is the number of reflections observed in the pattern. Any deviation of the texture coefficient from unity indicates a higher degree of preferred orientation of the crystallites.

1.5.2.2 Raman Spectroscopy

Raman spectroscopy is often used as a complimentary technique to XRD in the characterisation of semiconductor materials as it is very sensitive to the local crystallinity of a material. Raman spectra can reveal a wide range of information about a material, including the crystal structure type and orientation, strain/ stress present in the lattice, dopant concentration etc. Raman spectroscopy is a non-destructive technique and conveniently spectra can be acquired in a matter of seconds, allowing for high-throughput material analysis.

Raman spectroscopy reveals information about the vibrational modes in a material from inelastically scattered, (or Raman scattered) light. Light incident on a material will either be reflected, absorbed or scattered. Most light scattering by a material will be elastic light scattering (Rayleigh) and no change in energy will be observed. Inelastically scattered light can be of higher or lower energy depending on the vibrational state of the material, Figure 1.16.

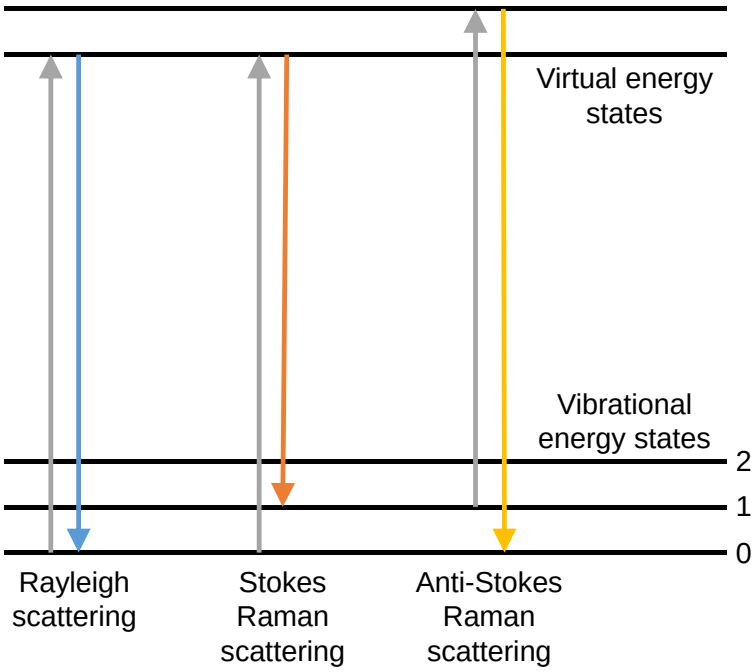

Figure 1.16 Energy level diagram for elastically (Rayleigh) and inelastically (Raman) scattered light. Inelastically scattered light can either be of a lower (Stokes) or higher (Anti-Stokes) energy than the incident light depending on the vibrational state of the molecule.

Raman bands arise from a change in the polarizability of the molecule meaning that the observed bands arise from specific characteristic molecular vibrations. When the energies of these transitions are plotted as a spectrum, they can be used to identify the material as they provide a "molecular fingerprint" of the material being observed. In crystalline solids, atomic vibrations are quantized (phonons) and they are very sensitive to internal and external perturbations, such as doping and stress. Changes in the length of the bonds and the tension in them alters the frequency of the phonons. The frequency of the scattered light is then a local probe of the perturbation experienced by the material.

1.5.2.3 X-ray Photoelectron Spectroscopy

X-Ray photoelectron spectroscopy (XPS) is a technique used to investigate the chemical environment of the elements at the surface of a material. The underlying principle of XPS relies on the photoelectric effect, whereby electromagnetic radiation incident on a material stimulates the emission of electrons. In XPS, the sample is irradiated with X-rays (typically Al Kα or Mg Kα). When an X-ray photon hits and transfers this energy to a core-level electron, it is emitted with a kinetic energy

dependent on the incident X-ray and binding energy of the atomic orbital from which it originated, Figure 1.16. The kinetic energy of the ejected electrons is measured and used to calculate the electron binding energy.

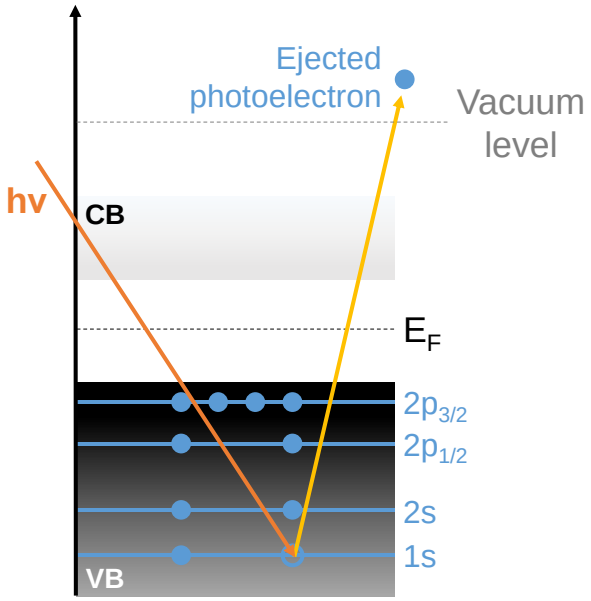

Figure 1.17 Schematic of photoelectron emission

As electrons are strongly scattered by atoms, only the surface layers can be detected. Since the core electrons in each element have a characteristic binding energy, XPS analysis can be used to identify the elements present at the surface of a material including the oxidation state of the element. XPS can also be used to investigate the electronic band structure of the filled valance band in the sample by identifying the energy of the electrons in the valence band relative to the Fermi level.

1.5.2.4 Band Gap Determination Using UV-Visible Spectroscopy

The optical band gap of a semiconductor can be experimentally determined using UV-Vis spectroscopic measurements. Spectra should be captured in transmittance mode and the absorbance can be determined using the relation:

$$A = 2 - \log_{10}\%T \tag{1.10}$$

Where A is absorbance and T transmittance. The absorbance A is then normalized to the path length l of the light through the material (e.g., the thickness of a film), producing the absorption coefficient, α:[67]

$$\alpha\ (\mathrm{cm}^{-1}) = \frac{\ln(10) \times A}{l\ (\mathrm{cm})} \tag{1.11}$$

Values of $\alpha > 10^4$ often obey the following relation presented by Tauc and supported by Davis and Mott:[68, 69]

$$\alpha h\upsilon \propto \left(h\nu - E_g\right)^{1/n} \tag{1.12}$$

Where n can take on values of 3, 2, 3/2, or 1/2, corresponding to indirect (forbidden), indirect (allowed), direct (forbidden), and direct (allowed) transitions, respectively.[70] These so-called Tauc plots of $(\alpha h\nu)^n$ versus $h\nu$ yield the value of the band gap when extrapolated to the energy axis.

1.5.3 Semiconductor Electrochemistry

When a photo-induced excitation occurs in a semiconductor, an electron is promoted from the VB to CB. This causes the generation of an electron-hole pair which primarily recombine releasing energy as heat or photons, unless there is a sufficient driving force to prevent this recombination. In photoelectrode-based systems, charge separation is largely due to the built-in electric field at the interface of the semiconductor and electrolyte. The formation of the semiconductor/electrolyte junction has most famously been modelled by Gerischer,[71] and closely follows solid state junction formation analogies.

When a semiconductor is immersed in an electrolyte, if the chemical potential of the semiconductor, E_F, and the electrochemical potential of the electrolyte, E_{redox}, (given by the Nernst expression), do not lie at the same energy and electrical current flows between the semiconductor and the solution until equilibrium between E_F and E_{redox} is reached. The electrochemical potential of the electrolyte is generally considered analogous to the Fermi level of the semiconductor. It should be noted that whilst the redox potential of an electrolyte is usually quoted against the standard hydrogen

electrode scale, (SHE), the Fermi level of a semiconductor is typically given with reference to the electron energy in vacuum. The two scales can be related using the following equation:[72]

$$E_{F,\,redox} = -4.5\ eV - e_0E_{redox} \quad (1.13)$$

For an n-type semiconductor, the Fermi level usually lies above the 'Fermi level', $E_{F,\,redox}$, of the electrolyte, thus equilibration occurs via the transfer of electrons to the electrolyte. The residual positive charge extends into the semiconductor for a significant distance (100 – 1,000 Å) referred to as the space charge region. Since the valence and conduction band energy levels are pinned at the surface of the semiconductor (due to interactions with the electrolyte), the positive charge associated with the space charge region is reflected in an upward bending of the bands in the material bulk, Figure 1.18c. In the case of a p-type semiconductor E_F usually lies below E_{redox} and electrons are transferred from solution into the semiconductor. The space charge region is then associated with a negative charge, causing a downward bending of the bands, Figure 1.18d. In both cases the semiconductor is depleted of majority charge carriers at the interface of the semiconductor and electrolyte and so the space charge region is also referred to as a depletion layer.

The charge transferred into the electrolyte forms an electrical double layer, comprised of a compact Helmholtz layer (typically 0.4-0.6 nm),[72] and a more diffuse Gouy-Chapman layer. The Helmholtz layer generally forms an inner layer comprised of adsorbed water species (H^+ and OH^-) and an outer layer of solvated electrolyte ions of the opposite charge. Just as in the semiconductor space charge region, there is a potential drop between the inner and outer Helmholtz layers, called the Helmholtz double layer voltage, V_H. Depending on the pH of the solution, either H^+ or OH^- ions will dominate the inner Helmholtz layer affecting the charge distribution at the semiconductor/ electrolyte interface and thereby also the potential distribution.= in the semiconductor.

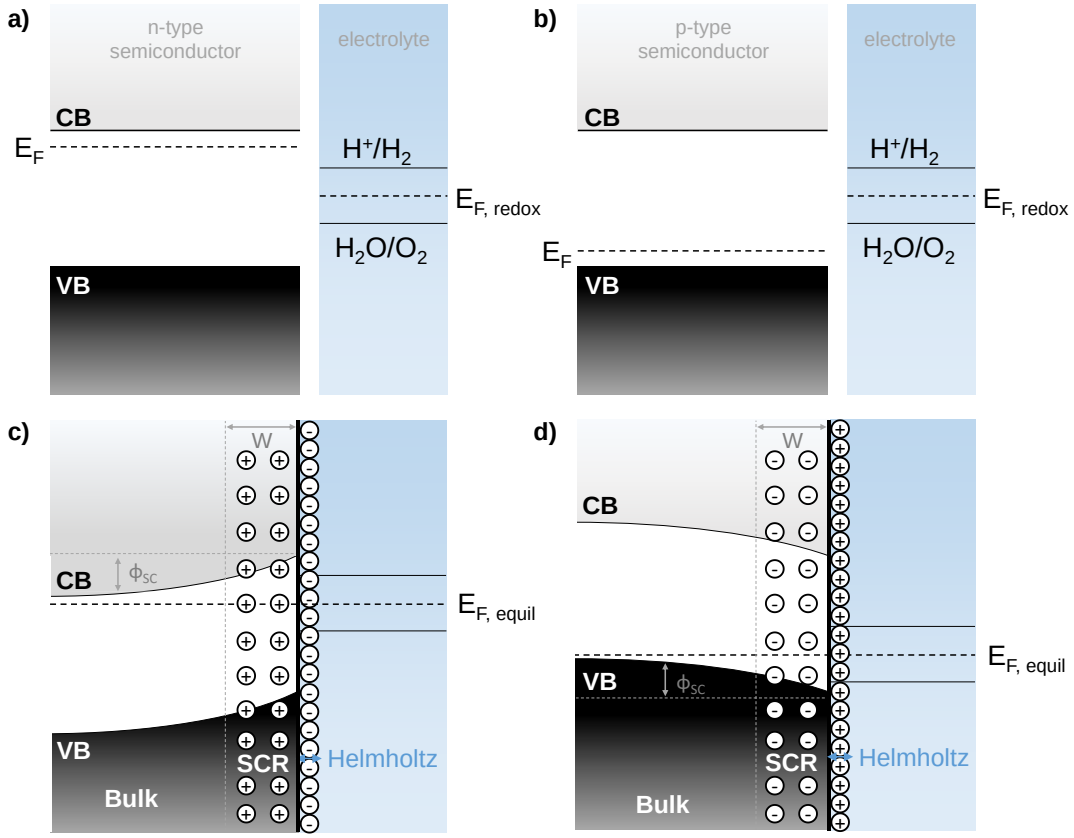

Figure 1.18 Semiconductor electrolyte junction formation for n-type and p-type semiconductors. a) and b) represent an n- and p-type semiconductor before contact with the electrolyte and c) and d) after contact respectively showing the charge distribution at the sc-el interface.

The presence of the space charge layer in the context of PEC electrodes is important, as in this region a potential drop, ϕ_{SC}, is present. This produces the electric field which is responsible for charge separation. The potential distribution and width of the space charge layer depend upon the amount of charge transferred to the surface and the density of shallow donors, N_D, or acceptors, N_A, in the material. The width of the space charge layer, W, is determined by the following, (the derivation of which can be found in[73]):

$$W = \sqrt{\frac{2\varepsilon_0\varepsilon_r}{eN_D}\left(\phi_{SC} - \frac{kT}{e}\right)} \tag{1.14}$$

Where ε_0 the dielectric permittivity in vacuum and ε_r the relative dielectric permittivity of the semiconductor. Any charge carriers generated within the space charge region are efficiently separated; in an n-type semiconductor the direction of the electric field is such that holes are swept to the surface and the electrons are driven to the rear ohmic

contact. Beyond the space charge region, the extent of collection of minority charge carriers depends upon processes of diffusion. The diffusion length, L_D, defines the region in which electron and hole pair generation is effective. Beyond a distance of L_D + W, electron and hole pairs generated will simply recombine, Figure 1.19. Thus the effective quantum yield for a semiconductor photoelectrode will depend not only on the light penetration length, $1/\alpha$, but also the relative magnitudes of W and L_D.

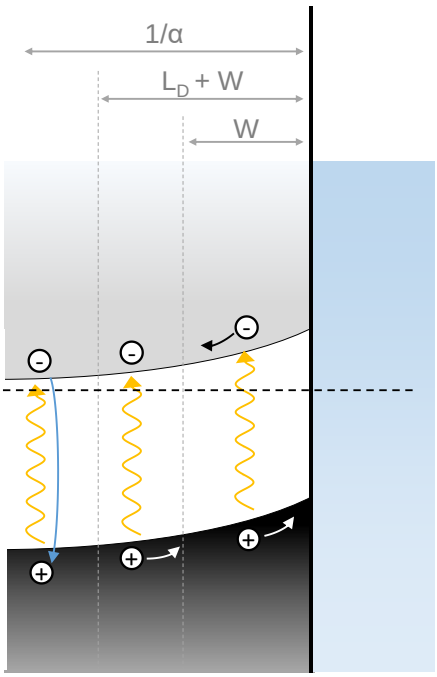

Figure 1.19 Absorption regions in an n-type semiconductor. Those charge carriers generated within a distance (L_D + W) contribute to the photocurrent but those outside of this region will recombine.

The edges of the band at the semiconductor-electrolyte interface are pinned and not affected by changes in potential, but the band levels of the interior of the semiconductor (away from the depletion region) are, so overall band bending depends on the applied potential. At a certain potential, the Fermi level and the redox solution potential lie at the same energy and no band bending occurs: this is referred to as the flat-band potential, E_{FB}. In an n-type semiconductor at potentials negative of the flat-band potential, an accumulation region develops in the semiconductor (caused by excess charge carriers, in this case electrons) and the band bends upwards. Depletion regions arise at potentials above the flat-band potential causing the band to bends downward, Figure 1.20. The opposite is the case for a p-type semiconductor, where depletion regions arise on application of a reverse bias and accumulation regions arise on forward

bias. The Fermi level in the semiconductor is shifted by ($V_{applied}$ – V_{eq}) from its equilibrium position, increasing the potential drop and extending the space charge region in the semiconductor.

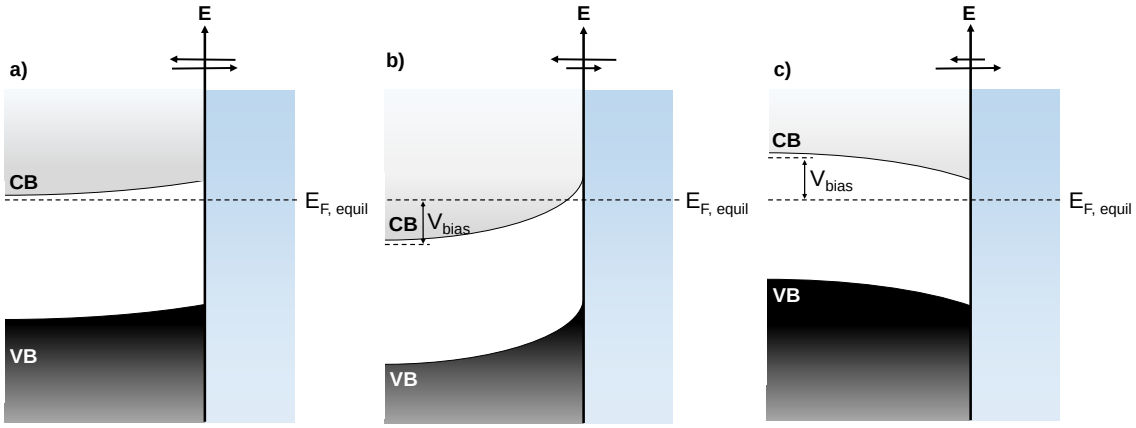

Figure 1.20 n-type semiconductor-electrolyte interface at a) equilibrium, b) potentials above the flat band potential (reverse bias) and c) potentials below the flat band potential (forward bias)

Whilst the Helmholtz potential, V_H is not affected by the applied potential, it does adjust depending upon the pH of the solution (whether H^+ or OH^- ions dominate the inner Helmholtz layer). The dependence of V_H on the pH of the electrolyte is summarised in the following:

$$V_H(volts) = 0.059 \times (pH_{PZZP} - pH) \quad (1.15)$$

where pH_{PZZP} is the pH of the point of zero zeta potential, (the point at which there is no net charge at the surface of the semiconductor). The energy levels of the semiconductor are intrinsically linked in the experimentally measurable quantity, the flat band potential, expressed in the following:

$$E_{FB} = A + \Delta E_F + V_H + E_0 \quad (1.16)$$

Where ΔE_F is the difference between the Fermi level and the majority carrier band edge and E_0 is the scale factor relating to the reference electrode redox level to the absolute vacuum scale (-4.5 V for NHE). E_{FB} is hence a property of the interface between the semiconductor and electrolyte and thus the band positions of the semiconductor will shift by 0.059 mV in the negative direction for each unit decrease in pH.[74] This is

applicable to metal oxide semiconductors, whose band edges show a Nernstian dependence in changes in pH but not necessarily to non-oxide semiconductors which may have alternative potential determining ions (other than OH^- and H^+).[75]

The shifting of the band edges according to the pH may seem like an extremely useful property: if reduction of a certain species is not possible because the conduction band is too low in energy, one might consider increasing the pH toward more alkaline values to make V_H more negative and raise E_c with respect to E_{redox}. Unfortunately, this strategy does not help for water splitting because the reduction and oxidation potentials of water also depend on the pH via the Nernst equation, thus the band positions of most metal oxides are fixed with respect to the water redox potentials, Figure 1.21.

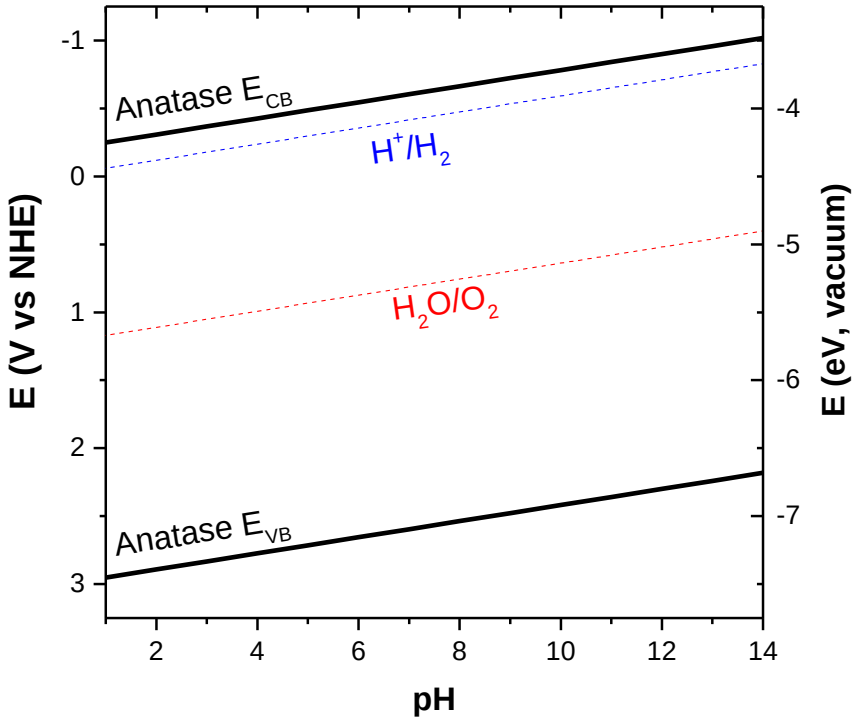

Figure 1.21 Dependence of the conduction and valence band edges of TiO_2,[76] and water redox potentials on the pH of the solution.

1.5.4 Photoelectrodes Under Operating Conditions

The fundamental processes of photoelectrochemical water splitting for an n-type photoanode in a two electrode system are illustrated in Figure 1.22. Incoming photons with an energy greater than the semiconductor band gap are absorbed, generating electron and hole pairs with an efficiency of η_{e^-/h^+}. The holes are swept to the surface of the semiconductor where they drive the water oxidation reaction. Electrons are

transported to the counter electrode via an electrical connection where they drive the water reduction reaction. The efficiency of charge separation, $\eta_{transport}$, and the combined efficiency for charge carrier transfer at the semiconductor/electrolyte interface, $\eta_{interface}$, along with η_{e^-/h^+} dictate the incident photon-to-current efficiency, which will be examined in greater detail in section 1.5.5:

$$IPCE = \eta_{e^-/h^+}\eta_{transport}\eta_{interface} \quad (1.17)$$

Under illumination the thermal equilibrium of the system is disturbed, particularly within the space charge region where charge carriers are generated. A single Fermi level can no longer be defined and instead quasi-Fermi levels which are defined by equations and should be considered:

$$E_{F,n}=E_C+ k_BT \ln(n/N_C) \quad (1.18)$$

$$E_{F,p}=E_V - k_BT \ln(p/N_V) \quad (1.19)$$

Where E_C and E_V are the energies of the conduction and valance bands respectively, n and p the concentration of the majority charge carrier and N_C and N_V the density of states in the conduction and valance bands respectively. With respect to the thermal equilibrium populations of carriers, the excess hole population significantly alters the minority-carrier distribution, while the excess electrons barely affect the majority-carrier numbers. As a result, the hole quasi-Fermi level shifts substantially in contrast to insignificant change in the electron quasi-Fermi level.

The maximum obtainable photovoltage, V_{ph}, of the semiconductor is the potential difference between the quasi-Fermi levels of electrons, $E_{F,n}$, and holes, $E_{F,p}$ and is typically 50-75 % of the semiconductor band gap. The minimum thermodynamic voltage for splitting water is 1.23 V, as such in a practical system, the semiconductor must have a band gap of at least 1.6 eV in order to split water unassisted. When the overpotentials required for kinetically driving the water redox reactions, OP_{HER} and OP_{OER} are considered, the band gap requirement is further increased to 2.0 eV.[77] Since the oxygen evolution reaction is more complex than the hydrogen evolution reaction, a larger overpotential for OER is necessary. Overpotential losses due to poor ionic

conductivity of the solution can also be significant. In particular the splitting of pure water is a challenge as the ionic conductivity is very low, thus acid, alkaline or buffered neutral solutions are usually used.

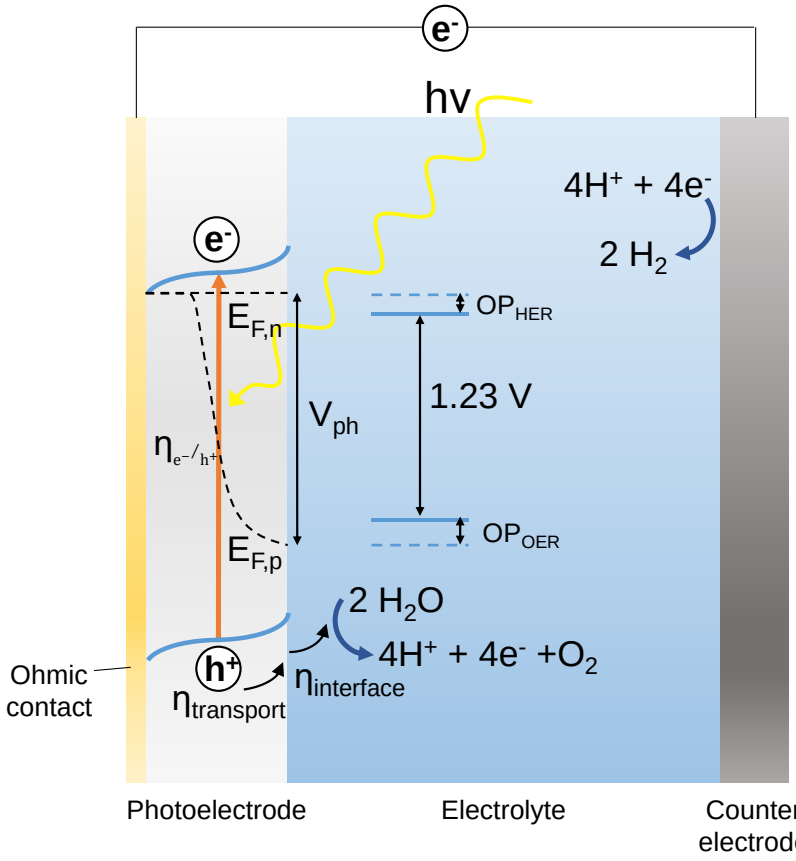

Figure 1.22 Band structure of an n-type photoelectrode showing the fundamental processes and energetic requirements of water splitting. Adapted from[35]

The extra overpotential required to split water is often supplied by the application of an electrical bias between the anode and cathode. The effect of an applied bias with and without radiation is as follows. For an n-type semiconductor, at potentials negative of the flat band potential (with and without irradiation), an accumulation region exists and cathodic current flows. The semiconductor-electrolyte interface is not perturbed by an external bias and so no net current flows without irradiation (dark curve, Figure 1.23). At potentials positive of the flat-band potential a depletion region exists (with an associated electric field) and so when the semiconductor is irradiated with light of a sufficient energy electron-hole pairs are generated which are separated by the electric field and photocurrent flows. The photocurrent is independent of the magnitude of the positive potential and so is seen to plateau (light curve, Figure 1.23) but does vary with

irradiation intensity. At the flat band potential due to the lack of a depletion region no current flows, but beyond this potential a depletion region exists and current flows thus the flat band potential is also referred to as the onset potential.

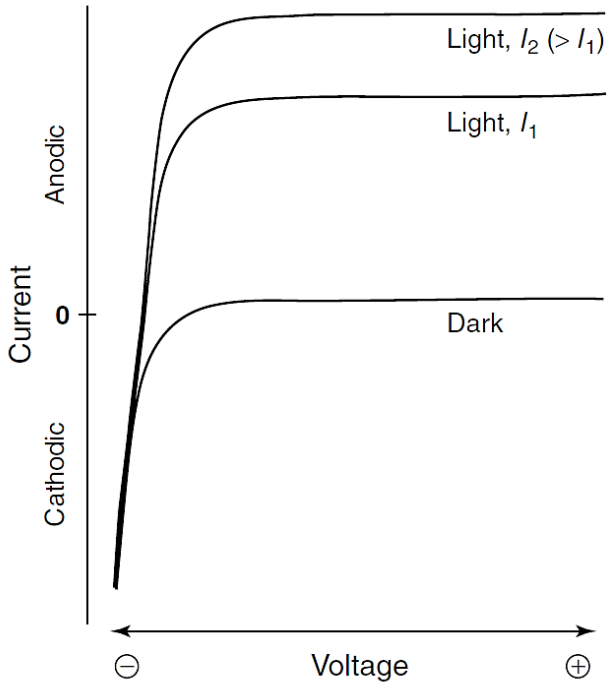

Figure 1.23 Current-potential curves for an n-type semiconductor in the dark and under illumination with two intensities of light. Reproduced with permission from[72]

1.5.5 Efficiency Definitions

This section will *briefly* describe some commonly used diagnostic techniques and metrics to characterise the operating efficiency of photocatalysts and photoelectrochemical cells. These efficiency metrics will be used to characterise the devices produced in this thesis and so will be explained here. For a more in-depth discussion, the reader is referred to a text compiled by various US Department of Energy supported institutions, 'Photoelectrochemical Water Splitting: Standards, Experimental Methods and Protocols'.[35]

As it has been seen in the previous section, the conditions under which a photoelectrode or photocatalyst is operated have a drastic effect on the obtainable photocurrent and overall efficiency. Generally, experiments should be carried out under a set of standard conditions including irradiation with an AM1.5 light source at a power output of 1 sun (100 mW.cm^{-2}), Figure 1.24. Defining a universal electrolyte is a much

more challenging task, since different semiconductors are stable in different electrolytes. Nevertheless the concentration should be greater than 0.1 M to ensure minimum solution resistance. The electrolyte used should always be quoted, along with the pH of the solution.

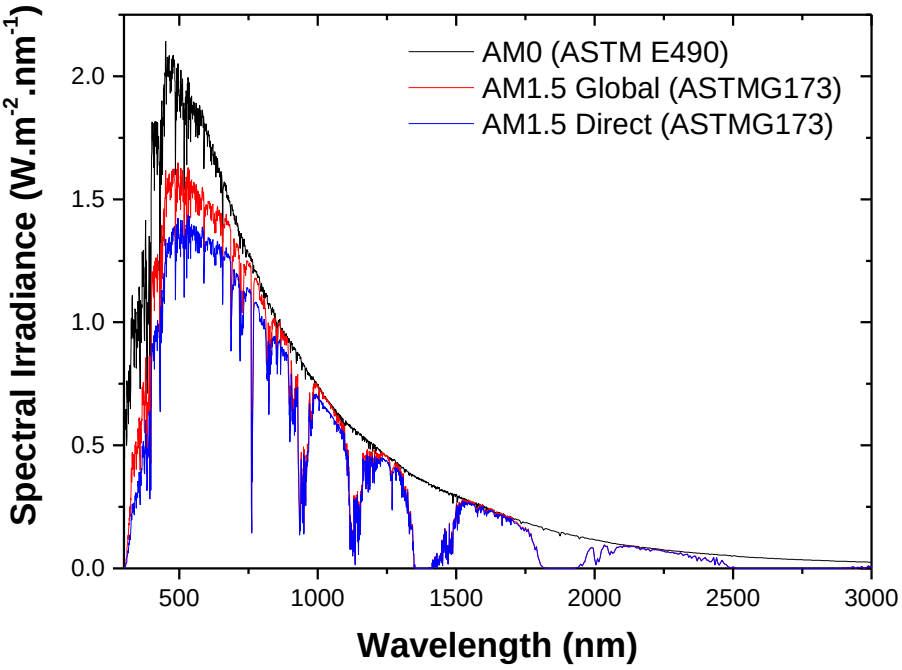

Figure 1.24 AM0 (spectrum outside the Earth's atmosphere), AM1.5 Global and AM1.5 Direct spectra plotted using ASTM data

There are generally two types of experiment to determine the efficiency of a sample. In the first, the photocatalyst or photoelectrode is placed in solution under irradiation and the rate of gas evolution is measured (expressed with units such as $\mu mol.hr^{-1}.g^{-1}$). From this the photocatalytic efficiency can be calculated. Typically the apparent quantum yield (AQY) is quoted which takes into account the number of incident photons (measured using a Si diode):

$$AQY\ (\%) = \frac{\text{Number of reacted electrons}}{\text{Number of incident photons}} \times 100 \tag{1.20}$$

For H_2 production:

$$AQY\ (\%) = \frac{2 \times \text{number evolved } H_2 \text{ molecules}}{\text{Number of incident photons}} \times 100 \tag{1.21}$$

For O_2 production

$$AQY\ (\%) = \frac{4 \times \text{number evolved } O_2 \text{ molecules}}{\text{Number of incident photons}} \times 100 \quad (1.22)$$

The AQY is estimated to be smaller than the total quantum yield due to factors such as scattering by the semiconductor. Although this is a useful metric analogous to a diagnostic current conversion efficiency, the AQY cannot be considered a true power conversion efficiency. Since there is no accounting for the voltage of a particular reaction or product the overall energy efficiency is not accounted for.

If the efficiency of the photoelectrode is measured as part of a photoelectrochemical cell (under 2 electrode conditions) then the observed photocurrent can be used to derive the solar to hydrogen efficiency (STH). The STH efficiency is the most frequently quoted measure of efficiency for photoelectrochemical cells and can be calculated using the product of the voltage, short circuit current and Faradaic efficiency for hydrogen evolution (η_F) under standard state conditions:

$$STH = \left[\frac{\left| j_{SC} (mA.cm^{-2}) \right| \times (1.23\ V) \times \eta_F}{P_{total}\ (mW.cm^{-2})} \right]_{AM1.5\ G} \quad (1.23)$$

The short circuit current, j_{SC} ($mA.cm^{-2}$), is the current at 0 V normalised to the illuminated electrode area and the voltage is the thermodynamic water splitting potential, 1.23 V. P_{total} refers to the total integrated power input density of the impinging illumination. The STH measure is only valid if the Faradaic efficiency is 1 (giving a 1:2 ratio for O_2:H_2 evolution) and no sacrificial reagents are used.

Unfortunately not all photoelectrodes are able to split water under short-circuit conditions and the additional overpotential required may need to be provided by the application of an external electrical bias. In this case the applied bias photon-to-current efficiency (ABPE) can be measured. It should be recognised if an applied bias greater than 1.23 V is required for the observation of water splitting, this brings into question the advantage of PEC over standard electrolysis in the dark.

$$ABPE = \left[\frac{\left| j_{ph} (mA.cm^{-2}) \right| \times (1.23 - |V_b|)\ (V) \times \eta_F}{P_{total}\ (mW.cm^{-2})} \right]_{AM1.5\ G} \quad (1.24)$$

Where j_{ph} is the photocurrent density under an applied bias, V_b. Again the ABPE should be reported versus the counter electrode and not the reference electrode which would result in an interface measurement and not a device measurement.

The final efficiency metric which will be considered is the incident photon-to-current efficiency (IPCE). The IPCE describes the photocurrent collected per incident photo as a function of the illumination wavelength. As seen in equation 1.11, the IPCE takes into account three fundamental processes involved in PEC including the photon absorbance, charge transport to the semiconductor/ electrolyte interface and charge transfer into the electrolyte. The photocurrent is measured under monochromatic illumination and often these values are used to predict the photocurrent under actual solar irradiation.

$$IPCE = \frac{\left|j_{ph}(mA.cm^{-2})\right| \text{ x } 1239.8 \text{ (V.nm)}}{P_{mono} \text{ (mW.cm}^{-2}) \text{ x } \lambda \text{ (nm)}} \quad (1.25)$$

1.6 Summary

This introductory section has touched upon the processes behind the water splitting reaction, both in the photocatalyst as well as the cell and the techniques available for evaluating efficiencies. Different cell configurations have been discussed which play an important role in commercialisation of the technology. In the first of the experimental sections the photoelectrochemical photodiode will be explored along with the CVD synthesis and characterisation of TiO_2, B-TiO_2 and B,N-TiO_2. The following experimental section will explore the use of PV-PEC tandem devices along with fabricated using CVD of Fe_2O_3 thin films onto commercially available a-Si devices. In the final experimental section, synthesis of the relatively overlooked semiconductor boron phosphide will be explored, along with its use in a photocatalyst suspension.

1.7 References

1. U. N. Foundation, Sustainable Energy for All, http://www.se4all.org/.
2. *KeyWorld Energy Statistics 2014*, The International Energy Agency, 2014.
3. J. H. Conti, P.; Beamon, J. A.; Napolitano, S.; Schaal, A. M.; Turnure, J. T.; Westfall, L. , 2013.
4. R. van de Krol and M. Grätzel, in *Photoelectrochemical Hydrogen Production*, eds. R. van de Krol and M. Grätzel, Springer US, 2012, vol. 102, ch. 1, pp. 3-11.
5. P. Tans, NOAA/ESRL, 2015.
6. R. K. R. Pachauri, A, *IPCC Fourth Assessment Report (AR4)*, IPCC, 2007.
7. C. McGlade and P. Ekins, *Nature*, 2015, 517, 187-190.
8. J. R. Petit, J. Jouzel, D. Raynaud, N. I. Barkov, J. M. Barnola, I. Basile, M. Bender, J. Chappellaz, M. Davis, G. Delaygue, M. Delmotte, V. M. Kotlyakov, M. Legrand, V. Y. Lipenkov, C. Lorius, L. Pepin, C. Ritz, E. Saltzman and M. Stievenard, *Nature*, 1999, 399, 429-436.
9. P. K. Tans, Ralph, Trends in Atmospheric Carbon Dioxide, www.esrl.noaa.gov/gmd/ccgg/trends/.
10. T. Randall, Fossil Fuels Just Lost the Race Against Renewables, http://www.bloomberg.com/news/articles/2015-04-14/fossil-fuels-just-lost-the-race-against-renewables.
11. Fossil Free - Commitments, http://gofossilfree.org/commitments-new/, Accessed 17th July, 2015.
12. Renewable Energy FAQ's, http://www.iea.org/aboutus/faqs/renewableenergy/.
13. N. S. Lewis, *MRS Bull.*, 2007, 32, 808-820.
14. C. Philibert, *Technology Roadmap: Solar Photovoltaic Energy*, International Energy Agency, 2014.
15. J. L. Sawin, *Renewables 2015 Global Status Report*, REN21, 2105.
16. G. D. Barbose, N.; Wiser, R., *Tracking the Sun V: An Historical Summary of the Installed Price of Photovoltaics in the United States from 1998 to 2011*, Lawrence Berkeley National Laboratory, 2012.
17. C. Philibert, *Technology Roadmap: Solar Thermal Electricity*, International Energy Agency, 2014.
18. Calculation of Solar Insolation, http://www.pveducation.org/pvcdrom/properties-of-sunlight/calculation-of-solar-insolation, Accessed 28th July, 2015.
19. Packing Some Power, http://www.economist.com/node/21548495.
20. J. Barber, *Inorg. Chem.*, 2008, 47, 1700-1710.
21. J. Barber, *Chem. Soc. Rev.*, 2009, 38, 185-196.
22. Y. Tachibana, L. Vayssieres and J. R. Durrant, *Nat. Photonics*, 2012, 6, 511-518.
23. C. A. S. Hall, B. E. Dale and D. Pimentel, *Sustainability*, 2011, 3, 2413-2432.
24. C. Liu, J. J. Gallagher, K. K. Sakimoto, E. M. Nichols, C. J. Chang, M. C. Y. Chang and P. D. Yang, *Nano Letters*, 2015, 15, 3634-3639.
25. S. Licht, B. Wang, S. Mukerji, T. Soga, M. Umeno and H. Tributsch, *Int. J. Hydrog. Energy*, 2001, 26, 653-659.
26. B. Parkinson and J. Turner, in *Photoelectrochemical Water Splitting: Materials, Processes and Architectures*, The Royal Society of Chemistry, 2013, DOI: 10.1039/9781849737739-00001, pp. 1-18.

27. G. Simbolotti, *IEA Energy Technology Essentials - Hydrogen Production and Delivery*, The International Energy Agency, 2007.
28. L. M. Peter, *Electroanalysis*, 2015, 27, 864-871.
29. Hydrogen Storage, http://energy.gov/eere/fuelcells/hydrogen-storage, Accessed 5th August, 2015.
30. *Multi-Year Research, Development and Demonstration Plan Executive Summary*, Fuel Cell Tehnologies Office, US Department Of Energy, 2012.
31. R. de Levie, *J. Electroanal. Chem.*, 1999, 476, 92-93.
32. A. Fujishima and K. Honda, *Nature*, 1972, 238, 37-+.
33. J. G. Mavroides, J. A. Kafalas and D. F. Kolesar, *Appl. Phys. Lett.*, 1976, 28, 241-243.
34. J. Li and N. Wu, *Catalysis Science & Technology*, 2015, 5, 1360-1384.
35. Z. Chen, T. Deutsch, H. Dinh, K. Domen, K. Emery, A. Forman, N. Gaillard, R. Garland, C. Heske, T. Jaramillo, A. Kleiman-Shwarsctein, E. Miller, K. Takanabe and J. Turner, in *Photoelectrochemical Water Splitting*, Springer New York, 2013, DOI: 10.1007/978-1-4614-8298-7_1, ch. 1, pp. 1-5.
36. T. L. Gibson and N. A. Kelly, *Int. J. Hydrog. Energy*, 2008, 33, 5931-5940.
37. G. Peharz, F. Dimroth and U. Wittstadt, *Int. J. Hydrog. Energy*, 2007, 32, 3248-3252.
38. B. A. Pinaud, J. D. Benck, L. C. Seitz, A. J. Forman, Z. Chen, T. G. Deutsch, B. D. James, K. N. Baum, G. N. Baum, S. Ardo, H. Wang, E. Miller and T. F. Jaramillo, *Energy Environ. Sci.*, 2013, 6, 1983-2002.
39. O. Khaselev and J. A. Turner, *Science*, 1998, 280, 425-427.
40. M. Ni, M. K. H. Leung, D. Y. C. Leung and K. Sumathy, *Renewable & Sustainable Energy Reviews*, 2007, 11, 401-425.
41. K. Maeda, *Journal of Photochemistry and Photobiology C-Photochemistry Reviews*, 2011, 12, 237-268.
42. A. Koca and M. Sahin, *Int. J. Hydrog. Energy*, 2002, 27, 363-367.
43. A. Paracchino, V. Laporte, K. Sivula, M. Gratzel and E. Thimsen, *Nat. Mater.*, 2011, 10, 456-461.
44. S. Hu, M. R. Shaner, J. A. Beardslee, M. Lichterman, B. S. Brunschwig and N. S. Lewis, *Science*, 2014, 344, 1005-1009.
45. T. J. Jacobsson, V. Fjallstrom, M. Sahlberg, M. Edoff and T. Edvinsson, *Energy Environ. Sci.*, 2013, 6, 3676-3683.
46. T. J. Jacobsson, C. Platzer-Bjorkman, M. Edoff and T. Edvinsson, *Int. J. Hydrog. Energy*, 2013, 38, 15027-15035.
47. T. J. Jacobsson, V. Fjallstrom, M. Edoff and T. Edvinsson, *Energy Environ. Sci.*, 2014, 7, 2056-2070.
48. L. Liao, Q. Zhang, Z. Su, Z. Zhao, Y. Wang, Y. Li, X. Lu, D. Wei, G. Feng, Q. Yu, X. Cai, J. Zhao, Z. Ren, H. Fang, F. Robles-Hernandez, S. Baldelli and J. Bao, *Nat Nano*, 2014, 9, 69-73.
49. D. M. Fabian, S. Hu, N. Singh, F. A. Houle, T. Hisatomi, K. Domen, F. Osterloh and S. Ardo, *Energy Environ. Sci.*, 2015, DOI: 10.1039/C5EE01434D.
50. D. M. K. Blake, C., *Hydrogen reactor development and design for photofermentation and photolytic processes*, The National Renewable Energy Lab, 2005.
51. J. B. M. Goodall, S. Kellici, D. Illsley, R. Lines, J. C. Knowles and J. A. Darr, *RSC Adv.*, 2014, 4, 31799-31809.
52. B. L. Kroposki, J.; Harrison, K.; Sen, P. K.; Novachek, F., *Electrolysis: Information and Opportunities for Electric Power Utilities*, The National Renewable Energy Lab, 2006.

53. H. Liu, J. Yuan and W. F. Shangguan, *Energy Fuels*, 2006, 20, 2289-2292.
54. A. A. Nada, M. H. Barakat, H. A. Hamed, N. R. Mohamed and T. N. Veziroglu, *Int. J. Hydrog. Energy*, 2005, 30, 687-691.
55. M. Bowker, *Green Chem.*, 2011, 13, 2235-2246.
56. H. Q. Lu, J. H. Zhao, L. Li, L. M. Gong, J. F. Zheng, L. X. Zhang, Z. J. Wang, J. Zhang and Z. P. Zhu, *Energy Environ. Sci.*, 2011, 4, 3384-3388.
57. A. Kudo, H. Kato and I. Tsuji, *Chemistry Letters*, 2004, 33, 1534-1539.
58. T. Sakata and T. Kawai, *Nouveau Journal De Chimie-New Journal of Chemistry*, 1981, 5, 279-281.
59. T. Kawai and T. Sakata, *Nature*, 1980, 286, 474-476.
60. T. Kawai and T. Sakata, *Nature*, 1979, 282, 283-284.
61. T. Kawai and T. Sakata, *Chemistry Letters*, 1981, DOI: 10.1246/cl.1981.81, 81-84.
62. M. Hoffmann, Durban, South Africa, 2012.
63. T. Stecker, Build a Better Toilet to Get Rich and Popular, http://www.scientificamerican.com/article/build-a-better-toilet-to-get-rich-and-popular/.
64. A. L. Patterson, *Phys. Rev.*, 1939, 56, 978-982.
65. J. I. Langford and A. J. C. Wilson, *J. Appl. Crystallogr.*, 1978, 11, 102-113.
66. C. Barret and T. B. Massalski, *Structure of Metals*, Pergamon, 1980.
67. Z. Chen, T. Deutsch, H. Dinh, K. Domen, K. Emery, A. Forman, N. Gaillard, R. Garland, C. Heske, T. Jaramillo, A. Kleiman-Shwarsctein, E. Miller, K. Takanabe and J. Turner, in *Photoelectrochemical Water Splitting*, Springer New York, 2013, DOI: 10.1007/978-1-4614-8298-7_5, ch. 5, pp. 49-62.
68. D. L. Wood and J. Tauc, *Physical Review B*, 1972, 5, 3144-&.
69. E. A. Davis and N. F. Mott, *Philosophical Magazine*, 1970, 22, 903-&.
70. S. M. Sze and K. K. Ng, in *Physics of Semiconductor Devices*, John Wiley & Sons, Inc., 2006, DOI: 10.1002/9780470068328.ch1, pp. 5-75.
71. H. Gerischer, *Electrochimica Acta*, 1990, 35, 1677-1699.
72. R. Krishnan, in *Encyclopedia of Electrochemistry*, Wiley-VCH Verlag GmbH & Co. KGaA, 2007, DOI: 10.1002/9783527610426.bard060001.
73. R. van de Krol, in *Photoelectrochemical Hydrogen Production*, eds. R. van de Krol and M. Grätzel, Springer US, 2012, vol. 102, ch. 2, pp. 13-67.
74. A. J. Nozik, *Annu. Rev. Phys. Chem.*, 1978, 29, 189-222.
75. Y. Xu and M. A. A. Schoonen, *Am. Miner.*, 2000, 85, 543-556.
76. S. Burnside, J. E. Moser, K. Brooks, M. Gratzel and D. Cahen, *J. Phys. Chem. B*, 1999, 103, 9328-9332.
77. A. B. Murphy, P. R. F. Barnes, L. K. Randeniya, I. C. Plumb, I. E. Grey, M. D. Horne and J. A. Glasscock, *Int. J. Hydrog. Energy*, 2006, 31, 1999-2017.

2 The 'Photodiode': TiO_2 and Anion Doped TiO_2 on Steel

Three different types of device design for photo-driven water splitting were introduced in the opening chapter of this thesis: the PV+electrolyser, the integrated photoelectrochemical array and the photocatalyst suspension. This chapter will explore the use of one type of integrated photoelectrochemical array, the water splitting 'photodiode', a term coined by Mills et al.[1, 2] Integrated PEC devices combine the harnessing of solar energy and electrolysis of water into a single device and are characterised by intermediate efficiency and cost between the prohibitively expensive PV+electrolyser systems and low efficiency photocatalyst suspensions. The application of a commonly used water splitting photocatalyst, titanium dioxide, in the photodiode system will be investigated.

Titanium dioxide has attracted much attention as a water splitting catalyst since this property was first demonstrated by Honda and Fujishima in 1972.[3] Despite this, the wide band-gap of TiO_2 (3.0 eV for rutile and 3.2 eV for anatase) limits the material's potential efficiency to around 1%,[4] thus chemical doping of TiO_2 will be explored in the hope of improving the overall water splitting activity of the material by modifying the light absorption properties (i.e. narrowing the band gap to facilitate greater solar light absorption). Two types of anion doped TiO_2 will be investigated: B-TiO_2 and co-doped B,N-TiO_2, both deposited using atmospheric pressure chemical vapour deposition (APCVD).

2.1 Introduction

2.1.1 The Photodiode

A photoelectrochemical photodiode consists of a metal substrate coated with a semiconductor photocatalyst. Most famously modelled by Schottky and Mott, the formation of a metal-semiconductor junction can result in either a rectifying contact, (in which current can pass in only one direction), or an ohmic contact (in which current can pass in either direction). Whether the contact is rectifying or ohmic depends on the magnitude of the work function, Φ, of the metal and the semiconductor. For an n-type semiconductor if $\Phi_M > \Phi_S$, then the bands of the semiconductor are bent upwards at the

interface and the junction has rectifying properties. If $\Phi_M<\Phi_S$ then a downward bending of the semiconductor bands is observed leading to an ohmic contact. Since for n-type semiconductors in nearly all cases $\Phi_M>\Phi_S$, most metal-semiconductor combinations form rectifying contacts. For a p-type semiconductor the opposite is true and usually $\Phi_M<\Phi_S$ but as holes have difficulty in passing underneath a barrier, rectifying contacts are nearly always formed. For an in-depth explanation of the formation of metal-semiconductor contacts the reader is referred to an excellent review article by Rhoderick,[5] but a brief overview in the context of an n-type semiconductor will be given here.

When a metal and a semiconductor are brought together, there is an equilibration between the Fermi level of the semiconductor and the Fermi level of the metal. For an n-type semiconductor, the Fermi level of the metal usually lies below that of the semiconductor thus equilibration occurs via electron flow from the semiconductor into the metal. This causes a fall in the chemical potential of the semiconductor in the region close to the metal-semiconductor interface, (termed the depletion region or space charge region), as it becomes depleted of electrons. The energy of the Fermi level of the metal is not appreciably affected as there are over 10^{10} times more valence electrons in the metal than there are conduction electrons in the semiconductor before contact,[6] thus the electric potential generated between the metal and semiconductor on contact causes a deformation in the bands of the semiconductor close to the metal-semiconductor interface.

In the bulk of the semiconductor there is an overall downward displacement in energy of the bands and at the metal-semiconductor interface the semiconductor bands are pinned due to a high density of surface states. This results in an upward bending of the semiconductor bands, creating a potential barrier for further electron transfer, Figure 2.1. The amount by which the bands are bent upwards (the so-called diffusion potential, V_{do}), is given by:[5]

$$V_{do} = \phi_M - \phi_S \qquad (2.1)$$

What is usually quoted is not the diffusion potential, but the barrier height Φ_B as viewed from the metal. For an n-type semiconductor, this is given by:

$$\phi_B = \phi_M - \chi \tag{2.2}$$

Where χ is the electron affinity of the semiconductor. Equation 2.2 is referred to as the Schottky-Mott approximation and correctly predicts the presence of band-bending in the semiconductor, but due to Fermi-level pinning caused by the presence of surface states, it incorrectly predicts the height of the Schottky barrier which actually has a much weaker dependence on the metal work function.

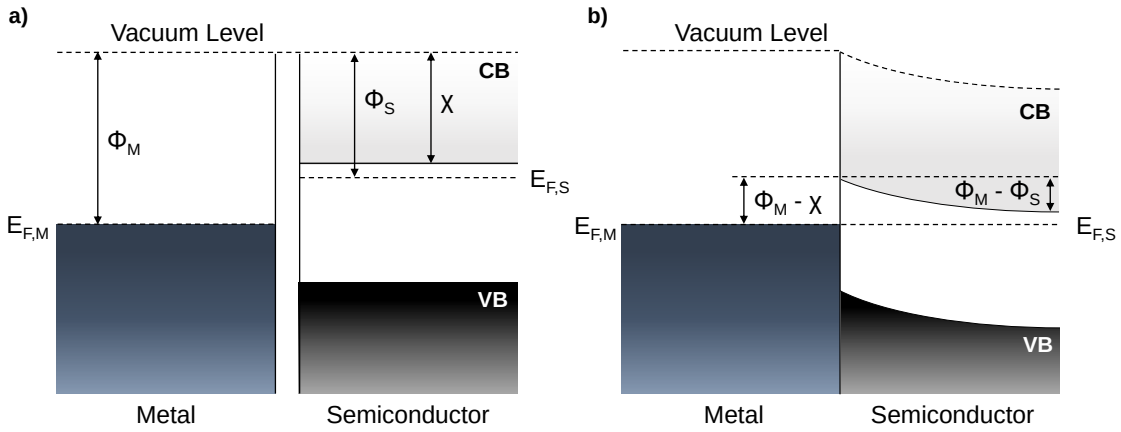

Figure 2.1 Band diagram for a rectfying metal-semiconductor junction a) before and b) after contact

The rectifying nature of metal-semiconductor contacts is exploited in the water splitting photodiode and gives rise to vectorial separation of electrons and holes in the device. In the water splitting photodiode, a photocatalyst is coated onto one side of a metal substrate and a co-catalyst onto the other. When the photocatalyst is irradiated with light greater than its band gap energy, electron and hole pairs are generated. The photogenerated electrons are transported through the metal substrate to the reverse side, where water is reduced over a co-catalyst. The concomitant holes are swept to the photocatalyst/ electrolyte interface where the water oxidation reaction is carried out. This layered structure can be sandwiched between the two compartments allowing for the distinct production of hydrogen and oxygen, minimising the back reaction and cutting out the need for costly gas separation, Figure 2.2.

This concept was first adopted by Anpo and co-workers, who developed a so-called H-type glass reactor in which a photodiode-type device was sandwiched between two compartments connected with a proton exchange membrane.[7-9] Their devices

typically consisted of visible light-responsive titanium dioxide deposited onto titanium foil using radio-frequency magnetron sputtering which had platinum nanoparticles loaded onto the reverse.[10] Reactions were carried out using 1.0 M NaOH in the TiO_2 compartment and 0.5 M H_2SO_4 in the Pt compartment, thereby obtaining a chemical bias of 0.83 V, ($\Delta E = 0.059 \times \Delta pH$), to assist the electron transfer from TiO_2 to Pt. This is a distinct advantage of the two-compartment cell and simplifies the overall device design as the need for an external electrical bias is minimised. Modest efficiencies and stoichiometric H_2 and O_2 evolution could be obtained from the system. It was shown that the photocatalytic activity of the vis-TiO_2 was enhanced following treatment of the surface with HF and on irradiation with a solar concentrator system, AQYs of 0.38 % were obtained.[11]

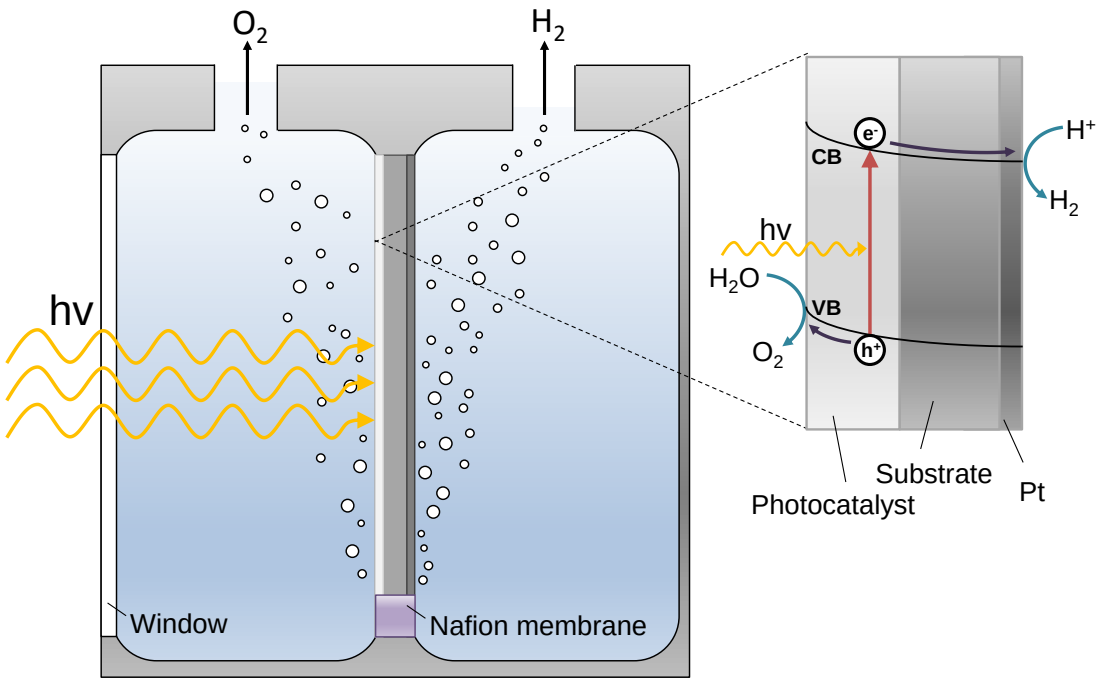

Figure 2.2 Representation of a photodiode for water oxidation and reduction in a 2-compartment cell, showing schematic of band structure (not absolute band positions) and vectorial separation of holes and electrons

The effect of the work function of the metal substrate on the overall photocatalytic activity of the device was investigated. Although Φ_M has minimal effect on the Schottky barrier height between the metal and semiconductor, it does affect the width of the depletion region.[12] Anpo and co-workers showed that photocatalytic activity of the vis-TiO_2 device increased significantly with a decrease in the substrate

work function.[7] This trend was also observed by Freitag and co-workers who investigated the degradation of organic compounds by TiO_2 deposited onto various metal substrates and found decreased photonic efficiency with increased work function.[12, 13]

2.1.2 TiO_2

Titanium dioxide has a long and fascinating history. Though the white powder had inadvertently been used as a pigment since ancient times,[14] it wasn't until the late 18th century that TiO_2 was identified and reported by a vicar in Cornwall.[15] A high refractive index, (n = 2.65 for rutile[16]), and its absorption solely in the UV region gives TiO_2 its white colour and this property has been utilised in numerous applications such as in pigments,[17] paints,[18] food colouring,[19] toothpaste[20] as well as in sunscreens.[21] The most remarkable property of TiO_2 however is its ability to act as a photocatalyst - a catalyst able to produce, upon absorption of light, chemical transformations of the reaction partners. This was first experienced when using TiO_2 as an additive in paints, where it was observed to cause bleaching and flaking.[22] An early study in 1938 reported the bleaching of dyes by TiO_2,[14] since which there have been many studies on the ability of TiO_2 to catalyse the break down organic materials, but that is not within the scope of this work and is covered in several reviews.[23-27]

2.1.2.1 Physical Properties of TiO_2

Undoped TiO_2 is intrinsically an n-type semiconductor with three crystalline polymorphs at ambient conditions: rutile, anatase and brookite (although brookite is not commonly observed). Both brookite and anatase are metastable phases which convert to the thermodynamically stable rutile on heating,[28] however anatase is often formed first at lower temperatures.

TiO_2 is comprised of chains of TiO_6 octahedra where each Ti^{4+} ion is surrounded by six O^{2-} ions. The polymorphs differ by the distortion of each octahedron and the assembly of the octahedral chains. In rutile, the octahedron has a slight orthorhombic distortion and is in contact with ten neighbouring octahedrons. Anatase on the other hand shows significant distortion and each octahedron is in contact with only eight neighbours. The unit cells of anatase and rutile are shown in Figure 2.3.

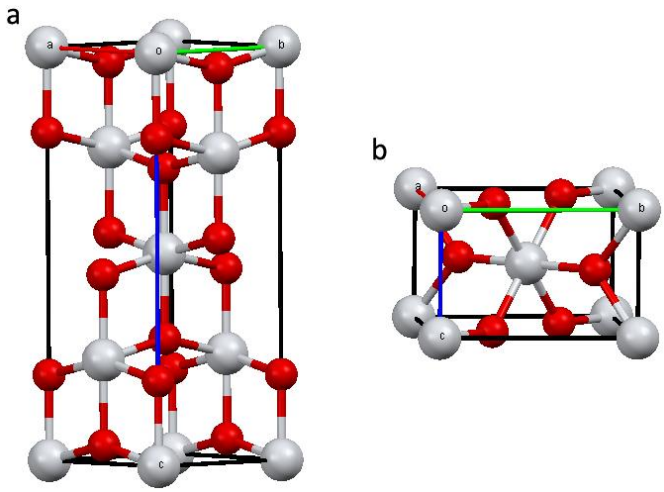

Figure 2.3 The unit cells of a) anatase and b) rutile where Ti atoms are white and oxygen atoms red

This distortion leads anatase to have shorter Ti-O distances but longer Ti-Ti distances making it less dense than rutile: 3.83 vs. 4.24 g/cm^3.[16] The optical properties are also affected; rutile has a higher refractive index than anatase[29] and a smaller band gap. The valance and conduction band positions also slightly vary between the two phases, which plays a crucial role in the material's ability to split water. Due to the position of the rutile conduction band, it is unable to split water without the use of an external bias,[30] as displayed in Figure 2.4.

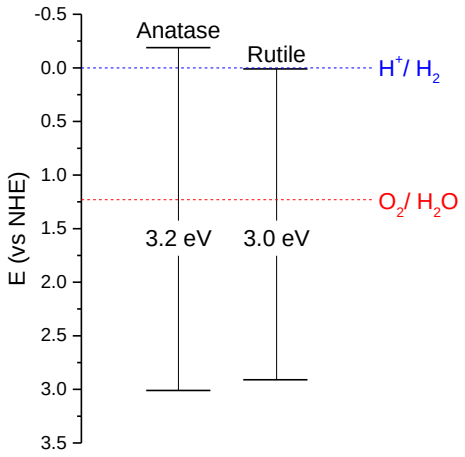

Figure 2.4. Valence and conduction band positions of the rutile and anatase phases of TiO_2. Data adapted from[30]

2.1.2.2 TiO_2 as a Photocatalyst for Water Splitting

Honda and Fujishima first demonstrated photocatalytic water splitting using TiO_2.[3] In the years since there have been considerable efforts in the development of other photocatalysts but TiO_2 still remains amongst the most promising as it is not only photocatalytically active but also biologically and chemically inert, cheap and easy to produce. One of the main advantages TiO_2 has is the fact that it does not undergo photocorrosion under typical operating conditions. The lifetime of any device for commercialisation plays very important role. For example, Turner's 'Artificial Leaf' based on III/V semiconductors had a 12.4 % efficiency but a lifetime of only around 20 hours,[31] making it impractical for real life application. Though the efficiency of Turner's 'Artificial Leaf' completely dwarfs the 0.1 % quantum efficiency reported by Honda and Fujishima in their initial work, the superior lifetime of TiO_2 offers a clear advantage.

2.1.2.3 Modification of TiO_2 for Visible Light Photocatalysis

Perhaps the biggest hindrance in the application of TiO_2 is that it is a wide band gap semiconductor and only absorbs light in the UV region, accounting for about 5% of the total energy of the solar spectrum. As a result considerable efforts have been made to improve the visible light absorption of TiO_2, including surface sensitisation using dyes and chemical doping. Surface sensitisation can be an effective way of extending the absorption of TiO_2 into the visible range but the dyes can themselves be degraded by TiO_2 and so this technique will not be discussed here but can be explored in a review on TiO_2 photocatalysis.[32]

2.1.2.4 Metal Doping and Ion Implantation

In order to decrease the band-gap of TiO_2, metal cation doping (where the metal ion is doped substitutionally for Ti^{4+}) has been extensively explored and was the focus of many early doping studies. Choi et al. doped TiO_2 with 21 different metal ions and compared their photoreactivity using $CHCl_3$ oxidation.[33] They were able induce a visible light response and in the case of V, Fe, Mo, Ru, Rh and Re the photocatalytic activity was improved, but the addition of Co and Al actually decreased efficiency. They concluded that the efficiency of a metal ion dopant depended on whether it acted to

improve interfacial charge transfer or acted as a recombination centre. Despite some metal ions being able to improve the photocatalytic response into the visible region, generally metal ion doping is detrimental as the dopants create a charge unbalance, e.g. with Cr^{3+} or Ni^{2+}, and act as recombination centres between electrons and holes.[34] In order to circumvent this charge imbalance, co-doping can be employed. Kudo et al. investigated the water oxidation activity of TiO_2 doped with Rh^{3+}/ Sb^{5+} and found doping the elements individually into the TiO_2 lattice had a negative effect on photocatalytic activity, but when doped in combination, improved oxygen production rates were observed.[35]

Another cation-doping technique that has been developed in recent years is metal ion implantation, where TiO_2 is bombarded with metal ions which inject into the TiO_2 lattice.[36] It has been shown that Cr ion implantation can extend light absorption into the red region and that Cr-TiO_2 is an active photocatalyst when irradiated with both UV and visible light.[37, 38] The Cr ions did not act as recombination centres, contrary to when they were chemically doped into the lattice and it was thought that the electronic structure of the material was modified in a different way for the two techniques.

2.1.2.5 Non-metal doping

Due to the drawbacks commonly associated with cation doping of titanium dioxide such as poor thermostability and high modification costs, focus has shifted onto anion doping TiO_2 with elements such as N,[39] S,[40] C,[41] F,[42] B.[43] Anion dopants are typically incorporated into the TiO_2 lattice in a position substitutional for O^{2-}. Since the conduction band edge of TiO_2 is primarily comprised of O 2p orbitals, mixing of the dopant anion 2p orbitals with the 2p states of O extends the valence band edge towards higher energies, narrowing the band gap of titania.[39] These dopant ions can also enter the TiO_2 lattice in an interstitial position (between Ti-O bridges) which typically results in inter-band states between the valence and conduction band.

Due to its comparable atomic size with oxygen, small ionisation energy and high stability, nitrogen is by far the most widely studied anion dopant for TiO_2 and has been shown as an effective dopant in enhancing the visible light absorption and photocatalytic activity of TiO_2.[44] Despite this there is little consensus on whether interstitial or substitutional doping yields the more effective visible light photocatalyst.[39,

[45-48] It has also been suggested that it is the indirect formation of oxygen vacancies upon nitrogen doping TiO_2 that is responsible for visible light absorption enhancement.[49] Nitrogen doping has been experimentally shown to introduce lower energy sites for electron-hole recombination processes to occur,[48] thus a trade-off exists in N-doped TiO_2 between the extent of bandgap narrowing and the detrimental effect of recombination.

Boron doping of TiO_2 on the other hand is much less researched but is an attractive candidate, especially as there have been reports of improved UV as well as visible light-driven activity.[50] Boron doping was first investigated by Moon and co-workers who synthesised powders of B-doped TiO_2 using a sol-gel method.[51, 52] Though they did not fully characterise the amount of dopant present or its oxidation state, they were able to show improved visible light absorption as well as the suppression of the parasitic back reaction between H_2 and O_2, which they stipulated was due to the presence of a thin layer of B_2O_3 on the surface the B/TiO_2 particles.

A recent study analysed the generation of photocurrent in B-doped and pristine TiO_2 nanotubes.[53] A titanium substrate was anodised and annealed to obtain crystalline nanotubes, then treated with trimethyl borate, ($B(OCH_3)_3$), to introduce the dopant. The total concentration of boron in the samples was determined using X-ray photoelectron spectroscopy (XPS) and was shown to be around 7%, where the B 1s peak had a binding energy of 192 eV and the Ti^{4+} peak showed no change in binding energy on introduction of the B dopant. The boron doped samples showed increased UV absorption as well as a shift of the absorption into the visible region. Photoelectrochemical measurements of the doped samples in 1 M KOH under UV light (0.75 $mW.cm^{-2}$) showed a 1.6 times higher saturation current than undoped samples. The boron-doped samples also showed improved degradation of organic compounds.

Though the majority of studies have shown improved visible light absorption of B-doped TiO_2 films,[54-58] some researchers have actually observed a blue shift in the absorption.[59, 60] A DFT study showed that only B in a substitutional position would create the mid-gap states that facilitate visible light absorption.[61] This was also confirmed in separate study, where the authors investigated different possible positions for B doped into the TiO_2 lattice.[62] They showed that interstitial doping was the most stable but that the metastable B substitutional for O did indeed create mid-band gap states (Figure 2.5).

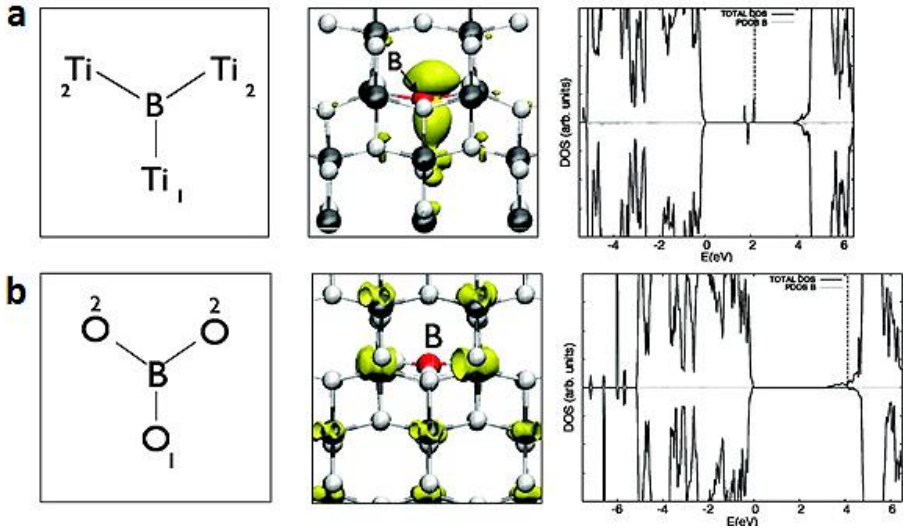

Figure 2.5. Optimal structures of boron doped into anatase and the calculated density of states, a) B substitutional for O and b) interstitial B. Reprinted with permission from.[62] Copyright 2009 American Chemical Society.

The chemical environment of B doped into the TiO_2 lattice has been experimentally investigated using XPS. Elemental boron is known to show a range of binding energies, reported anywhere from 186.4 to 188.4 eV.[63, 64] Similarly there has been an array of values reported for boron doped TiO_2. B-doped TiO_2 powders were synthesied by In et al. who observed two peaks in the B 1s spectra at 193.3 and 190.6 eV.[55] They ascribed the peak at 193.3 eV to an inactive boron oxide-like material which did not contribute to the overall photocatalytic activity (the characteristic peak of B_2O_3 lies at 193.1 eV).[65] The peak at 190.6 eV was thought to be B incorporated into the TiO_2 lattice substitutional for O leading to the presence of mid-gap states that contributed to the photocatalytic activity when tested under visible light. They rationalised the binding energy by comparing it to that of TiB_2, which lies at 187.5 eV,[66] stating that the higher value could be explained by comparatively higher charge transfer to the Ti due to the adjacent electronegative O atoms. The authors did not test the B-TiO_2 photocatalyst under UV light or simulated solar conditions and so no conclusions can be drawn on the overall improvement of the material relative to pristine TiO_2, an unfortunate oversight which is commonplace in testing procedures by many authors.

Chen et al. saw improved UV and visible light activity of B-doped TiO_2 nanoparticles where the broad B 1s XPS peak was at an approximate position of 191 eV which shifted to ~192 eV as the amount of B was increased. The authors described the chemical environment to be similar to that in B_2O_3, which would mean an oxidation

state of B^{3+}.[50] They concluded that the boron was doped into the lattice due to the observed change in properties, but they do not state where the B would lie. Interestingly the authors did not properly resolve their B 1s data, and it appears that they may have more than one peak in the samples with a higher B content and so it is stipulated that they have two B environments, one where B is doped into the lattice substitutional for O and a further boron oxide-like state, as was observed by In et al.

Co-doping of anions into the TiO_2 lattice has also been explored as a technique to modify the electronic structure of TiO_2 and dopant pairs are often chosen to compensate for any excess charge generated by the individual dopants.[54, 67, 68] In particular, B,N co-doped TiO_2 has attracted much attention, especially since the discovery of B,N-doped red anatase by Liu and co-workers.[69] The material had a band-gap gradient from 3.22 eV at the core to as low as 1.94 eV at the surface due to a post synthesis ammonia treatment. Despite the remarkable reduction in the bandgap, only moderate photocurrents were recorded, with a quantum efficiency of ~0.8 % at 0.3 V vs Ag/AgCl under 400 nm irradiation. The B-dopant in particular has been shown to play a synergistic role, where a B-N co-doped sample was fabricated and gave higher hydrogen production rates than nitrogen-only doped TiO_2.[70]

APCVD of B-doped an B,N-co-doped films using $TiCl_4$, ethyl acetate, $B(^iOPr)_3$, t-$BuNH_2$ as precursors will be described in the following section. The relative water splitting activities will be explored in a photodiode configuration, by depositing films onto stainless steel.

2.2 Experimental Methods

Preparation of photodiode: Thin films of boron doped TiO_2 were deposited in a custom-built cold walled CVD reactor using APCVD. The reaction chamber consisted of a quartz tube 330 mm in length and 105 mm in diameter and contained a graphite reactor bed, heated by three Whatman cartridges inserted into the block. Films were deposited onto isopropanol cleaned 304 grade steel substrates of area 25 x 25 mm^2 which had been placed on Pilkington float glass of dimension 220 x 85 mm^2 and fluorine-doped-tin oxide (FTO) subtrates (Pilkington) of area 25 x 25 mm^2 which were placed directly on the graphite block. Titanium(IV) chloride (Aldrich, 99.9%), ethyl acetate (Fischer, reagent grade), triisopropyl borate (Aldrich, 99.9%) and t-butylamine (Aldrich, 98 %) were used as precursors and were located in heated bubblers at 70, 40, 75 and 5 °C respectively. Nitrogen (BOC, 99%) was used as a carrier gas in order to transport the precursors through heated lines, with $TiCl_4$, EtAc and $B(iOPr)_3$ at a flow rate of 0.5 $L.min^{-1}$. The flow rate of t-$BuNH_2$ was varied between 0.05, 0.1 and 0.2 L/min to investigate the effect of concentration. Titanium(IV) chloride and ethyl acetate were introduced into one mixing chamber and triisopropyl borate and t-$BuNH_2$ into a second with additional nitrogen flow rates of 4.8 and 1.6 $L.min^{-1}$, respectively. The mixing chambers were held at 250 °C to avoid condensation of precursors. The two gas flows were then passed through a 2.5 cm baffle manifold into the reaction chamber. Depositions were carried out at 500, 550 and 600 °C for 30s to 3 min. Platinum was then coated onto the reverse side of the substrates in an argon atmosphere using an EMScope SC500 sputter coater at a pressure of 0.1 Torr and current of 35 μA for 4 min.

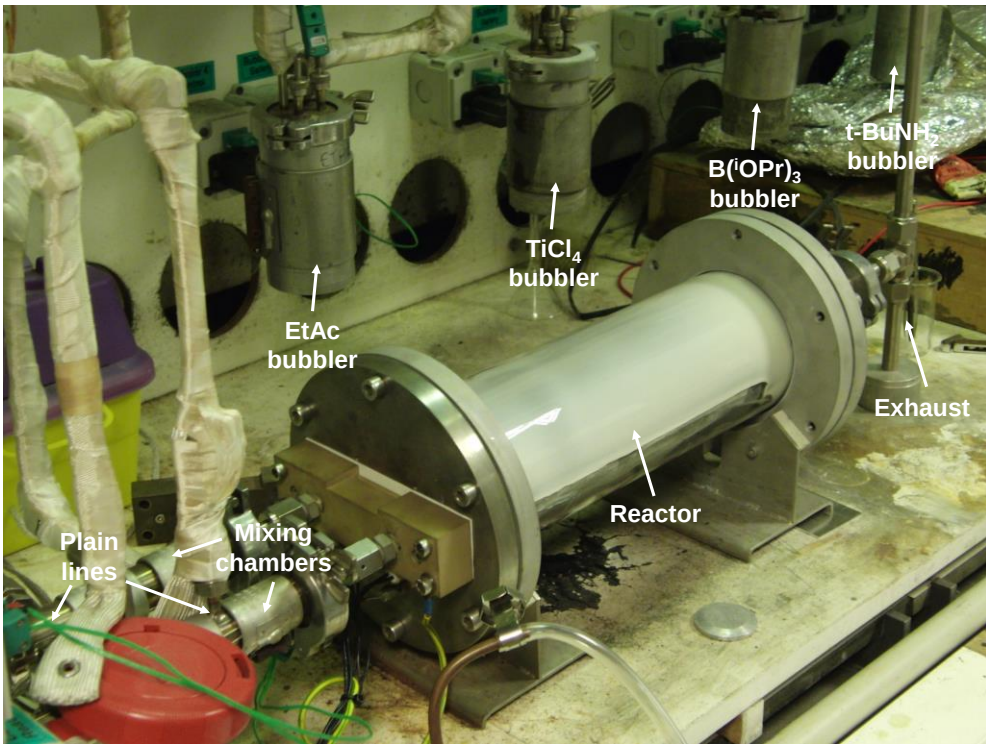

Figure 2.6 Atmospheric pressure CVD rig used for TiO_2 depositions

Characterisation and analysis: To confirm the phase of titania formed, powder X-ray diffraction (PXRD) and Raman spectroscopy were used. PXRD of steel coupons was performed using a Bruker D4 Bragg-Brentano theta-2 theta reflection geometry machine equipped with Cu $K_{\alpha 1+2}$ source powered at 40 kV, 30 mA coupled with a post-sample graphite monochromator and scintillation counter detector. PXRD of films on glass was carried out using a Bruker D8 diffractometer with parallel beam and grazing incidence angle optics equipped with Cu $K_{\alpha 1+2}$ source powered at 40 kV, 40 mA and coupled with a LynxEye silicon strip detector. In both cases scans were performed with a 0.05° step for 2 s/ step and 0.5 slits and for analysis of films on glass a 0.5° incidence angle was used.

Raman spectroscopy was conducted using a Renishaw in Via spectrometer equipped with a 532 nm wavelength laser. X-ray photoelectron spectroscopy (XPS) was used to determine the composition of the films and spectra were recorded on a Kratos Axis Nova spectrometer equipped with a monochromated Al K_{α} X-ray source and delay line detector. Survey spectra were recorded with energy of 160 eV and higher resolution spectra were recorded at 80 eV.

A Filmetrics F20 single spot thin film machine was used to analyse the thicknesses of the samples. Scanning electron microscopy (SEM) was used to observe surface morphology of the films and was carried out using a JEOL 6301 SEM with secondary electron imaging and accelerating voltage of 5 kV. UV-Vis spectra of the films deposited on glass were captured in transmission mode on a PerkinElmer Lambda 25 UV-Vis spectrometer.

Functional testing: The ability of the films to produce hydrogen was tested in 50 mL of a stirred sacrificial solution of 1:1 0.2 M HCl : absolute ethanol. The ethanol was used as a hole scavenger and the remaining photogenerated electrons performed the reduction reaction. The samples were suspended from a rubber septum in a sealed glass vessel equipped with a water cooled jacket and which was filled with 50 mL of sacrificial solution leaving a headspace of 15 mL. They were then irradiated with two 8 W Vilber 365 nm black light lamps with an irradiance of 2 $mW.cm^{-2}$ and 250 µL of gas was collected from the headspace every 15 minutes for two hours and analysed using gas chromatography. In order to quantify the amount of hydrogen present, the counts were compared to a sample of pure hydrogen.

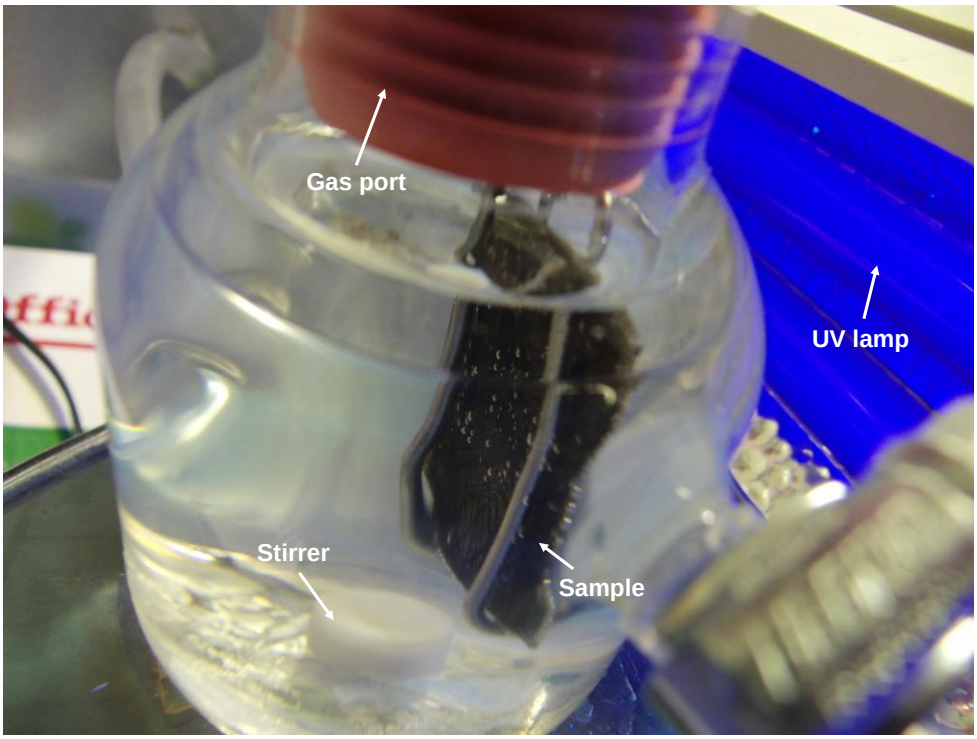

Figure 2.7 Hydrogen evolution test set-up

Oxygen evolution testing was carried out in a sacrificial electron acceptor solution consisting of aqueous solutions of 20 ml of 0.2 M NaOH and 20 ml of 0.02 M $Na_2S_2O_8$. The solution was placed in a gas tight round glass reactor attached to an oxygen electrode (Rank Brothers), under constant stirring. The oxygen concentration in the aqueous phase was measured as an oxygen reducing electrical current using a potentiostat. The photodiode was then immersed into the solution, purged with argon and then re-purged before each irradiation cycle. The sample was irradiated for a set time interval using a 150 W xenon arc lamp equipped with filters (WG 320 and UG5 filters), simulating a UV solar output, with a UVA irradiance of 15 $mW.cm^{-2}$. The irradiation was repeated three times for every sample.

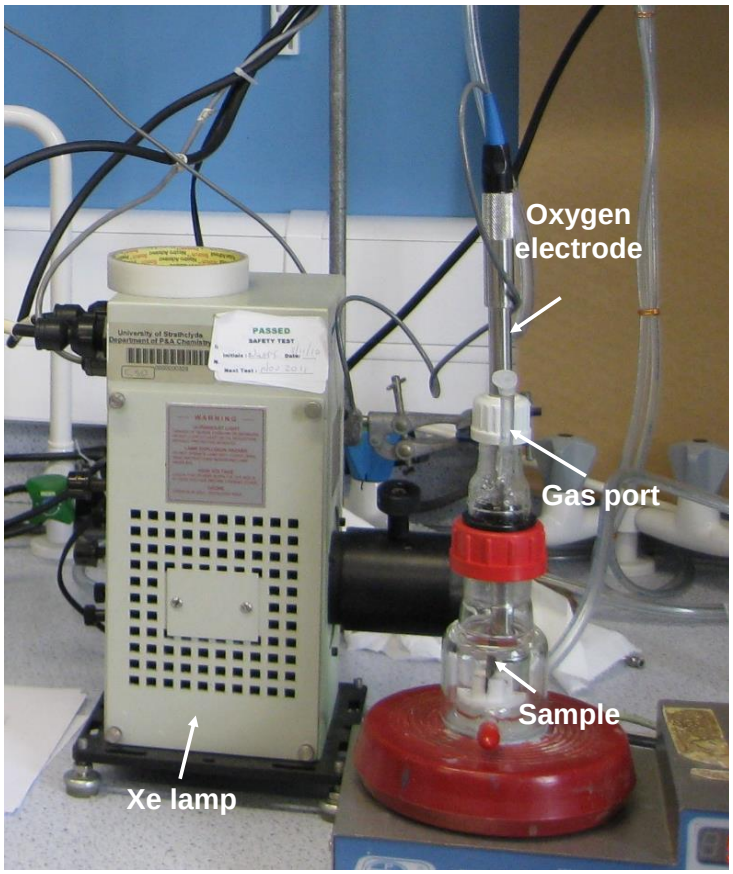

Figure 2.8 Oxygen evolution test set-up

The photocurrent density generated by samples deposited on FTO was recorded using a Metrohm Autolab potentiostat. Samples were placed in a three electrode glass cell using an $Ag/AgNO_3$ reference electrode (via a Luggin capillary), Pt wire counter electrode (area ca. 1.6 cm^2) and working electrode (area ca. 3.2 cm^2). An aqueous 0.1 M

KNO_3 was used as an electrolyte (pH ca. 5.5). The potential range (usually -0.8 to 1.0 V) was scanned at 50 $mV.s^{-1}$ and three cycles were completed; the first two with light being chopped and the last one with light on (note: sample was always in dark when the potential was swept in the negative direction). A 200 W xenon arc lamp was used to illuminate the sample. UG320 and UG5 band-pass filters were used to simulate the sun's UV profile with an irradiance of 10 $mW.cm^{-2}$.

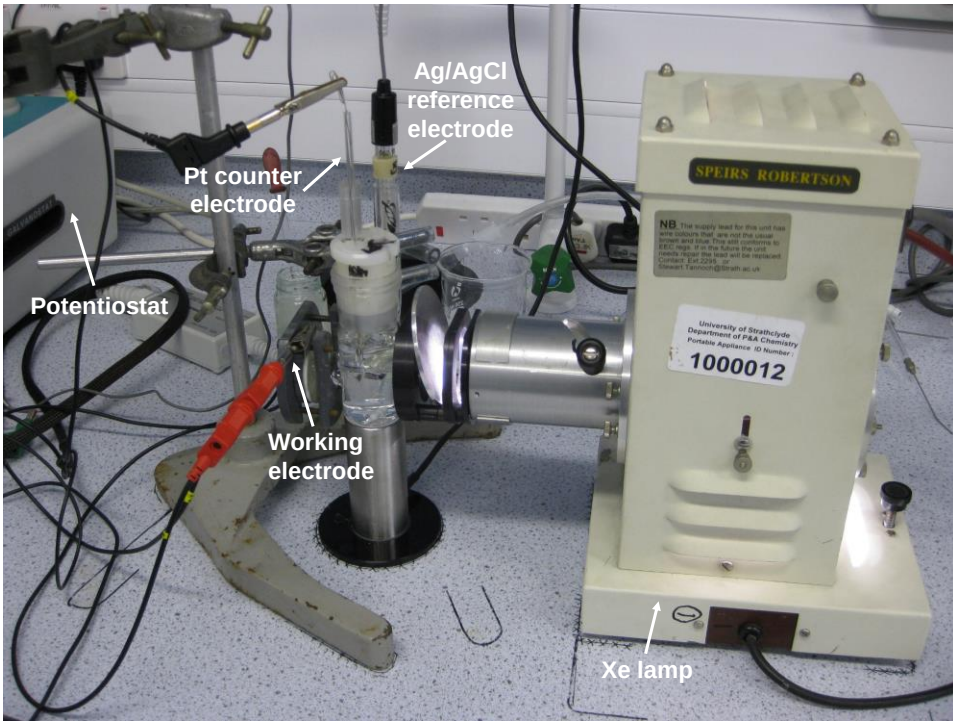

Figure 2.9 Photoelectrochemical testing set-up

2.3 Results and Discussion

2.3.1 TiO_2 and B-TiO_2

2.3.1.1 Structural Characterisation

Firstly the effect of boron doping was investigated to optimise the films prior to the introduction of an additional N-dopant. Non-doped TiO_2 and B-doped TiO_2 films were deposited onto steel substrates using APCVD at 500, 550 and 600 °C, with thicknesses between 200 - 1500 nm. The films were crack-free and well adhered, with no evidence of delamination on application of the Scotch tape test. The thinner films were deposited for functional testing as it has been shown that ~200 nm is an optimum thickness for the TiO_2 photocatalyst in a water-splitting diode.[2] The thickest films were selected for detailed powder X-ray diffraction studies, which revealed crystalline material; films deposited at 500 and 550 °C corresponded to anatase, as observed previously,[71] and those deposited at 600 °C were rutile, TiO_2 (Figure 2.10).

No additional phases were observed in any spectra, (and in particular no crystalline B_2O_3), indicating any boron present is incorporated into the TiO_2 lattice, is an amorphous form, or is below the detection limit. Diffraction patterns were also taken of the thinner films and were found to contain the same phases and relative intensities though were generally poorer quality due to higher background signal from the steel substrate.

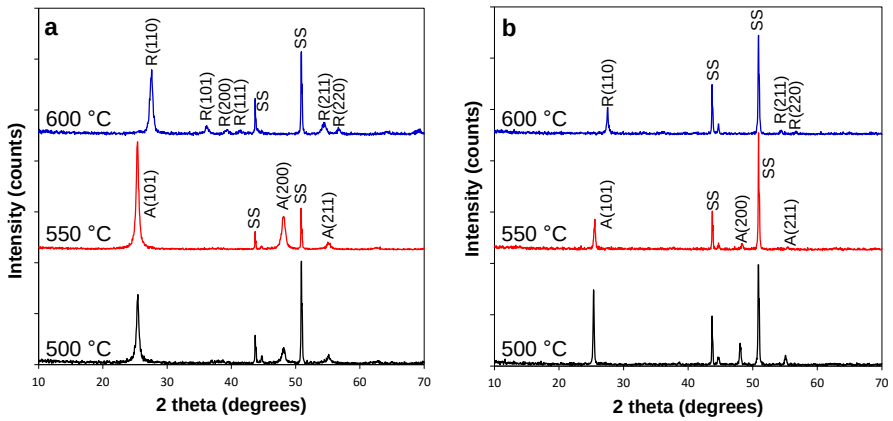

Figure 2.10. XRD patterns of a) B-doped TiO_2 and b) TiO_2 deposited using APCVD at varying temperatures. A = anatase; R = rutile; SS = stainless steel substrate

SEM showed that upon B-doping of the TiO_2 films there was a marked change in the morphology of the particles. The non-doped samples were composed of densely packed, highly faceted particles of typical size around 100 nm, whereas the doped samples were elongated and blade-like, of typical size around 400 nm, Figure 2.11. The crystallite size was estimated from the broadening of the anatase (101) peak and the rutile (110) peak using the Scherrer equation, Equation 1.8. The estimated crystallite sizes are displayed in Table 1 where it was observed that smaller crystallites are obtained when the TiO_2 films were doped with boron, a phenomenon which has been reported previously in powder samples.[50] Interestingly with increasing deposition temperature the crystallite size actually decreased, which may indicate higher rates of nucleation during the CVD process.

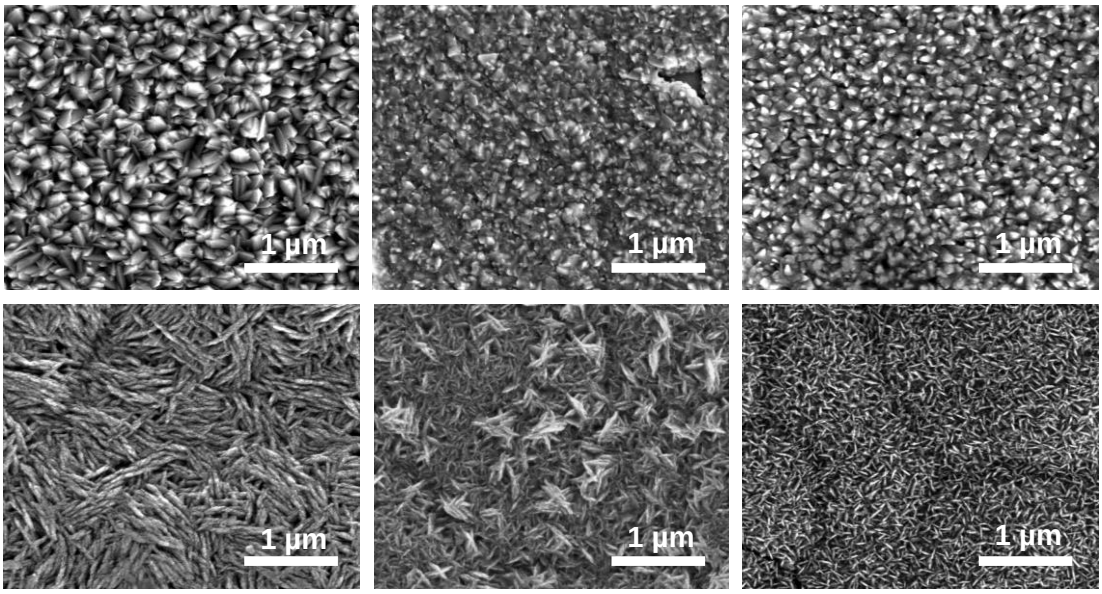

Figure 2.11. SEM images of non-doped (top row) and boron doped (bottom row) TiO_2 CVD samples made at 500, 550 and 600 °C, respectively

Lattice parameters for the B-doped and undoped systems were calculated using the general structure analysis system (GSAS), where the patterns were fit employing a Le Bail model. For fitting ease and accuracy, PXRD patterns were obtained of films on the underlying glass substrates so no contributions from the steel substrates were present. For the anatase films deposited at 500 and 550 °C the lattice parameter along the c-axis decreased by 0.02 and 0.137 Å respectively on boron doping and 0.03 and 0.04 Å as compared to reference values for anatase (44882-ICSD). Lattice parameters were not

calculated for the films deposited at 600 °C as the films on glass were found to be anatase, a directing effect which has been observed previously.[1]

The orientation of crystallites in TiO_2 is known to affect the material's properties, such as wettability,[74] as well as photocatalytic activity.[26, 29, 75] The crystallite orientations of the B-doped and undoped TiO_2 films were semi-quantitatively evaluated by calculating the texture coefficient through comparison of the relative peak intensities with anatase and rutile powder diffraction standards (anatase: 44882-ICSD, rutile: 44881-ICSD) using Equation 1.9. Those reflections in which enhanced or suppressed orientation were identified are outlined in Table 2.1. It was observed that for anatase phase TiO_2 in both doped and non-doped samples the most intense reflection was the (101) plane which is known to be the most thermodynamically stable and prevalent in nanocrystalline TiO_2,[77] and that the degree of orientation in the (101) plane was greater in the boron doped samples. Interestingly, growth in the remaining crystal planes was supressed in all samples with the exception of the boron doped samples, where the (200) plane had a 50% increased orientation when the film was deposited at 550 °C. The average surface energies of the different crystal faces in anatase have been shown to follow the order: {110} at 1.09 $J.m^{-2}$ >{001} at 0.9 $J.m^{-2}$ >{100} at 0.53 $J.m^{-2}$ >{101} at 0.44 $J.m^{-2}$.[78, 79] It is usually believed that high surface energy facets with a higher percentage of under-coordinated atoms are more reactive in heterogeneous reactions, thus the growth of {100} and {001} facets which have 100% under-coordinated Ti_{SC} atoms is highly desirable.[80]

In the rutile sample increased orientation in the (110) plane was observed in the doped and undoped samples but this was greater with the boron dopant present. In the undoped rutile sample, all other crystal faces were supressed whereas in the doped sample the (200), (211) and (220) all had increased texturing. For rutile, the {110} has been shown to be the most active reduction site for catalysis and so this is likely to enhance the material's catalytic ability.[81]

Sample	Reflection TC (hkl)							Crystallite size (nm)	Lattice parameter (Å)	
	A(101)	A(200)	A(211)	R(110)	R(200)	R(211)	R(220)		a-axis	c-axis
TiO_2 500 °C	1.1	0.9	-	-	-	-	-	66	3.7867(3)	9.5068(57)
TiO_2 550 °C	1.1	0.6	-	-	-	-	-	31	3.7820(3)	9.61002(52)

TiO_2 600 °C	-	-	-	1.7	-	0.3	4.8	51	-	-
B-TiO_2 500 °C	1.4	1.0	0.4	-	-	-	-	20	3.7871(4)	9.48438(69)
B-TiO_2 550 °C	1.4	1.5	0.4	-	-	-	-	18	3.7826(24)	9.473(12)
B-TiO_2 600 °C	-	-	-	2.7	1.8	1.2	1.3	14	-	-

Table 2.1. Texture coefficients, crystallite size and lattice parameters derived from XRD data relative to standard powder diffraction patterns of anatase and rutile TiO_2. Deviations in texture coefficient above or below 1 indicate texturing.

Raman spectroscopy was employed to gain further information about chemical environment and microstructure of the thin films as it is very sensitive to local crystallinity. The characteristic Raman peaks of anatase TiO_2 lie at 144, 396, 516 and 639 cm^{-1} and can be assigned to the E_g, B_{1g}, A_{1g} or B_{1g}, and E_g modes, respectively.[82] The main rutile peaks lie at 144, 447 and 609 cm^{-1} and can be assigned to the B_{1g}, A_{1g} and E_g modes, respectively. In rutile a peak also is present at ~232 cm^{-1} and is caused by a multi-phonon scattering process.[83]

The Raman spectra showed a phase transformation from anatase at lower deposition temperature, (500 and 550 °C) to rutile at higher temperatures (600 °C), agreeing with the XRD data, Figure 2.12. Crucially in the doped samples, a shift in the anatase E_g band is observable, from 148.0 cm^{-1} in undoped TiO_2 to 150.1 and 151.9 cm^{-1} for B-doped anatase samples deposited at 500 and 550 °C respectively. A blue shift in the anatase E_g peak has been attributed to phonon confinement which is reported to occur is through a reduction in particle size.[84, 85] This blue shift is consistent with the results presented here as a decrease in particle size is observed on B-doping, (Table 2.1).

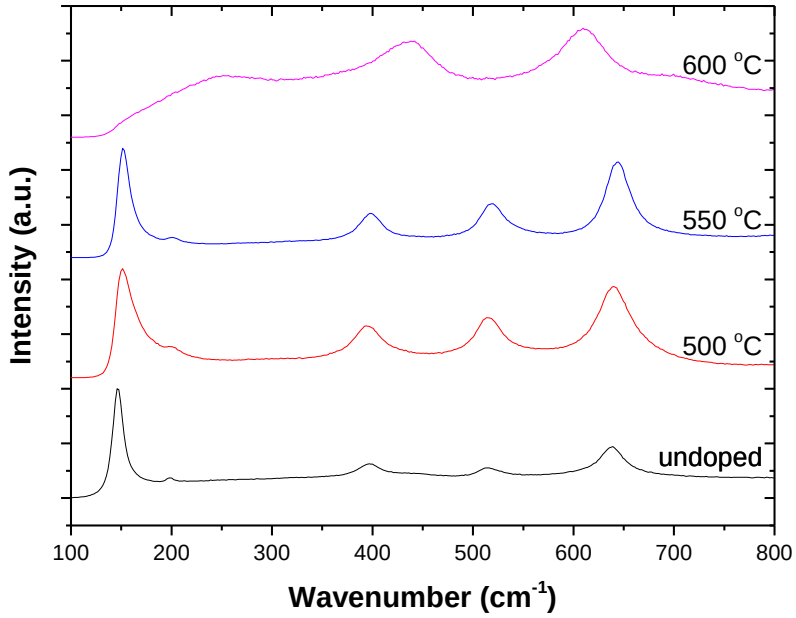

Figure 2.12 Raman spectra of undoped TiO_2 deposited at 500 °C on 304 stainless steel and B-TiO_2 at deposited at varying temperatures on stainless steel

The samples were analysed using XPS to determine the boron content as well as the chemical environment of the doped species. The characteristic peaks of cationic B in B_2O_3 and anionic B in TiB_2 lie at 193.1 and 187.5 eV respectively.[65, 66] Typically intermediate values are observed for B-TiO_2. Generally peaks at ~190.5-191.8 eV have been attributed to boron in an oxygen substitutional position,[55, 56, 86, 87] and peaks at higher binding energy to interstitial boron.[67, 86]

XPS was carried out on ten different B-doped CVD samples and it was found that the Ti peak was located at an average chemical shift of 459.2 ± 0.1 eV, Figure 2.13, indicative of Ti^{4+} with no reduced Ti^{3+} species.[88] The O 1s peak was located at 530.4 ± 0.2 eV. The B 1s peak was observed at an average chemical shift of 191.4 ± 0.2 eV, which combined with the contraction in the c-axis of the unit cell observed from the PXRD data (Table 2.1) is likely attributable to boron in substitutional position.[56] The position of the peak did not vary with phase (anatase vs. rutile) and the average dopant level was found to be 0.9 ± 0.3 at%, Figure 2.13.

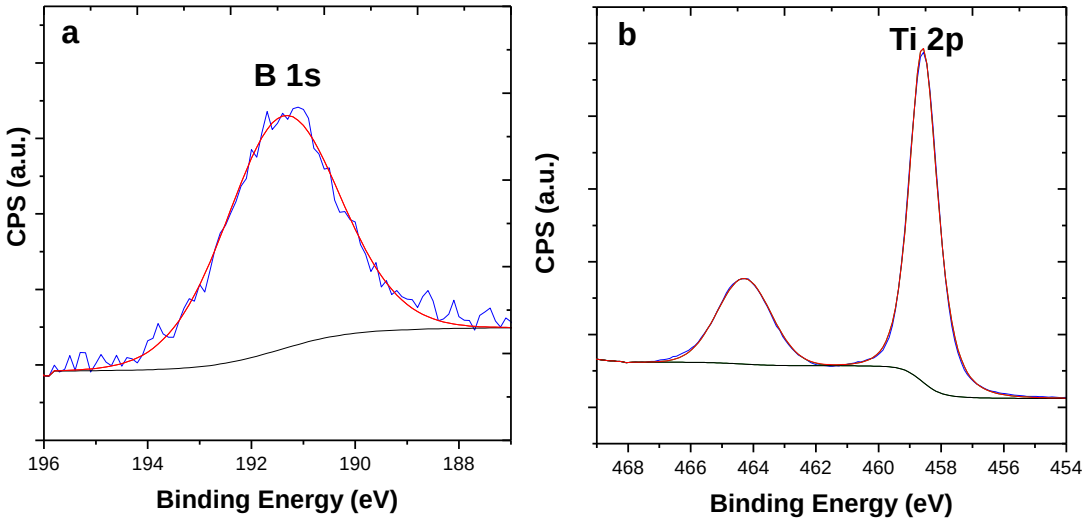

Figure 2.13 XPS spectra of B-doped TiO_2 deposited at 550 °C showing a) the B1s peak and b) the Ti 2p peaks

Despite the relatively low concentration of B doped into the TiO_2 lattice, increasing the flow rate of the $B(O^iPr)_3$ precursor was not attempted in order to increase the ratio of B in the material. This was due to the observation of a cloudy film developing on the surface of the B-TiO_2 which was identified as boric acid by Raman spectroscopy (RRUFF ID R060496), indicating that with this particular precursor the solubility limit of B has been reached. The boric acid was removed by simply rinsing the film with distilled water.

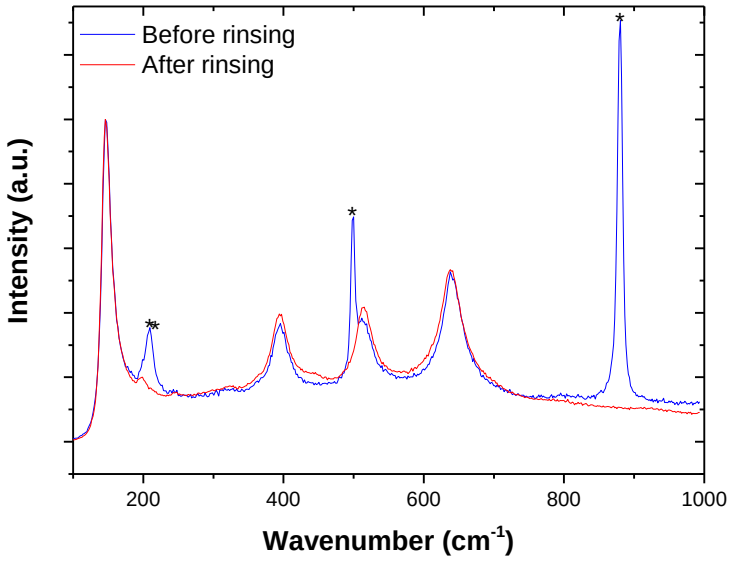

Figure 2.14 Raman spectrum of B-TiO_2 deposited at 550 °C taken before and after rinsing with distilled water showing the removal of boric acid, whose peaks are marked with an asterisk

The optical characteristics of non-doped and B-doped films deposited on glass were determined using UV-vis spectrometry, Figure 2.15. The visible light absorption of the boron-doped samples was enhanced as compared to non-doped TiO_2. Tauc plots were used to determine the band gap of the materials. A band gap of 3.26 eV was calculated for the undoped TiO_2 sample, characteristic of TiO_2 in the anatase phase,[29] which decreased to 3.15 eV on boron doping, similar to other B-TiO_2 systems in the literature.[89]

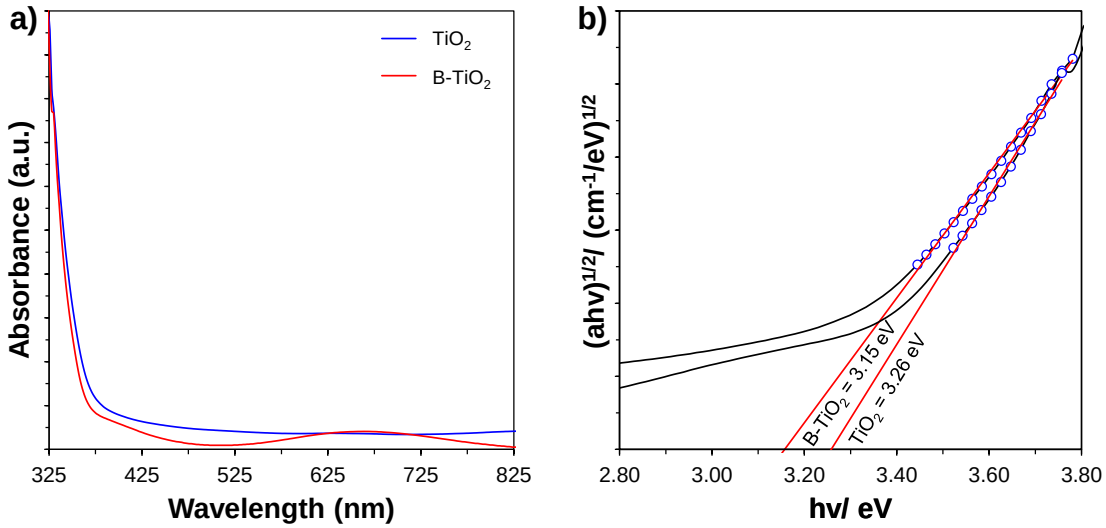

Figure 2.15 a) UV-vis absorption spectra for TiO_2 and B-doped TiO_2 and b) corresponding Tauc plots

2.3.1.2 Photocatalytic water reduction and oxidation

The ability of the films to reduce water to hydrogen was tested using a sacrificial solution of acidified 1:1 water: ethanol. The use of sacrificial solutions (in this case an electron donor) is common in assessing whether one half of the water splitting reaction satisfies the kinetic and thermodynamic potentials for H_2 and O_2 evolution, but it does not necessarily mean the photocatalyst will be capable of overall water splitting. Sacrificial reagents are most frequently chosen to provide an oxidation pathway of lower, or even negative ΔG than for true water splitting, so the process is more thermodynamically favourable.[90] In the case of ethanol oxidation and water reduction, the overall reaction can be written as:

$$C_2H_5OH + 3H_2O \rightarrow 2CO_2 + 6H_2 \quad (2.3)$$

Samples of thickness ~200 nm were selected for testing, as this has been demonstrated to be an optimum thickness for water reduction using a TiO_2 photodiode.[1] Four samples from each deposition temperature were tested using 365 nm UV irradiation, (irradiance = 2 $mW.cm^{-2}$). The gas produced was analysed using gas chromatography and in all samples, a steady rate of hydrogen production was observed, Figure 2.16. The sample with the highest hydrogen production rate was tested again for 4 hours and a similar rate of hydrogen production was observed with no decay, indicating the films are stable during use. No H_2 production was observed when the samples were held in the dark, indicating that the reaction was a photocatalytic and not a chemical one.

Generally samples deposited at 550 °C showed higher hydrogen production rates and B-doped samples far outperformed their undoped counterparts, with activities an order of magnitude higher. The best performing B-doped sample gave a hydrogen production rate of 24 $\mu L.cm^{-2}.hr^{-1}$, as compared to the best non doped sample which gave a rate of 2.6 $\mu L.cm^{-2}.hr^{-1}$. The hydrogen production rate of the B-doped samples also surpassed similar systems in the literature, where an undoped TiO_2 photodiode gave hydrogen production rates of 3 $\mu L.cm^{-2}.hr^{-1}$, and rates of 7 $\mu L.cm^{-2}.hr^{-1}$ were observed for a Pt- loaded TiO_2 thin film.[2, 9] It is likely that the enhancement in rate is due not only to the presence of the boron dopant and the corresponding decrease in the material's band gap, Figure 2.15 but also due to the enhanced orientation along the (200) face observed in the samples deposited at 550 °C, which saw a 50% increase as compared to powder diffraction standards, Table 2.1. The {100} plane is a high energy face in anatase and its abundance has been shown to increase the rate of photocatalysis.[91, 92] If the enhancement in rate were due the presence of B alone, higher rates would be expected from samples deposited at 500 °C, which are also anatase containing a similar %B content, but average orientation on the (200) face.

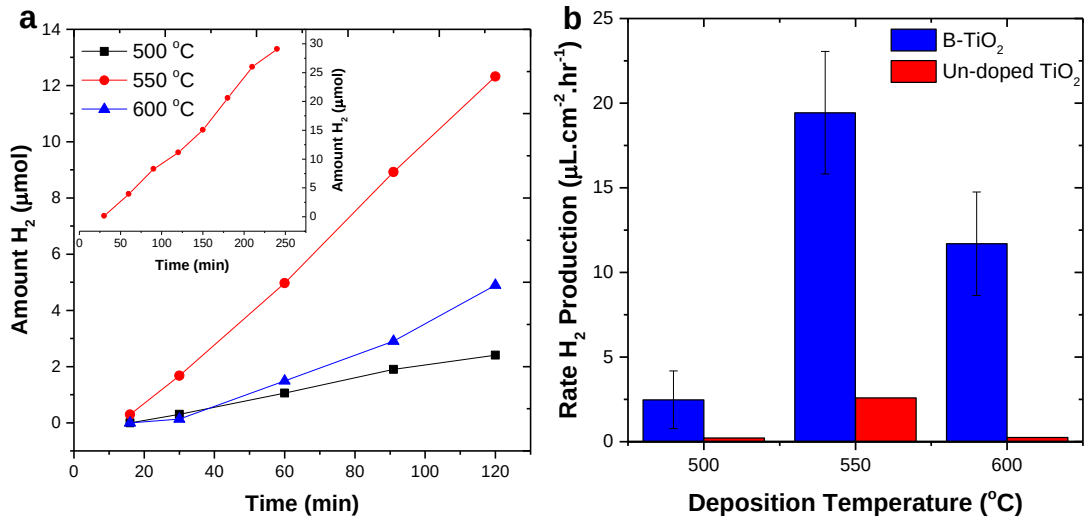

Figure 2.16 Photocatalytic production of hydrogen by boron doped and un-doped samples; a) moles of hydrogen in the headspace with time of B-TiO_2 deposited at varying temperature, inset B-TiO_2 sample deposited at 550 °C re-tested for 4 hours and b) average hydrogen production rates of doped and non-doped samples

Light harvesting was enhanced by the B-dopant as can be seen in Figure 2.15 so the visible light activity of the samples was assessed by irradiation in sacrificial solution with light $\lambda > 400$ nm for 4 h, but no hydrogen was detected. As a result it is thought that the use of a co-dopant such as nitrogen may be necessary to facilitate visible light photocatalysis, as observed by other authors.[93]

The best performing boron doped samples were tested for their water oxidation capabilities in a basic sacrificial solution of $Na_2S_2O_8$. For sacrificial water oxidation using persulfate ions the overall reaction can be written as follows:[94]

$$2S_2O_8^{2-} + 2H_2O \rightarrow 4SO_4^{2-} + 4H^+ + O_2 \qquad (2.4)$$

With the half reactions:

$$2S_2O_8^{2-} + 4e^- \rightleftharpoons 4SO_4^{2-} \qquad E^0_{ox} = +1.960 \text{ V vs NHE}^{94} \qquad (2.5)$$

$$2H_2O + 4h^+ \rightleftharpoons 4H^+ + O_2 \qquad E^0_{red} = -1.229 \text{ V vs NHE} \qquad (2.6)$$

The use of the persulfate ion leads to a large and negative ΔG, (-355 kJ/mol at pH = 13),[94] for reaction 2.9 and is a highly irreversible process.

The samples were loaded into the vessel which was then sealed and left for a period of time before the light was turned on and there were no leaks present, Figure 2.17. Samples were then irradiated using UVA illumination of irradiance 15 mW.cm^{-2}. The sample deposited at 500 °C was inactive for oxygen production and the samples deposited at 550 and 600 °C gave oxygen evolution rates of 6.6 and 22.0 μL.cm^{-2}.hr^{-1} respectively. Interestingly the rutile sample deposited at 600 °C performed better than the anatase sample deposited at 550 °C in the water oxidation test, but worse in the water reduction test. The relative poor performance of the anatase samples for water oxidation could be accounted for by the suppression of the {001} face, which has been shown to be the anatase oxidation site.[81] In order to improve the activity of the anatase samples for water photooxidation a co-catalyst could be used.[95, 96]

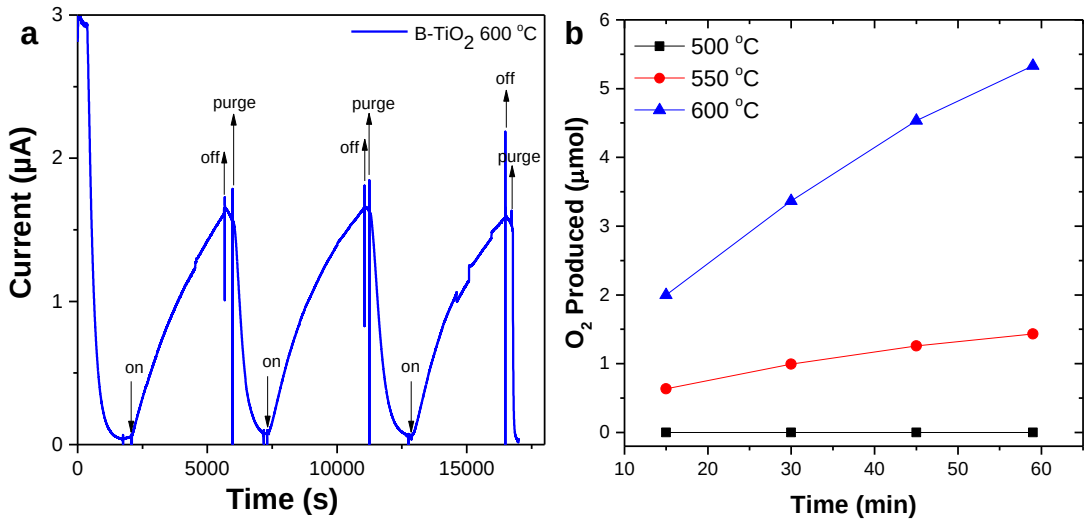

Figure 2.17 Oxygen evolution from B-TiO_2 samples deposited at various temperatures measured using a Clark cell, a) trace of current measured vs time for B-TiO_2 600 indicating when the light was turned on and off and the system purged with N_2 and b) oxygen production for a single cycle of the test, which was repeated 3 times in all cases.

UV light sources of different irradiances were used for the hydrogen and oxygen evolution tests (2 and 15 mW.cm^{-2} respectively) and so in order to compare the results apparent quantum yields were calculated using the formula[34]:

$$\text{AQY}(\%) = \frac{\text{number of reacted electrons or holes}}{\text{number of incident photons}} \text{ x } 100 \qquad (2.7)$$

The B-TiO_2 sample deposited at 550 °C gave better hydrogen production but the sample deposited at 600 °C gave stoichiometric AQYs of hydrogen and oxygen (Table 2.2).

Sample	AQY Hydrogen Production (%)	AQY Oxygen Production (%)
B-TiO_2 500	1.0	0.0
B-TiO_2 550	8.1	0.7
B-TiO_2 600	4.9	2.4

Table 2.2. B-TiO_2 apparent quantum yields for hydrogen and oxygen production from measurements in sacrificial solutions of ethanol and sodium persulfate respectively

The photocurrent density as a function of applied voltage produced by the samples deposited on FTO was assessed using filters to simulate the sun's UV content and is presented in Figure 2.18. The light was chopped during the positive sweep and held in the dark on the negative sweep. The dark current observed was negligible indicating the samples are stable. The B-TiO_2 samples showed a 500 mV smaller overpotential against water photo-oxdiation (more rapid onset of current) than the non-doped samples and a steep profile before reaching a plateau which is typical of an efficient photodiode,[97, 98] whereas the non-doped samples did not reach a stable photocurrent. This improvement of the photocurrent density with boron doping has also been observed by Lu and co-workers, who fabricated B-TiO_2 hollow nanotubes via anodisation: here the enhanced performance was attributed to increased light absorption.[53] The morphology of the crystallites has also been shown to effect the photoconversion efficiency,[99-101] and so the change in the microstructure of the boron-doped material could also explain the improved photocurrent profile. The earlier onset of photocurrent supports the superior activity of the B-doped samples in the hydrogen testing experiments; despite the samples having the same saturation current, the non-doped samples would require further biasing to see the same activity as the B-doped samples.

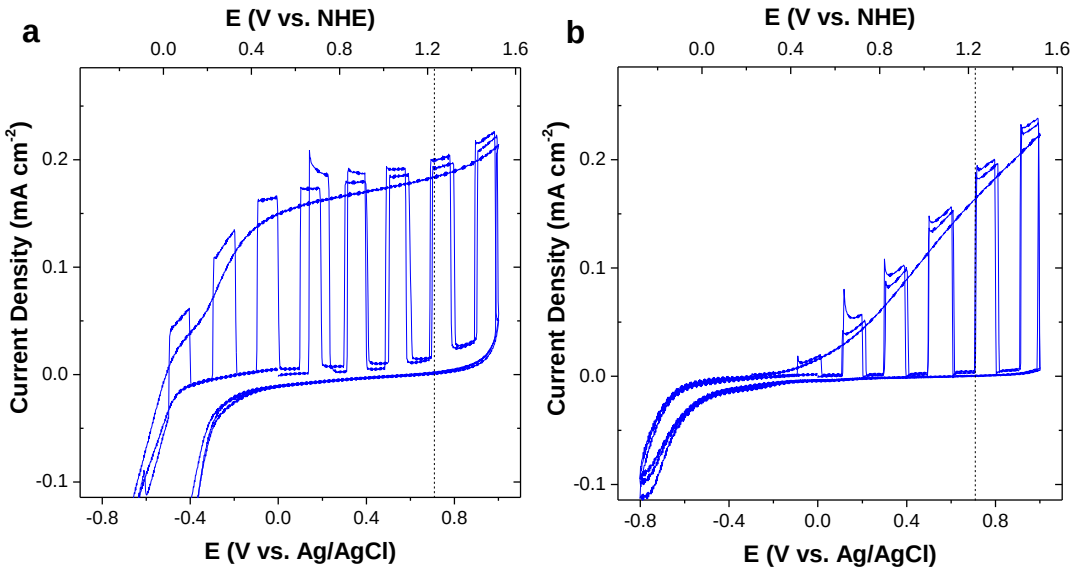

Figure 2.18 Photocurrent density of a) B-TiO_2 and b) undoped TiO_2 (both deposited at 550 °C) in 0.1 M KNO_3 under simulated solar UV irradiation (10 $mW.cm^{-2}$)

2.3.2 B,N-TiO_2

2.3.2.1 Structural Characterisation

After optimising the film deposition conditions for B-TiO_2, (flow rate of 0.6 L/ min for $TiCl_4$, EtOAc and $B(iOPr)_3$ at 550 °C for 40 s), t-butylamine (t-$BuNH_2$), a nitrogen dopant source, was added as an additional precursor to facilitate B,N-co-doping. Three flow rates were selected for the t-$BuNH_2$ and all other flow rates were held constant at 0.6 L/min in order to investigate the effect of the N-doping percentage. The flow rates used for depositions are summarised in Table 2.3 and depositions were carried out at 550 °C.

	Ratio Reactants			
Flow rate $tBuNH_2$ (L/min)	**$TiCl_4$**	**EtOAc**	**$tBuNH_2$**	**$B(iOPr)_3$**
0.2	1	2.1	0.53	0.99
0.1	1	2.1	0.26	0.99
0.05	1	2.1	0.13	0.99

Table 2.3 Flow rates of t-$BuNH_2$ (where all other precursors had a flow rate of 0.6 L/min) and ratio of reactants for B,N-TiO_2 depositions

The films were similar in appearance to the B-only doped TiO_2 films and no cracks or delamination on application of the Scotch tape test were apparent. XRD revealed that the films were anatase phase, Figure 2.19, however due to the thinness of the films and slight warping of the substrates (a guillotine was used to cut the steel), XRD patterns were too poor to carry out further data analysis, such as deriving the texture coefficients as was carried out with the B only doped films.

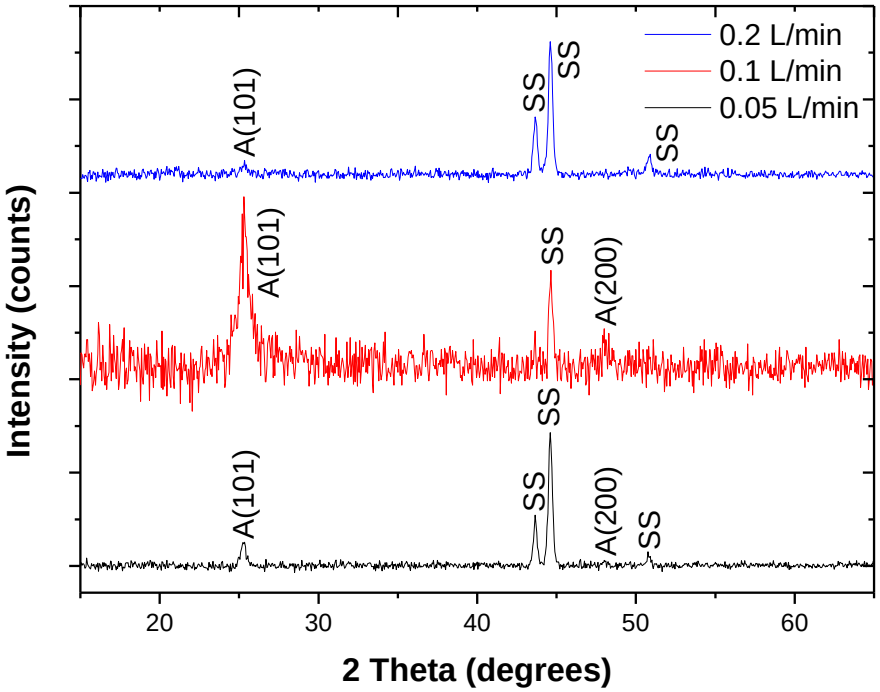

Figure 2.19 XRD patterns of B,N-doped TiO_2 films deposited using APCVD of $TiCl_4$, ethyl acetate, triisopropyl borate and t-butylamine at 550 °C. A = anatase; SS = stainless steel substrate

The presence of anatase phase TiO_2 in all B,N-TiO_2 samples was confirmed by Raman spectroscopy. Hematite (iron oxide) was also observed with peaks at ~ 225.8, 246.5, 291.3, 299.1, 412.8, 508.5, 615.5 and 669.2 cm^{-1},[102, 103] indicating some corrosion of the steel substrate during deposition. Interestingly the anatase E_g peaks in the B,N-TiO_2 samples were not blue-shifted relative to pristine TiO_2, (where E_g = 148.0 cm^{-1}), with the E_g peaks located at 144.5, 146.1 and 145.8 cm^{-1} for the samples with a flow rate of 0.05, 0.1 and 0.2 L/min respectively.

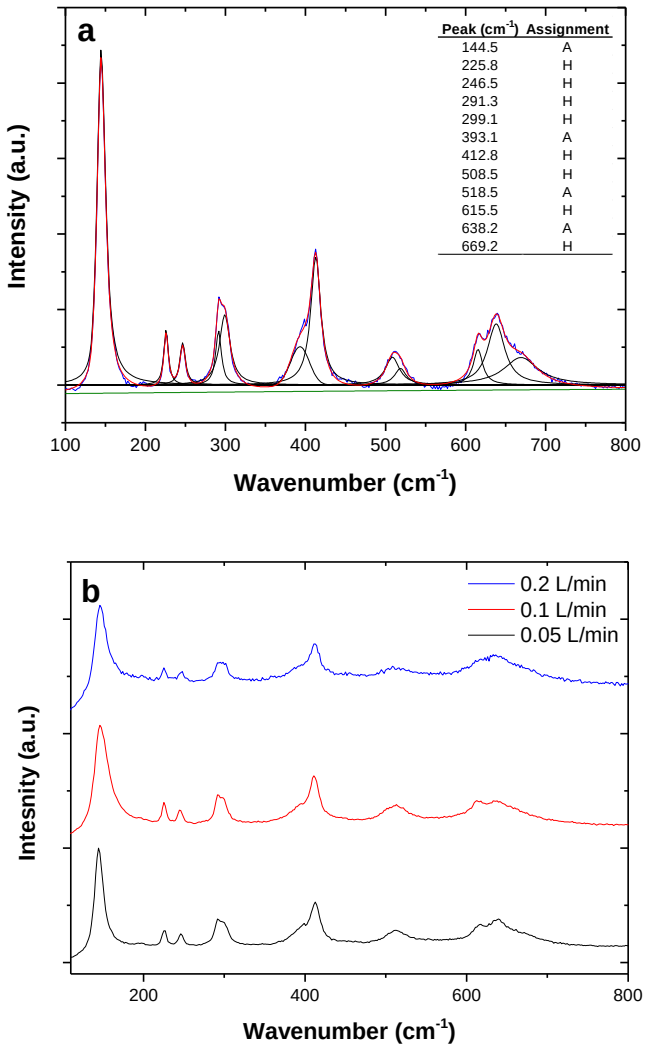

Figure 2.20. Raman spectra of B,N-TiO_2; a) peak fitting and assignments of B,N-TiO_2 deposited on steel using CVD with a flow rate of 0.05 L/min t-$BuNH_2$ where A =anatase and H = hematite, where peaks were modelled using a Gaussian-Lorentzian function and b) Raman spectra of B,N-TiO_2 deposited on steel using CVD with varying flow rates of t-$BuNH_2$

SEM of the samples revealed a similar morphology of crystallite to the B-doped TiO_2 with elongated crystallites, however these appeared in small islands indicating that the nitrogen co-dopant causes a reduction in the crystallinity of the films, which is reflected in the poor XRD patterns.

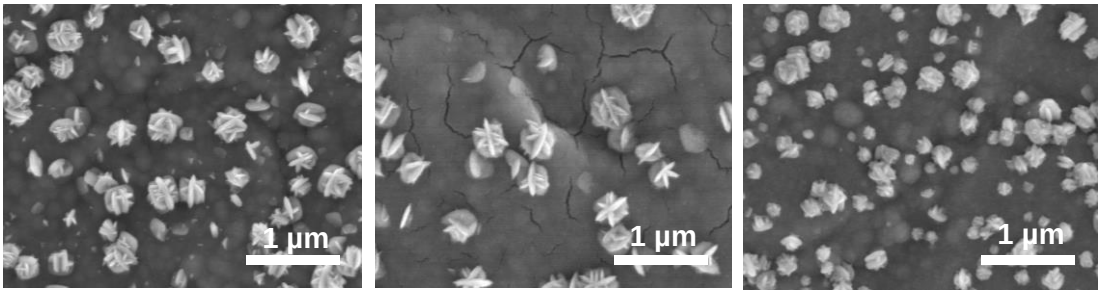

Figure 2.21 SEM images of B,N-TiO_2 with a flow rate of 0.05, 0.1 and 0.2 L/min left to right

XPS analysis revealed that in all B,N- co-doped samples nitrogen had been doped into the lattice in an interstitial position, displaying the characteristic binding energy of N(0) at ~400 eV.[104, 105] This binding energy has also been attributed to chemisorbed γ-N_2,[106] however due to the absence of any N 1s peak in the B-only doped XPS spectra it can be concluded that the peak at 400 eV is indeed due to N incorporated into the TiO_2 lattice. A slight shift was observed in the binding energy of the B 1s peak from ~191.4 eV in B-only doped TiO_2 to ~191.7 eV in B,N-TiO_2 which has been observed previously, where the authors attributed this shift to the proximity of the B and N atoms.[93] Interestingly, as the concentration of N in the samples increases the concentration of B is also observed to increase, Table 2.4. This is explained by the interstitially doped N creating oxygen vacancies which can be filled by the B in an oxygen substitutional position. This phenomenon has also been observed with interstitially doped B, which increased the solubility of substitutionally doped N.[69]

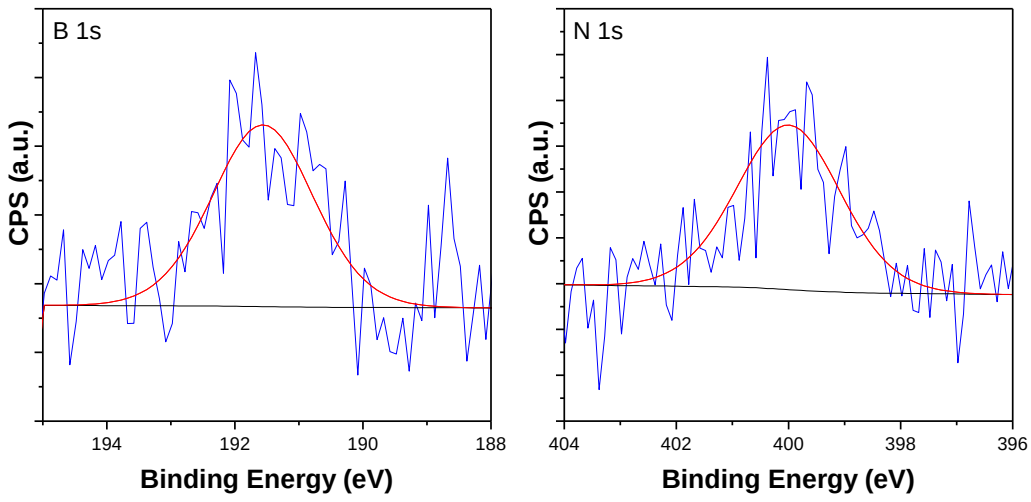

Figure 2.22 Compositional analysis of B,N-TiO_2 films using XPS, showing the B 1s and N1s scans of the sample deposited with a 0.1 L/min flow rate of $tBuNH_2$

$tBuNH_2$ L/min	%N	N Binding Energy (eV)	%B	B Binding Energy (eV)
0.05	0.20	400.1	0.46	191.7
0.1	0.31	400.1	0.64	191.7
0.2	0.36	400.0	0.90	191.9

Table 2.4 Dopant concentration determined using XPS of B,N-TiO_2 with varying flow rates of $tBuNH_2$

The optical characteristics of the B,N co-doped films deposited on glass were determined using UV-vis spectrometry, Figure 2.23. Interestingly, a blue-shift in the absorption as compared to undoped TiO_2 was observed for the B,N co-doped films. A band gap of 3.26 eV was calculated for the undoped TiO_2 sample, characteristic of TiO_2 in the anatase phase,[29] Figure 2.15. This increased to 3.33 eV for the B,N-codoped film deposited using a flow rate of 0.05 L/min t-$BuNH_2$, 3.31 eV for the film deposited using a flow rate of 0.1 L/min t-$BuNH_2$ and 3.30 eV for the film deposited using 0.2 L/min t-$BuNH_2$. Since the B-dopant caused a narrowing of the TiO_2 band gap in the B-only system, the steady decrease of the band gap here is likely caused by the increasing amount of B incorporated in the films as it fills the vacancies created by the substitutional N. A blue shift due to the incorporation of N-TiO_2 has been observed previously,[107] however the overwhelming conclusion from the literature is that incorporation of N into the TiO_2 lattice causes a red-shift in the absorption onset,[44] and so the widening of the band gap observed may be caused by other factors such as size effects due to the reduced crystallinity of the films.[108]

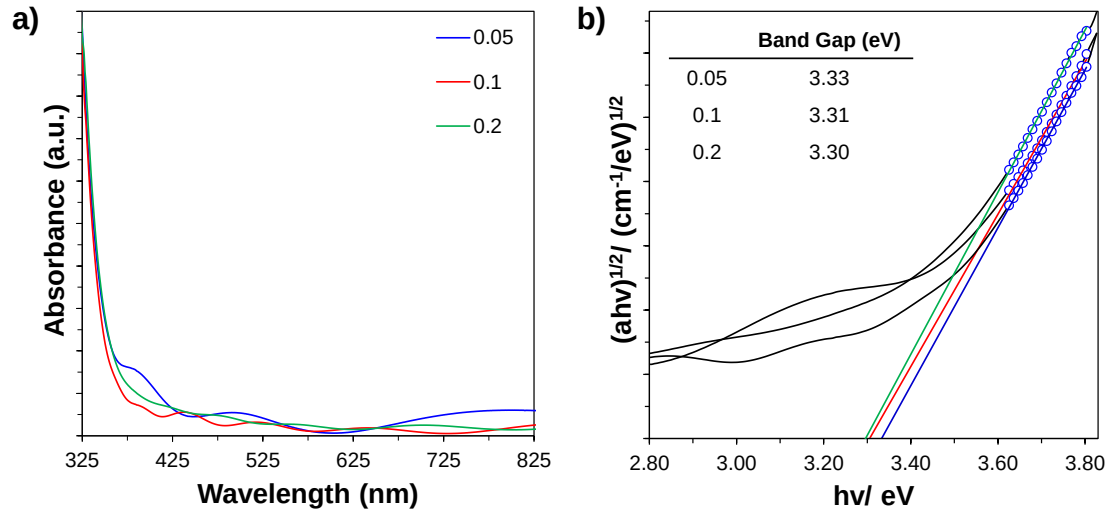

Figure 2.23 a) UV-vis absorption spectra for B,N co-doped TiO_2 and b) corresponding Tauc plots

2.3.2.2 Photocatalytic water reduction and oxidation

The samples were tested for hydrogen production using the same procedure as for the B-only doped samples and it was found that with increasing nitrogen content, there was a decrease in the hydrogen production rate, Figure 2.24. This same trend was observed in the PEC of the samples deposited on FTO, where the photocurrent saturation decreased proportionally to increasing nitrogen content, Figure 2.25. The samples were inactive for oxygen production. This reduction in activity for higher ratios of nitrogen in co-doped TiO_2 has been observed before, however the authors did report an improvement in activity as compared to B-doped only TiO_2.[60] In this case the reduction in activity is likely due to a decrease in coverage and crystallinity of the B,N-doped TiO_2 samples and the increase in the magnitude of the band gap as compared to B-only doped TiO_2.

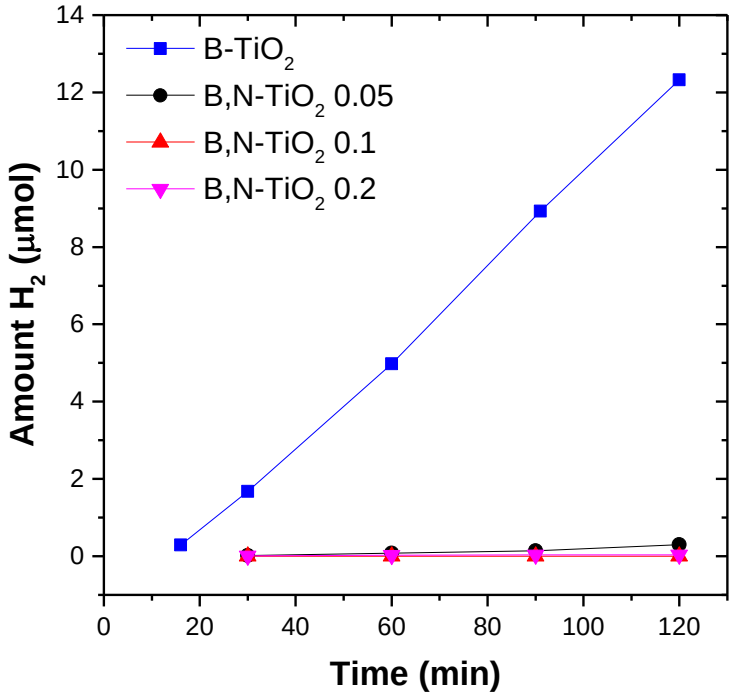

Figure 2.24 Photocatalytic water reduction testing of B,N-TiO_2. Samples were tested in acidified sacrificial solution under 356 nm irradiation

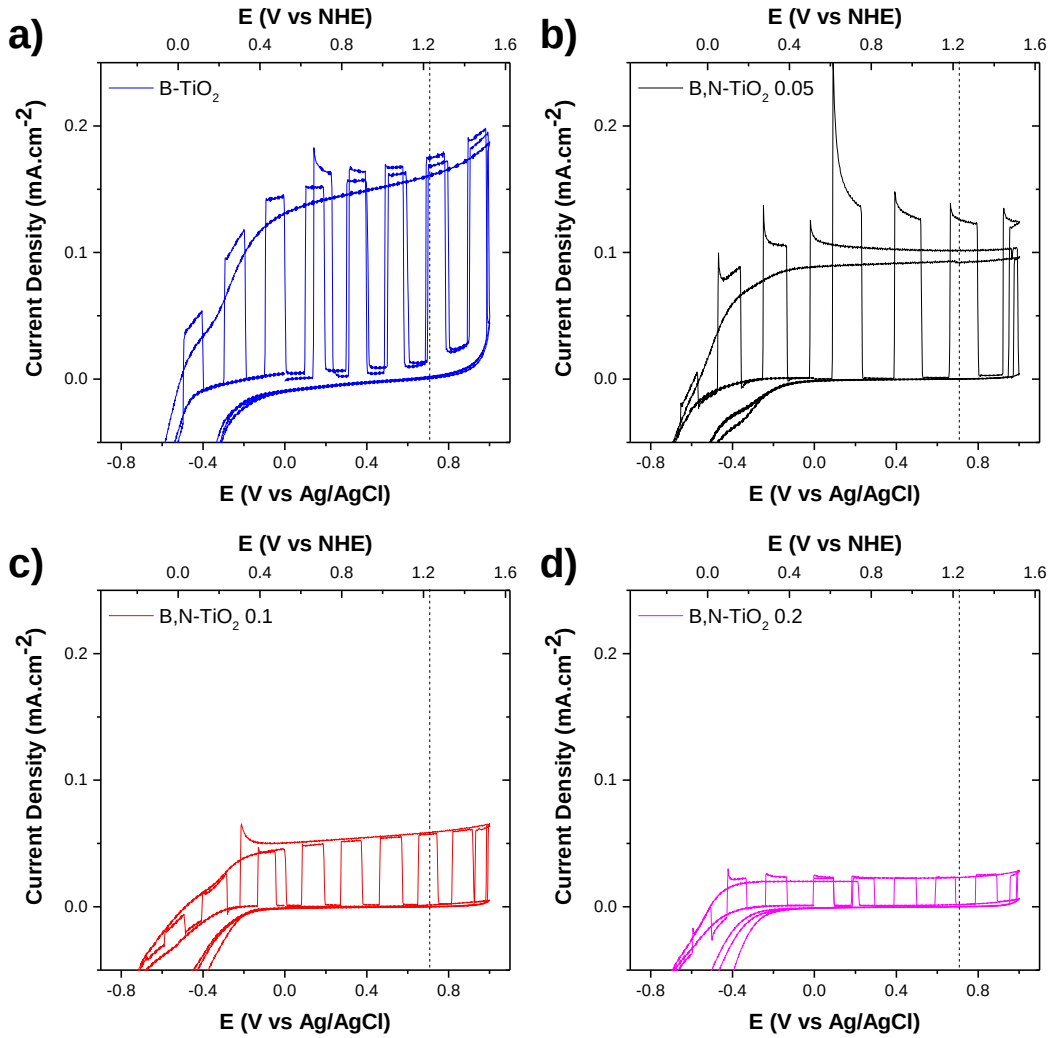

Figure 2.25 PEC of samples tested in 0.1 M KNO_3 under simulated solar UV irradiation (10 $mW.cm^{-2}$)

2.4 Conclusions

Boron doped and boron-nitrogen co-doped TiO_2 films were deposited onto steel and FTO substrates using chemical vapour deposition of titanium(IV) chloride, ethyl acetate, triisopropyl borate and t-butyl amine, which to the authors' knowledge is the first example of thin film B- and B,N- doped TiO_2 made using APCVD. The films were analysed using XRD and Raman spectroscopy and were crystalline TiO_2 with no additional phases present. The samples deposited at lower temperature (500 and 550 °C) were anatase and rutile at higher temperatures (600 °C). Raman spectroscopy revealed a shift in the E_g anatase band for B-doped samples, attributed to the presence of the dopant and decrease in crystallite size as compared to undoped samples. The band gap of the TiO_2 films was observed to decrease on B-doping and increase on B,N-codoping.

The composition of the films was analysed using XPS and coupled with a contraction in the unit cell observed by calculation of lattice parameters of the films, it was thought the B dopant was incorporated into the TiO_2 lattice in an O-substitutional position, and the N was doped in an interstitial position. Remarkable rates of hydrogen production were observed in the B-doped films when compared to non-doped samples as well as having more favourable photocurrent profiles, however the presence of N drastically reduced the rate of hydrogen production. In light of this boron doped TiO_2 APCVD films of low cost could be manufactured on a reel-to-reel process for photodiodes, which could be used for water reduction and oxidation but nitrogen co-doping using a t-butylamine source is not recommended. The improvement in photocatalysis on boron doping could also be utilised in wider applications such as water purification, dye-sensitised solar cells and antimicrobial surfaces.

2.5 References

1. G. Hyett, J. A. Darr, A. Mills and I. P. Parkin, *Chem.-Eur. J.*, 2010, 16, 10546-10552.
2. G. Hyett, J. A. Darr, A. Mills and I. P. Parkin, *Chem. Vapor Depos.*, 2010, 16, 301-304.
3. A. Fujishima and K. Honda, *Nature*, 1972, 238, 37-+.
4. E. Miller, A. DeAngelis and S. Mallory, in *Photoelectrochemical Hydrogen Production*, eds. R. van de Krol and M. Grätzel, Springer US, 2012, vol. 102, ch. 7, pp. 205-273.
5. E. H. Rhoderick, *Solid-State and Electron Devices, IEE Proceedings I*, 1982, 129, 1.
6. K. D. Knowles, Chris; Brook David; Lianne Sallows, Metal–Semiconductor Junction – Rectifying Contact, http://www.doitpoms.ac.uk/tlplib/semiconductors/junction_rectifying.php, Accessed 7th October 2015.
7. M. Kitano, K. Tsujimaru and M. Anpo, *Applied Catalysis a-General*, 2006, 314, 179-183.
8. M. Kitano, K. Tsujimaru and M. Anpo, *Top. Catal.*, 2008, 49, 4-17.
9. M. Kitano, M. Takeuchi, M. Matsuoka, J. A. Thomas and M. Anpo, *Catal. Today*, 2007, 120, 133-138.
10. Y. Horiuchi, T. Toyao, M. Takeuchi, M. Matsuoka and M. Anpo, *Physical Chemistry Chemical Physics*, 2013, 15, 13243-13253.
11. M. Kitano, K. Iyatani, K. Tsujimaru, M. Matsuoka, M. Takeuchi, M. Ueshima, J. M. Thomas and M. Anpo, *Top. Catal.*, 2008, 49, 24-31.
12. J. Freitag and D. W. Bahnemann, *Phys. Status Solidi-Rapid Res. Lett.*, 2014, 8, 596-599.
13. J. Freitag and D. W. Bahnemann, *Chemphyschem*, 2015, 16, 2670-2679.
14. K. Hashimoto, H. Irie and A. Fujishima, *Jpn. J. Appl. Phys. Part 1 - Regul. Pap. Brief Commun. Rev. Pap.*, 2005, 44, 8269-8285.
15. G. C. Boase, in *Oxford Dictionary of National Biography*, eds. H. C. G. Matthew and B. and Harrison, Oxford University Press, 2004.
16. Y. Cui, H. Du and L. S. Wen, *J. Mater. Sci. Technol.*, 2008, 24, 675-689.
17. G. Pfaff and P. Reynders, *Chem. Rev.*, 1999, 99, 1963-1981.
18. J. H. Braun, A. Baidins and R. E. Marganski, *Prog. Org. Coat.*, 1992, 20, 105-138.
19. A. Weir, P. Westerhoff, L. Fabricius, K. Hristovski and N. von Goetz, *Environ. Sci. Technol.*, 2012, 46, 2242-2250.
20. J. Wang, G. Zhou, C. Chen, H. Yu, T. Wang, Y. Ma, G. Jia, Y. Gao, B. Li, J. Sun, Y. Li, F. Jiao, Y. Zhao and Z. Chai, *Toxicology Letters*, 2007, 168, 176-185.
21. A. Salvador, M. C. Pascual-Marti, J. R. Adell, A. Requeni and J. G. March, *J. Pharm. Biomed. Anal.*, 2000, 22, 301-306.
22. E. Keidel, *Furben Zeitung*, 1929, 34, 1242.
23. A. Mills and S. LeHunte, *Journal of Photochemistry and Photobiology a-Chemistry*, 1997, 108, 1-35.
24. U. I. Gaya and A. H. Abdullah, *Journal of Photochemistry and Photobiology C-Photochemistry Reviews*, 2008, 9, 1-12.
25. O. Carp, C. L. Huisman and A. Reller, *Prog. Solid State Chem.*, 2004, 32, 33-177.
26. A. Fujishima, X. T. Zhang and D. A. Tryk, *Surf. Sci. Rep.*, 2008, 63, 515-582.

27. A. Fujishima, T. N. Rao and D. A. Tryk, *Journal of Photochemistry and Photobiology C: Photochemistry Reviews*, 2000, 1, 1-21.
28. R. D. Shannon and J. A. Pask, *Journal of the American Ceramic Society*, 1965, 48, 391-&.
29. U. Diebold, *Surf. Sci. Rep.*, 2003, 48, 53-229.
30. S. Burnside, J. E. Moser, K. Brooks, M. Gratzel and D. Cahen, *J. Phys. Chem. B*, 1999, 103, 9328-9332.
31. O. Khaselev and J. A. Turner, *Science*, 1998, 280, 425-427.
32. M. Ni, M. K. H. Leung, D. Y. C. Leung and K. Sumathy, *Renewable & Sustainable Energy Reviews*, 2007, 11, 401-425.
33. W. Y. Choi, A. Termin and M. R. Hoffmann, *J. Phys. Chem.*, 1994, 98, 13669-13679.
34. A. Kudo and Y. Miseki, *Chem. Soc. Rev.*, 2009, 38, 253-278.
35. R. Niishiro, R. Konta, H. Kato, W. J. Chun, K. Asakura and A. Kudo, *Journal of Physical Chemistry C*, 2007, 111, 17420-17426.
36. M. Anpo, M. Takeuchi, K. Ikeue and S. Dohshi, *Current Opinion in Solid State & Materials Science*, 2002, 6, 381-388.
37. M. Takeuchi, H. Yamashita, M. Matsuoka, M. Anpo, T. Hirao, N. Itoh and N. Iwamoto, *Catalysis Letters*, 2000, 67, 135-137.
38. M. Anpo and M. Takeuchi, *Journal of Catalysis*, 2003, 216, 505-516.
39. R. Asahi, T. Morikawa, T. Ohwaki, K. Aoki and Y. Taga, *Science*, 2001, 293, 269-271.
40. T. Umebayashi, T. Yamaki, H. Itoh and K. Asai, *Appl. Phys. Lett.*, 2002, 81, 454-456.
41. S. U. M. Khan, M. Al-Shahry and W. B. Ingler, *Science*, 2002, 297, 2243-2245.
42. J. C. Yu, J. G. Yu, W. K. Ho, Z. T. Jiang and L. Z. Zhang, *Chem. Mat.*, 2002, 14, 3808-3816.
43. I. E. Grey, C. Li, D. M. MacRae and L. A. Bursill, *Journal of Solid State Chemistry*, 1996, 127, 240-247.
44. R. Asahi, T. Morikawa, H. Irie and T. Ohwaki, *Chem. Rev.*, 2014, 114, 9824-9852.
45. S. Livraghi, K. Elghniji, A. M. Czoska, M. C. Paganini, E. Giamello and M. Ksibi, *Journal of Photochemistry and Photobiology a-Chemistry*, 2009, 205, 93-97.
46. S. Mahalingam and M. J. Edirisinghe, *J. Phys. D-Appl. Phys.*, 2008, 41, 9.
47. K. Pomoni, A. Vomvas and C. Trapalis, *J. Non-Cryst. Solids*, 2008, 354, 4448-4457.
48. H. Irie, Y. Watanabe and K. Hashimoto, *J. Phys. Chem. B*, 2003, 107, 5483-5486.
49. L. Zhao, Q. Jiang and J. S. Lian, *Appl. Surf. Sci.*, 2008, 254, 4620-4625.
50. D. Chen, D. Yang, Q. Wang and Z. Y. Jiang, *Industrial & Engineering Chemistry Research*, 2006, 45, 4110-4116.
51. S. C. Moon, H. Mametsuka, S. Tabata and E. Suzuki, *Catal. Today*, 2000, 58, 125-132.
52. S. C. Moon, H. Mametsuka, E. Suzuki and Y. Nakahara, *Catal. Today*, 1998, 45, 79-84.
53. N. Lu, X. Quan, J. Y. Li, S. Chen, H. T. Yu and G. H. Chen, *Journal of Physical Chemistry C*, 2007, 111, 11836-11842.
54. Y. L. Su, X. W. Zhang, S. Han, X. Q. Chen and L. C. Lei, *Electrochem. Commun.*, 2007, 9, 2291-2298.

55. S. In, A. Orlov, R. Berg, F. Garcia, S. Pedrosa-Jimenez, M. S. Tikhov, D. S. Wright and R. M. Lambert, *Journal of the American Chemical Society*, 2007, 129, 13790-+.
56. W. Zhao, W. H. Ma, C. C. Chen, J. C. Zhao and Z. G. Shuai, *Journal of the American Chemical Society*, 2004, 126, 4782-4783.
57. I. A. Md, S. S. Bhattacharya and H. Hahn, *J. Appl. Phys.*, 2009, 105, 8.
58. A. Zaleska, J. W. Sobczak, E. Grabowska and J. Hupka, *Applied Catalysis B-Environmental*, 2008, 78, 92-100.
59. Y. Huang, W. K. Ho, Z. H. Ai, X. A. Song, L. Z. Zhang and S. C. Lee, *Applied Catalysis B-Environmental*, 2009, 89, 398-405.
60. V. Gombac, L. De Rogatis, A. Gasparotto, G. Vicario, T. Montini, D. Barreca, G. Balducci, P. Fornasiero, E. Tondello and M. Graziani, *Chemical Physics*, 2007, 339, 111-123.
61. H. Geng, S. W. Yin, X. Yang, Z. G. Shuai and B. G. Liu, *J. Phys.-Condes. Matter*, 2006, 18, 87-96.
62. E. Finazzi, C. Di Valentin and G. Pacchioni, *Journal of Physical Chemistry C*, 2009, 113, 220-228.
63. L. Chen, T. Goto, T. Hirai and T. Amano, *J. Mater. Sci. Lett.*, 1990, 9, 997-999.
64. A. R. Burke, C. R. Brown, W. C. Bowling, J. E. Glaub, D. Kapsch, C. M. Love, R. B. Whitaker and W. E. Moddeman, *Surface and Interface Analysis*, 1988, 11, 353-358.
65. J. A. Schreifels, P. C. Maybury and W. E. Swartz, *Journal of Catalysis*, 1980, 65, 195-206.
66. G. Mavel, J. Escard, P. Costa and J. Castaing, *Surface Science*, 1973, 35, 109-116.
67. Y. M. Wu, M. Y. Xing and J. L. Zhang, *Journal of Hazardous Materials*, 2011, 192, 368-373.
68. Y. Cong, F. Chen, J. L. Zhang and M. Anpo, *Chemistry Letters*, 2006, 35, 800-801.
69. G. Liu, L. C. Yin, J. Q. Wang, P. Niu, C. Zhen, Y. P. Xie and H. M. Cheng, *Energy Environ. Sci.*, 2012, 5, 9603-9610.
70. Y. X. Li, G. F. Ma, S. Q. Peng, G. X. Lu and S. B. Li, *Appl. Surf. Sci.*, 2008, 254, 6831-6836.
71. A. J. Cross, C. W. Dunnill and I. P. Parkin, *Chem. Vapor Depos.*, 2012, 18, 133-139.
72. A. L. Patterson, *Phys. Rev.*, 1939, 56, 978-982.
73. J. I. Langford and A. J. C. Wilson, *J. Appl. Crystallogr.*, 1978, 11, 102-113.
74. X. J. Feng, J. Zhai and L. Jiang, *Angew. Chem.-Int. Edit.*, 2005, 44, 5115-5118.
75. G. Liu, J. C. Yu, G. Q. Lu and H. M. Cheng, *Chem. Commun.*, 2011, 47, 6763-6783.
76. C. Barret and T. B. Massalski, *Structure of Metals*, Pergamon, 1980.
77. V. Shklover, M. K. Nazeeruddin, S. M. Zakeeruddin, C. Barbe, A. Kay, T. Haibach, W. Steurer, R. Hermann, H. U. Nissen and M. Gratzel, *Chem. Mat.*, 1997, 9.
78. M. Lazzeri, A. Vittadini and A. Selloni, *Physical Review B*, 2001, 63.
79. M. Lazzeri, A. Vittadini and A. Selloni, *Physical Review B*, 2002, 65, 1.
80. F. Pan, K. Wu, H. X. Li, G. Q. Xu and W. Chen, *Chem.-Eur. J.*, 2014, 20, 15095-15101.
81. T. Ohno, K. Sarukawa and M. Matsumura, *New Journal of Chemistry*, 2002, 26, 1167-1170.

82. W. F. Zhang, Y. L. He, M. S. Zhang, Z. Yin and Q. Chen, *J. Phys. D-Appl. Phys.*, 2000, 33, 912-916.
83. T. Ohsaka, F. Izumi and Y. Fujiki, *Journal of Raman Spectroscopy*, 1978, 7, 321-324.
84. Z. Zhang, S. Brown, J. B. M. Goodall, X. Weng, K. Thompson, K. Gong, S. Kellici, R. J. H. Clark, J. R. G. Evans and J. A. Darr, *J. Alloy. Compd.*, 2009, 476.
85. A. S. Pottier, S. Cassaignon, C. Chaneac, F. Villain, E. Tronc and J. P. Jolivet, *Journal of Materials Chemistry*, 2003, 13, 877-882.
86. X. Ding, X. Song, P. Li, Z. Ai and L. Zhang, *Journal of Hazardous Materials*, 2011, 190, 604-612.
87. N. O. Gopal, H. H. Lo and S. C. Ke, *Journal of the American Chemical Society*, 2008, 130, 2760-+.
88. M. Murata, K. Wakino and S. Ikeda, *J. Electron Spectrosc. Relat. Phenom.*, 1975, 6, 459-464.
89. V. Stengl, V. Houskova, S. Bakardjieva and N. Murafa, *Acs Applied Materials & Interfaces*, 2010, 2, 575-580.
90. A. Kudo, H. Kato and I. Tsuji, *Chemistry Letters*, 2004, 33, 1534-1539.
91. X. Zhao, W. Jin, J. Cai, J. Ye, Z. Li, Y. Ma, J. Xie and L. Qi, *Advanced Functional Materials*, 2011, 21.
92. J. M. Li and D. S. Xu, *Chem. Commun.*, 2010, 46, 2301-2303.
93. N. Feng, A. Zheng, Q. Wang, P. Ren, X. Gao, S.-B. Liu, Z. Shen, T. Chen and F. Deng, *Journal of Physical Chemistry C*, 2011, 115, 2709-2719.
94. A. Mills and M. A. Valenzuela, *Journal of Photochemistry and Photobiology A: Chemistry*, 2004, 165, 25-34.
95. S. Elouali, A. Mills, I. P. Parkin, E. Bailey, P. F. McMillan and J. A. Darr, *Journal of Photochemistry and Photobiology a-Chemistry*, 2010, 216, 110-114.
96. M. W. Kanan and D. G. Nocera, *Science*, 2008, 321, 1072-1075.
97. M. G. Walter, E. L. Warren, J. R. McKone, S. W. Boettcher, Q. Mi, E. A. Santori and N. S. Lewis, *Chem. Rev.*, 2010, 110.
98. F. Meng, J. Li, S. K. Cushing, J. Bright, M. Zhi, J. D. Rowley, Z. Hong, A. Manivannan, A. D. Bristow and N. Wu, *Acs Catalysis*, 2013, 3, 746-751.
99. S. Saremi-Yarahmadi, K. G. U. Wijayantha, A. A. Tahir and B. Vaidhyanathan, *Journal of Physical Chemistry C*, 2009, 113.
100. T. K. Townsend, E. M. Sabio, N. D. Browning and F. E. Osterloh, *Energy Environ. Sci.*, 2011, 4, 4270-4275.
101. J. X. Zhu, Z. Y. Yin, D. Yang, T. Sun, H. Yu, H. E. Hoster, H. H. Hng, H. Zhang and Q. Y. Yan, *Energy Environ. Sci.*, 2013, 6, 987-993.
102. I. R. Beattie and T. R. Gilson, *Journal of the Chemical Society a -Inorganic Physical Theoretical*, 1970, DOI: 10.1039/j19700000980, 980-&.
103. A. M. Jubb and H. C. Allen, *Acs Applied Materials & Interfaces*, 2010, 2, 2804-2812.
104. C. W. Dunnill and I. P. Parkin, *Dalton Transactions*, 2011, 40, 1635-1640.
105. L. Mi, P. Xu, H. Shen and P. N. Wang, *Journal of Photochemistry and Photobiology a-Chemistry*, 2008, 193, 222-227.
106. L. Miao, S. Tanemura, H. Watanabe, Y. Mori, K. Kaneko and S. Toh, *Journal of Crystal Growth*, 2004, 260, 118-124.
107. O. Diwald, T. L. Thompson, E. G. Goralski, S. D. Walck and J. T. Yates, *The Journal of Physical Chemistry B*, 2004, 108, 52-57.
108. H. Lin, C. P. Huang, W. Li, C. Ni, S. I. Shah and Y.-H. Tseng, *Applied Catalysis B-Environmental*, 2006, 68, 1-11.

3 PV-PEC Tandem Devices: Fe_2O_3/ a-Si

The previous chapter explored one type of integrated photoelectrochemical array, the water splitting photodiode. In this chapter, another type of integrated PEC device will be investigated, the PV-PEC tandem device. In this device, a photocatalyst is coupled with a PV cell in order to assist water splitting by applying a photo-induced electrical bias. The use of a PV cell introduces a level of complexity and cost over the photodiode, where a photocatalyst is simply coated onto a metal substrate, but the potential gains in efficiency can compensate for this.

Hematite, (α-Fe_2O_3), has been one of the most intensively studied photocatalysts for water splitting. The suitably sized band gap of hematite (usually reported between 1.9 and 2.2 eV[1]) and the terrestrial abundance of iron make hematite an attractive candidate for large scale solar hydrogen production. Despite this, there are several challenges associated with employing hematite for photo-assisted water splitting, including the position of its conduction band, which is 0.28 V positive of the hydrogen evolution potential. As a result it is unable to split water without the use of an external bias, which can conveniently be provided by the employment of a PV cell as a bottom layer.[2, 3] In this chapter, the chemical vapour deposition of non-doped Fe_2O_3 and Si-doped Fe_2O_3 will be described along with their application in the water splitting photodiode and a PV-PEC tandem device.

3.1 Introduction

Iron is the fourth most abundant element in the earth's crust,[4] and due to the fact it is easily oxidised, (often a cause for concern in the steel industry), iron oxides are widespread and have played an important role in society. Iron oxide has not only served as a precursor to steel, but has also been used as a pigment as early as 32,000 years ago, (famously captured in Werner Herzog's 2010 documentary 'Cave of Forgotten Dreams' on the Lausanne cave paintings). Hematite is so named for its red colour, haima translates to blood in Greek and is still used today as a pigment in paints, cosmetics, food colourants etc.[5] This exemplifies its ability to absorb in the visible portion of the solar spectrum. A high Mohs hardness, (6.5), has also led to the use of hematite as an

abrasive. The properties and uses of the iron oxides are covered in detail in a 2003 book by Cornell and Schwertmann.[6]

3.1.1 Hematite

3.1.1.1 Physical Properties

Iron is able to exist in a wide range of oxidation states, (although +2 and +3 are most commonly observed). As a result, there are 16 naturally occurring forms of iron oxide,[6] of these hematite, (α-Fe_2O_3), where iron is fully oxidised to the +3 state, is the most thermodynamically stable.

Hematite adopts a corundum structure with lattice parameters a = 5.0356 Å and c = 13.7489 Å.[6] The structure can be described in terms of the O^{2-} ions, which adopt a hexagonal close-packed lattice along the [001] direction.[4] Two thirds of the octahedral interstitial sites are filled with Fe^{3+} ions, whilst the tetrahedral sites are vacant. The structure can also be thought of in terms of pairs of FeO_6 octahedra, where each octahedra shares edges with three neighbouring octahedra and a face with another in an adjacent plane, leading to trigonal distortion of the octahedra. The unit cell of hematite is shown in Figure 3.1.

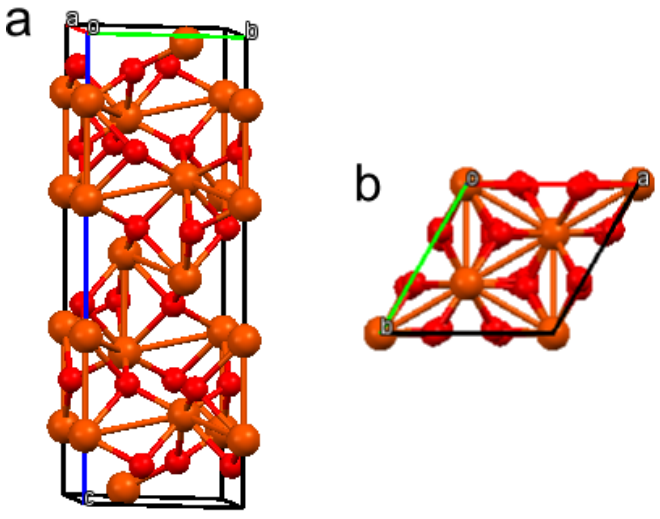

Figure 3.1 Unit cell of α-Fe_2O_3, (where Fe^{3+} is displayed in orange and O^{2-} in red), showing a) the packing of a single unit cell and b) unit cell shown along the c axis

Hematite displays n-type conductivity but is typified by a low charge carrier mobility (electron mobility of 10^{-2} $cm^2.V^{-1}.s^{-1}$).[7-9] The conduction band of hematite is comprised of empty Fe 3d orbitals and ultraviolet photoemission spectroscopy has revealed the valance band consists of overlapping antibonding O 2p and Fe 3d (t_{2g}) orbitals giving rise to a complicated structure about 10 eV wide,[10, 11] Figure 3.2b. An indirect band gap of 1.9-2.2 eV is responsible for hematite's red colour,[1] but there are also optical absorption bands in both the infrared and UV regions due to crystal field and charge transfer transitions,[12] Figure 3.2 a.

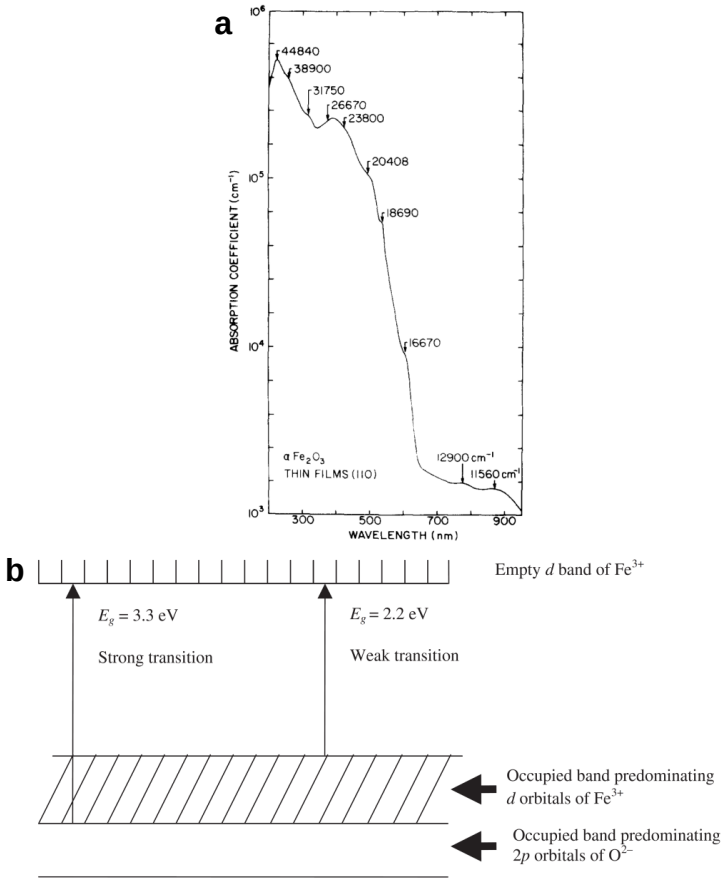

Figure 3.2 a) absorption coefficient as a function of wavelength for α-Fe_2O_3 (reproduced with permission from[12]) and b) band structure of hematite (reproduced with permission from[13])

3.1.1.2 Hematite as a Photocatalyst for Water Splitting

Due to the attractive band gap of hematite α-Fe_2O_3, (1.9-2.2 eV),[1] its excellent chemical stability at pH > 4,[14] (Figure 3.3b), and the terrestrial abundance of iron, hematite has attracted much attention as a water splitting photocatalyst. Despite hematite's band gap

being of the ideal size for a single absorber water splitting material, (at least 1.9 eV, ideally 2.03 eV),[15, 16] the band gap does not straddle the water oxidation and reduction potentials, Figure 3.3a, and so it is unable to split water without the use of an external bias.

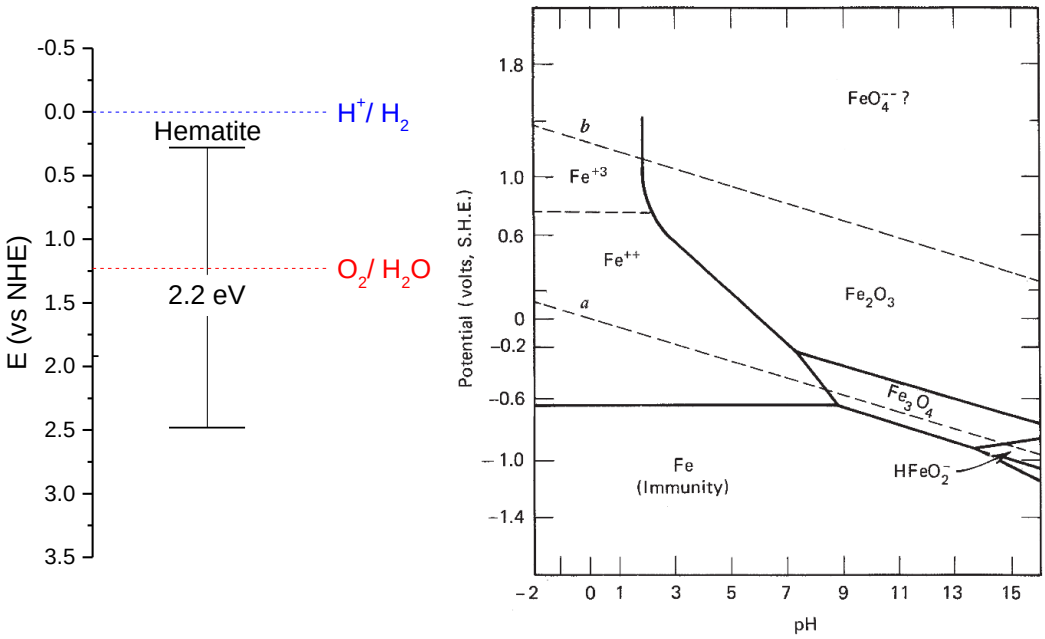

Figure 3.3 a) Valence and conduction band positions of hematite and b) Pourbaix diagram of iron in water (reproduced from with permission from[17])

The ability of hematite to oxidise water was first demonstrated by Hardee and Bard in 1967,[14] where films were deposited using CVD of [Fe(acac)$_3$] on Pt and Ti substrates. Moderate photocurrents of 0.7 mA/cm^2 at +0.4 V vs SCE were obtained using visible light irradiation (yellow filter with <0.1% transmittance below 450 nm) in 1 M NaOH. The films had a photocurrent onset at 550 nm, agreeing with the band gap of hematite. Following this seminal study, hematite was extensively investigated in the late 70's and early 80's, (covered in several reviews[4, 13]) and from these early studies it was concluded that the following issues would have to be addressed for hematite to be adopted as a water splitting photocatalyst:

1. Flat-band potential is too low for water reduction (Figure 3.3a)
2. Large over-potential before the onset of water oxidation is observed

3. Relatively low absorption coefficient at 550 nm (8 x 10^4 cm^{-1}) meaning that films must be at least 400 nm thick for 95% absorption at this wavelength[18]
4. Very short minority charge carrier diffusion length (2 – 4 nm)[19]
5. Poor electron mobility (10^{-2} $cm^2.V^{-1}.s^{-1}$)[7-9]

In order to address the first two points, a multi-junction device can be used, where a PV bottom layer provides the additional bias required.[2, 3, 20] This is particularly pertinent for hematite which is typified by poor photovoltages around 0.6 V, 1.5 V less than the 2.1 eV band gap.[21] In a multi-junction series-connected device the overall current is limited by the minimum photocurrent in any of the cells,[22] thus for application as a PEC material the poor electronic properties of hematite (points 4 and 5) should be improved, which is often achieved through a combination of doping and nanostructuring.

3.1.1.3 Doping of Hematite

Due to a high resistivity, short minority carrier diffusion length and low electron mobility,[19, 23] hematite has a relatively poor photo-response. The conductivity and PEC response of hematite can be improved through the use of chemical doping and both p-type (Cu^{2+}, Zn^{2+}, Mg^{2+}),[24-26] and n-type (Ti^{4+}, Sn^{4+}, Zr^{4+}, Nb^{5+})[9, 27, 28] substitutional dopants have been explored. Moderate conductivities can be achieved with appropriate dopants, for example conductivities of 0.25 $\Omega^{-1}.cm^{-1}$ were achieved with Zr^{4+} doping (vs 10^{-6} $\Omega^{-1}.cm^{-1}$ for pristine hematite).[9]

In particular Si-doped Fe_2O_3 has attracted much attention. Early work on Si-doped Fe_2O_3 indicated that the introduction of Si dopants led to higher photocurrents as compared to another popularly selected dopant Ti, as it was suggested the Ti centres may be acting as recombination sites.[29] In other studies it has been shown that the incorporation of Si into Fe_2O_3 can lead to a small grain size and a high density of surface states, and thus compares unfavourably to other dopants.[30]

Perhaps the most highly cited work on hematite as a water splitting photocatalyst is a 2006 study by Grätzel and co-workers.[31] Vertical atmospheric pressure CVD was used to deposit Si-doped Fe_2O_3 films on FTO substrates at 420 °C using [$Fe(CO)_5$] and tetraethyl orthosilicate (TEOS) precursors. Films consisted of 'cauliflower-like'

nanostructures, (Figure 3.4a and b) with a crystallite size of 5-10 nm for Si doped samples, compared to 20-40 nm for undoped samples. The Si dopant also increased texturing along the (110) plane. High photocurrent densities of 1.8 mA.cm^{-2} (at 1.23 V vs NHE in 1 M NaOH) were achieved in the Si-doped samples as compared to non-doped samples, in which current densities of 10 μA.cm^{-2} were typical. Improved photocurrent density was attributed to enhancement along the basal planes normal to the substrate, as well as the smaller particle size produced in the Si-doped samples resulting in a shorter path-length for minority charge carriers to reach the surface.

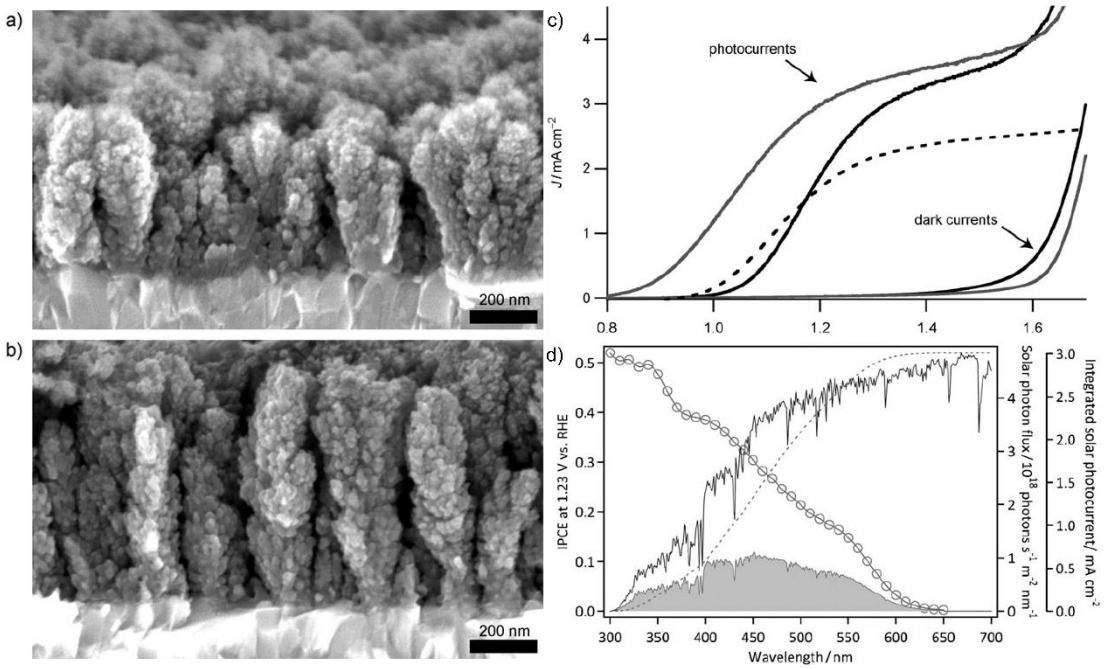

Figure 3.4 Si-doped Fe_2O_3 deposited using APCVD. Cross-sectional SEM images of Si-Fe_2O_3 deposited using a plain flow rate of a) 2 L.min^{-1} air, b) 6 L.min^{-1} air. c) photocurrent density of Si-Fe_2O_3 electrodes prepared with carrier gas flow rate of 2 L.min^{-1} air (dashed line), 6 L.min^{-1} air (black line) and after IrO_2 nanoparticle treatment (grey line). d) IPCE at 1.23 V vs NHE (circles) and AM1.5 trace (black line) are multiplied to give the number of photons stored in the form of hydrogen (shaded area), and photocurrent (dashed line). Reproduced with permission from[32]

In later work by the same group, the particle to precursor ratio was optimised by increasing the carrier gas flow rate to 6 L.min^{-1},[32] resulting in further enhancement along the basal planes normal to the substrate and improved photocurrents of 3 mA.cm^{-2} at 1.23 V vs NHE. Surface treatment of the Si-Fe_2O_3 electrode with IrO_2 nanoparticles led to a 200 mV cathodic shift of photocurrent onset and a current density of 3.3 mA.cm^{-2} at 1.23 V vs NHE, (Figure 3.4c).

The current record photocurrent density for a hematite electrode is 4.32 mA.cm^{-2} at 1.23 V vs NHE (34% of the maximum photocurrent expected from hematite with a band-gap of 2.1 eV), however this required a multi-step high-temperature annealing process, Pt dopant and surface treatment with CoPi,[33] and still had a photocurrent onset >0.6 V vs NHE.

3.1.2 PV-PEC Tandem Devices

Despite the improvement in performance of Fe_2O_3 as a traditional mono-photoelectrode through doping, nanostructuring and co-catalyst loading,[4] (Figure 3.5), efficiencies in this configuration are still poor. Typically a very large external bias is required for overall water splitting, (most often photocurrents are quoted at 1.23 V, the thermodynamic water splitting potential), bringing into question the merits of PEC over standard electrolysis in the dark, Equation 1.21. Consequently the development of a device employing earth abundant materials (such as iron oxide) that does not require the driving force of an external bias is highly desirable.

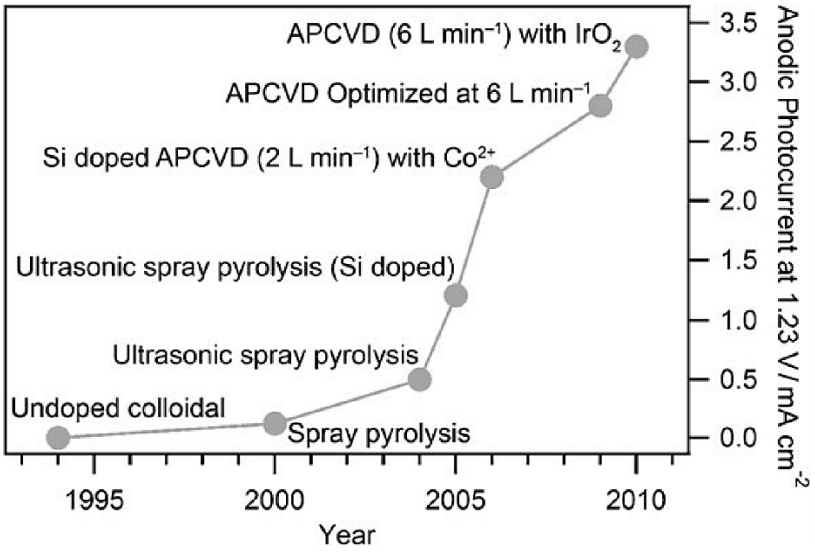

Figure 3.5 Improvement over time in photocurrent density (at 1.23 V vs NHE under 1 sun conditions) obtained from Fe_2O_3 electrodes through a combination of nanostructuring and surface treatment. Reproducedwith permission from[4]

A number of device designs have been explored to achieve unassisted photoelectrochemical water splitting,[34] Section 1.4.2. One promising scheme is to employ a hybrid PV-PEC electrode which couples a metal oxide photoelectrode

material with a photovoltaic solar cell.[2] In this way the solar cell can provide the additional voltage required by the photoelectrode, (the output voltage of a semiconductor is typically 50-70% of the band gap),[22] whilst being protected by the stable oxide material. These components are ideally integrated into a monolithic device, reducing the need for wiring and improving the device efficiency per unit area for the monolith as compared to a configuration where the devices are connected in tandem side by side. Such a device can be sandwiched between two water sources connected by a membrane to evolve oxygen and hydrogen in separate compartments, reducing the need for a costly separation step downstream.[35]

Various different solar cells have been integrated into such devices with high efficiencies including GaAs solar cells,[36] as well as more sophisticated AlGaAs/Si systems,[37] however these are costly and have poor resistance against corrosion. Alternatively dye-sensitised solar cells have been employed in a tandem PV-PEC electrode and moderate efficiencies of 3.1 and 1.17 % were achieved for WO_3 and Fe_2O_3 electrodes respectively.[38] Despite this promising result, the application of DSSCs in a tandem PV-PEC device is somewhat limited by the relatively low V_{OC} output of the cells and so further improvements of the cells is required, or the use of multiple DSSCs connected in series.[39, 40]

Amorphous silicon solar cells have emerged as a popular choice for use in a PV-PEC driven device due to their good stability in a range of pHs, high V_{OC}, and relatively low cost.[41] The concept of a 'hybrid photoelectrode' PV-PEC device was first demonstrated by Miller et al. who reactively sputtered a WO_3 layer onto a double junction a-Si PV cell giving a device efficiency of 0.7% STH.[3] The device showed excellent stability with no degradation in performance over 10 hours of operation in an acidic electrolyte. The efficiency was later improved to 3% STH by optimisation of the WO_3 layer and a-Si cell.[42] Miller et al also investigated hematite as a potential top cell due to the smaller band gap as compared to WO_3 (2.1 vs 2.8 eV) but concluded that due to the large bias required hematite was unsuitable for a PEC-PV-PV type cell.[2, 43]

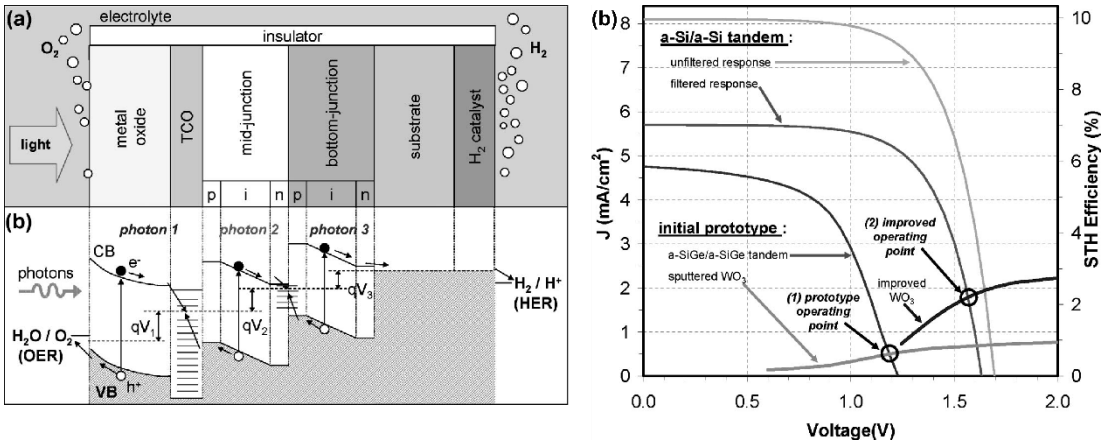

Figure 3.6 a) Schematic representation of PV-PEC monolithic device, b) band diagram of the device illustrating electron and hole pathways from a three photon process and c) load line analysis and predicted operating points of hybrid WO_3/ a-Si device showing optimisation of the device by improvements in the PEC photocurrent in 1M H_3PO_4 and performance of the a-Si device all tested under 1 sun conditions. Reproduced with permission from[44]

It was later shown by Ding et al. that a triple junction amorphous solar cell was indeed more efficient at driving a Fe_2O_3/ a-Si hybrid photoelectrode due to the large bias required by hematite.[45] Films of iron oxide were deposited on FTO substrates using chemical bath deposition and an external wire was used to connect the electrode to the a-Si cell. During testing, electrodes were both submerged in the electrolyte and illuminated either in a tandem or parallel configuration. The use of wiring to connect the two devices adds to the cost and complexity of the overall device design and so it is of interest to create a fully integrated monolithic device, which will be explored in the following section.

3.2 Experimental Methods

3jn a-Si preparation: 3jn a-Si cells were obtained from Xunlight Corporation,[46] and were cut to dimension 25 x 25 mm^2 using a guillotine to minimise distortion of the edges. Platinum was coated onto the reverse side of the substrates in an argon atmosphere using an EMScope SC500 sputter coater at a pressure of 0.1 Torr and current of 35 μA for 4 min. The edges of the cells were then etched with 1M HCl until no coating was visible to reduce shorting. Finally samples were rinsed with distilled water and isopropanol before being dried under N_2.

α-Fe_2O_3 film deposition: Thin films of hematite Fe_2O_3 were deposited in a cold walled CVD reactor using APCVD in a method adapted from the literature.[31] Three different type of substrate were used: Pilkington float glass with an SiO_2 barrier layer, fluorine-doped tin oxide coated glass (Pilkington NSG TEC 15), which was placed directly onto the graphite heating block and 3jn a-Si cells (Xunlight), which were placed onto a 45 x 140 mm^2 piece of float glass and loaded into the reactor. A second piece of float glass served as a top plate and was suspended 5 mm above the glass substrate to ensure laminar flow. Iron(0) pentacarbonyl (Sigma-Aldrich, >99.99%) was used as a precursor and was located in a bubbler maintained at room temperature. Nitrogen (BOC, 99%) was used as a carrier gas with a flow rate of 0.1 $L.min^{-1}$ to transport the precursor to a mixing chamber, where an additional flow of air, 8 $L.min^{-1}$ was introduced. The gas mixture was then passed into the reactor which was heated to 300 °C with a substrate temperature of 280 °C. For Si-doped films tetraethyl orthosilicate (TEOS, Sigma-Aldrich, 99.999%) was used as an additional precursor. The bubbler containing TEOs was held at room temperature and nitrogen was used as a carrier gas with a flow rate of 0.2 $L.min^{-1}$. Samples were heated at 10 °$C.min^{-1}$ under constant nitrogen flow of 1 $L.min^{-1}$. Depositions were carried out for a duration between 5 min and 1 min 15 s.

CAUTION: $Fe(CO)_5$ is toxic and reactions should be carried out in a fumehood.

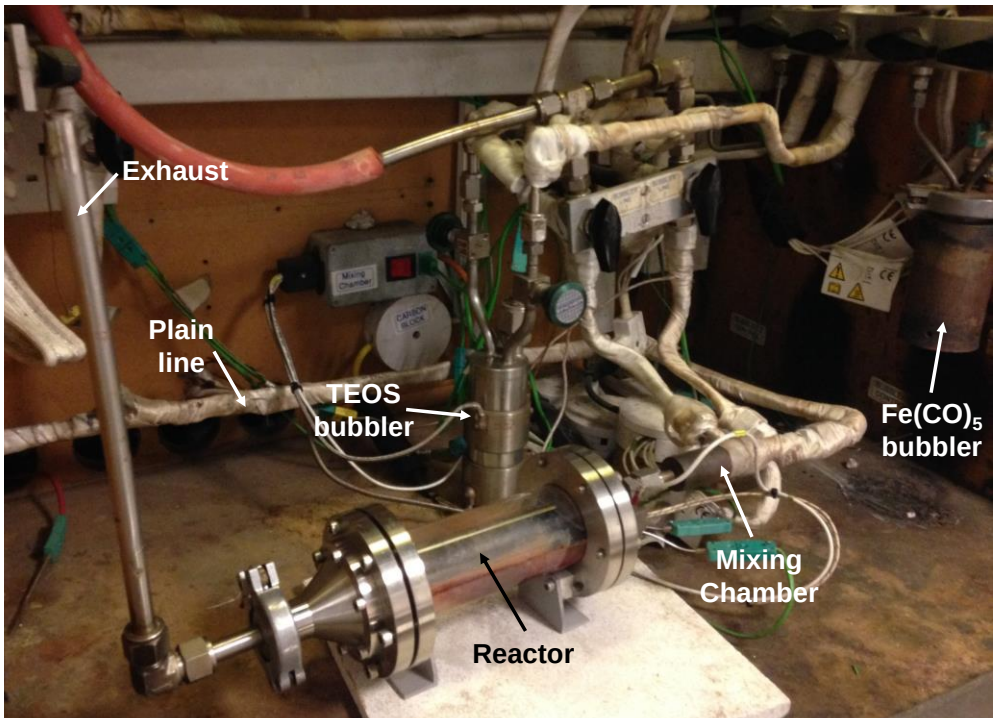

Figure 3.7 Atmospheric pressure CVD rig used for hematite depositions

Characterisation and analysis: Powder X-ray diffraction (PXRD) was used to characterise the hematite films deposited on FTO. A Bruker D8 diffractometer with parallel beam and grazing incidence angle optics equipped with Cu $K_{\alpha 1+2}$ source powered at 40 kV, 40 mA and coupled with a LynxEye silicon strip detector was used. Scans were performed with an incidence angle of 0.5° using a 0.05° step for 4 s/ step and 0.5 slits. Raman spectroscopy was conducted using a Renishaw in Via spectrometer equipped with a 785 nm wavelength laser. X-ray photoelectron spectroscopy (XPS) was used to determine the composition of the films and spectra were recorded on a Thermoscientific K-alpha spectrometer equipped with a monochromated Al K_{α} X-ray source and 180° double focussing hemispherical analyser-128-channel detector. Survey spectra were recorded with energy of 200 eV and higher resolution spectra were recorded at 50 eV. Scanning electron microscopy (SEM) was used to observe surface morphology of the films and determine the thickness of the deposited layer. Imaging was carried out using a JEOL 6301 SEM with secondary electron imaging and accelerating voltage of 5 kV. UV-vis spectra were recorded on a PerkinElmer Lambda 950 spectrometer in transmission mode.

Functional Testing: The performance of the 3jn a-Si cells was determined using current-voltage measurements prior to Fe_2O_3 deposition. Copper tape was used as a current collector for both the anode and the cathode. A thin strip was affixed onto the front of the cell and the steel substrate served as the back contact. The cells were then irradiated with an AM1.5 light source at 1 sun intensity and the current output was measured as a function of the applied voltage, which was swept between 0 and 2.5 with a 0.5 V/s scan rate.

The photocurrent density generated by samples was recorded using an IviumStat potentiostat. Samples were placed in a three electrode quartz cell (Pine Research Instruments) with an $Ag/AgNO_3$ reference electrode and Pt wire counter electrode. Aqueous 1 M NaOH (pH = 13.6) was used to characterise iron oxide films deposited on FTO and 0.1 M K_2HPO_4 (pH = 9.4) was used for the a-Si and Fe_2O_3/ a-Si cells as they were found to be unstable in NaOH. The potential range (usually -0.8 to 1.0 V) was scanned at 50 $mV.s^{-1}$ and three cycles were completed; the first in the dark, the second with light on and the third with the light being chopped. A 75 W xenon arc lamp was used to illuminate the sample equipped with AM1.5G and a neutral density filter (NG11 50% transmission, UQG Optics) to simulate the sun's spectral output with an irradiance of either 300 $mW.cm^{-2}$ or 100 $mW.cm^{-2}$ where an additional neutral density filter was used. (NOTE: samples were measured at 300$mW.cm^{-2}$ prior to the acquisition of a ND filter).

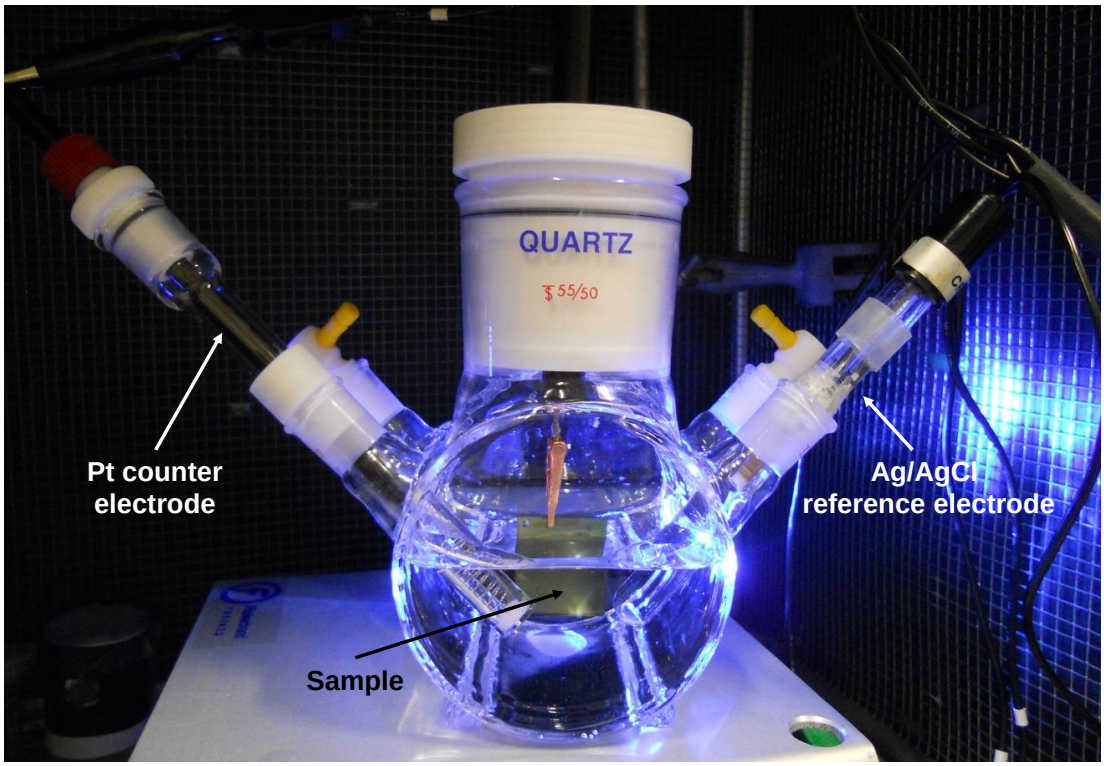

Figure 3.8 Photoelectrochemical cell

3.3 Results and Discussion

3.3.1 α-Fe_2O_3 and Doping Studies

3.3.1.1 Structural Characterisation

Prior to deposition on triple junction amorphous silicon, 3jn a-Si, substrates, the ideal deposition parameters and physical characteristics of Fe_2O_3 and Si-Fe_2O_3 films were determined on glass and FTO coated glass substrates. Those films deposited on FTO coated glass were then selected for photoelectrochemical studies. Iron oxide and Si-doped iron oxide films were deposited on FTO with a substrate temperature of 280 °C, (chosen to be compatible with a-Si processing technology) using iron pentacarbonyl in air.[47] For the Si-doped films, TEOS was used as the silicon source. Films were crack-free and well adhered, with no evidence of delamination on application of the Scotch tape test. The non-doped iron oxide films had a deep red appearance and the Si doped films appeared a pale orange in colour, Figure 3.9.

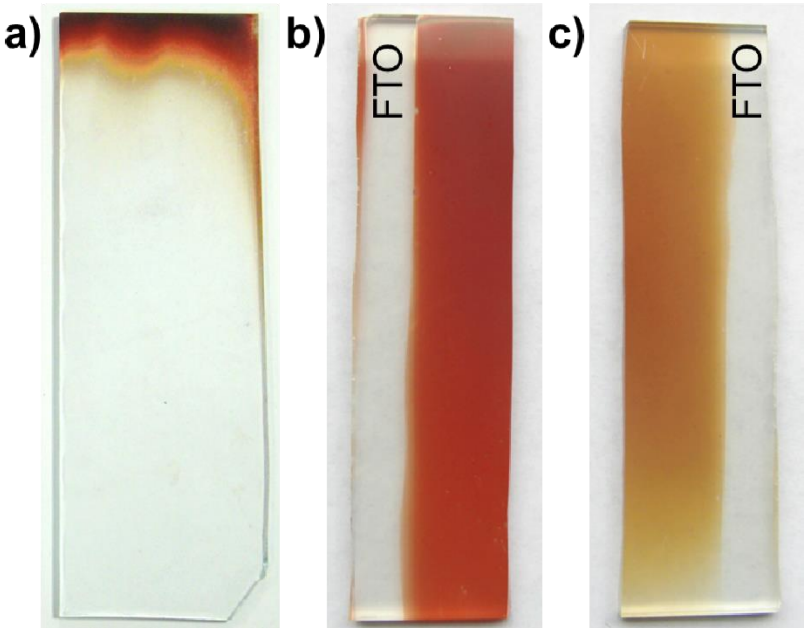

Figure 3.9 a) and b) undoped Fe_2O_3 films deposited by atmospheric pressure CVD in air using $Fe(CO)_5$ as a precursor, a deposition time of 5 minutes and substrate temperature of a) 420 °C and b) 280 °C were used. c) Si-doped Fe_2O_3 using TEOS as an additional precursor and a substrate temperature of 280 °C. Both b) and c) were deposited on FTO coated glass and a contact strip is observable

The effect of temperature on the deposition behaviour of the Fe_2O_3 films was investigated and it was observed that the use of higher substrate temperatures (~420 °C), led to rapid decomposition of the [$Fe(CO)_5$] precursor at the inlet to the reactor (the half-life for decomposition of [$Fe(CO)_5$] at 300 °C is 5.3 ms).[48] This resulted in poor surface coverage of the substrate and the formation of a powdery film on the reactor top-plate, indicating a high rate of reaction and nucleation in the gas phase which is undesirable for the formation of a well adhered film. As a result the lower deposition temperature of 280 °C was selected for device fabrication.

It is interesting to note that the deposition behaviour observed is contrary to the observations of Grätzel et al, who investigated the APCVD of Fe_2O_3 in a 2006 JACS paper.[31] In their work, Fe_2O_3 and Si- Fe_2O_3 were deposited using the same precursors and a substrate temperature of 420 °C. Good surface coverage of the substrate was obtained and it is thought that the difference in surface coverage is attributable to the vertical deposition technique employed by Grätzel et al, whereby the precursor was introduced directly onto the substrate.

Films deposited at 280 °C (a temperature chosen to be compatible with a-Si processing technology) were the hematite phase, Figure 3.10, which has been shown to be active for water oxidation.[31] When films were deposited on FTO, preferential orientation was observed in the (110) plane, whereas in the case of those films deposited directly on glass, a preferential orientation along the (104) plane was observed. This substrate-directing effect has been commonly observed in hematite deposited on conductive SnO_2,[31, 49-51] and is thought to be particularly desirable for Fe_2O_3 when used as a water splitting photocatalyst, as preferential orientation along the (110) plane implies that the most conductive (001) plane is aligned vertically to the substrate.[52] Those films which had the additional TEOS precursor during deposition were found to be amorphous.

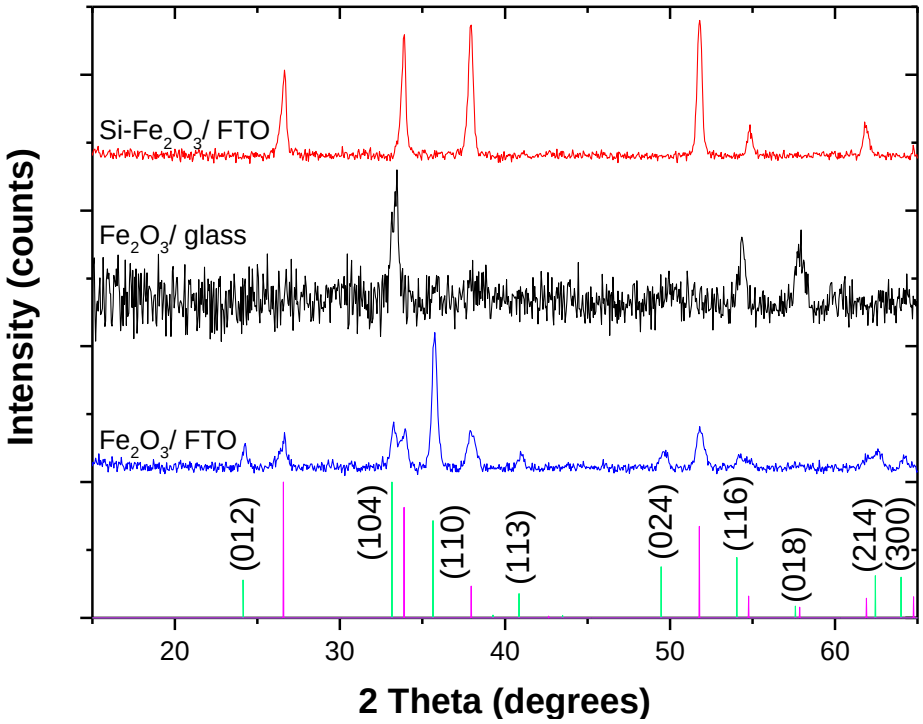

Figure 3.10 XRD pattern of Fe_2O_3 deposited at 280 °C on FTO coated glass (blue), float glass (black), Si-doped Fe_2O_3 deposited on FTO. Standard diffraction patterns have also been included where green is hematite (82902-ICSD) with plane indices indicated and magenta is cassiterite (SnO_2, 16635-ICSD)

The Scherrer equation was used to estimate the crystallite size of the films from the broadening of the (110) peak, Equation 2.3. For the undoped films deposited on FTO the crystallite size was found to be ~ 60 nm, much larger than the 20-40 nm reported by Grätzel et al using the same precursor.[31] This difference is likely caused by the lower deposition temperature leading to a lower nucleation rate.

SEM showed the films were comprised of forest-like clusters of nanoparticles, characteristic of this deposition technique.[31] Interestingly, this microstructure appeared to be maintained on Si doping, despite the amorphous nature of the film. Cross-sectional SEM of an undoped sample deposited on FTO coated glass with a deposition duration of 5 minutes revealed a growth rate of 200 nm/ min.

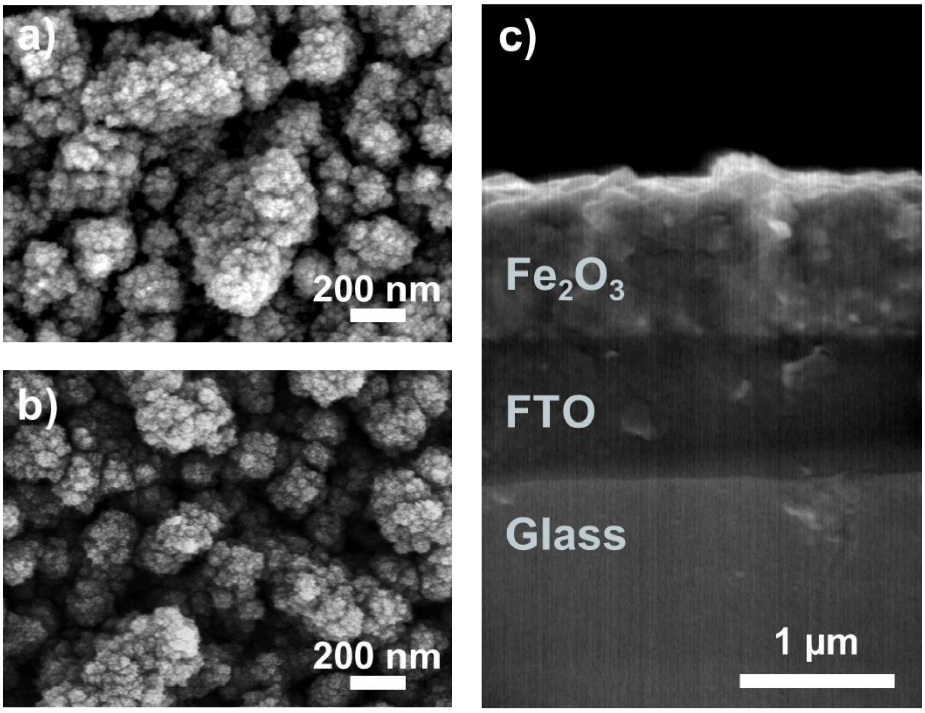

Figure 3.11 SEM images of a) undoped and b) Si-doped Fe_2O_3 deposited for 5 min on FTO coated glass and c) cross-sectional view of undoped Fe_2O_3 showing layer thickness.

Raman spectra were taken of the samples and were in agreement results obtained from XRD analysis. For the undoped Fe_2O_3 film deposited on FTO, peaks characteristic of hematite were observed at 221.8 (A_{1g}), 242.1 (E_g), 287.7 (E_g), 298.0 (E_g), 405.3 (E_g), 492.0 (A_{1g}) and 608.8 cm^{-1} (E_g).[53-55] The undoped film deposited on glass also had peaks associated with hematite at 289.5 296.4, 407.7, 606.4 cm^{-1}, although they were fewer in number and smaller in intensity, indicating the directing effect of the FTO substrate. The spectra of the Si-doped sample showed no peaks associated with hematite and resembled that of the underlying FTO coated glass substrate indicating that the film is amorphous. Amorphous Fe_2O_3 shows broad bands between 450-700 cm^{-1} due to the Fe-O vibration mode,[56] but in this case such bands are not distinguishable due to the strong signal from the substrate.

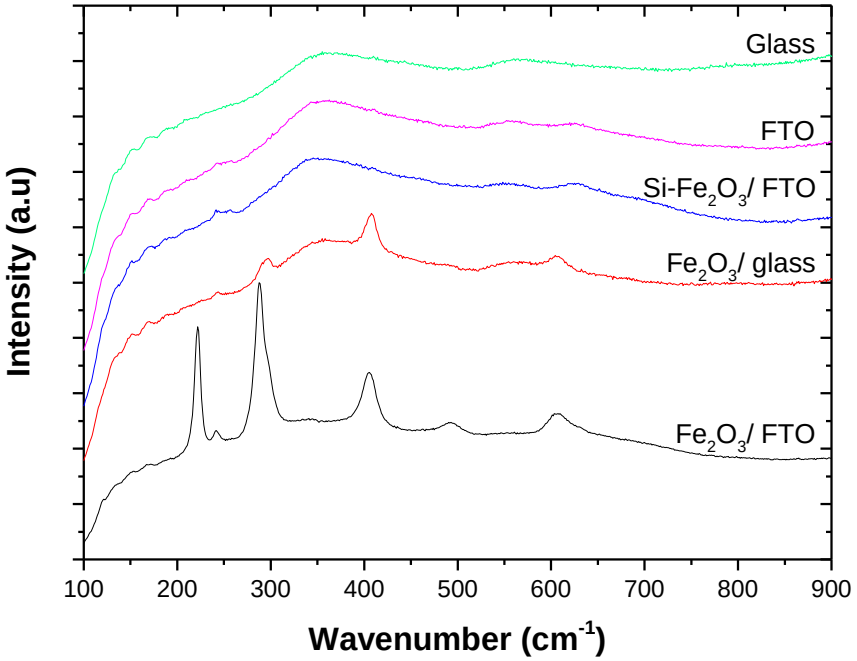

Figure 3.12 Raman spectra of Fe_2O_3 deposited at 280 °C on FTO and glass, Si-Fe_2O_3 deposited on FTO, the FTO coated substrate and glass substrate used

The samples were analysed using XPS to determine the Si content and chemical environment. Fitting of the $2p_{3/2}$ peak in high-spin Fe^{3+} and Fe^{2+} is particularly problematic due significant broadening of the peak as compared to $Fe^{(0)}$ metal or low-spin Fe^{2+}.[57] This broadening has been shown to be caused by spin orbit coupling between the 2p core hole and unpaired 3d electrons of the photoionised Fe cation and the inclusion of crystal field and electrostatic interactions.[58, 59] The Fe $2p_{3/2}$ peaks were fit using CasaXPS and employing the multiplet structure originally calculated by Gupta and Sen, later refined by others.[60, 61] According to this model, the $2p_{3/2}$ envelope can be fit with four peaks at ~ 709, 710, 711 and 712 eV, an additional 'surface peak' due to surface structures at ~ 715 eV and a broad satellite peak at ~719 eV due to shake up and charge transfer processes.[60]

The undoped Fe_2O_3 sample fit the model for α-Fe_2O_3 well, Figure 3.13, but on Si-doping a shift to higher binding energy of the Fe 2p peaks was observed, which suggests Fe in a higher oxidation state. Also, the peak shape did not fit well to that of Fe^{3+}. The Si 2p doublet was fit using a separation of 0.6 eV,[62] and a binding energy of 101.7 eV was observed for the Si $2p_{3/2}$ peak, indicative of Si in SiO_x,[63, 64] (reduced compared to SiO_2 which has binding energies typically ~103 – 104 eV).[63, 65] A ratio of 1:0.75 for Fe:Si was observed, much higher than the optimum dopant level of Si^{4+} into the hematite

lattice, which was determined to be 1.6 at% by Grätzel et al. From the high at% of Si, coupled with the amorphous nature of the film from XRD and Raman results in the material presented here, it is stipulated that an amorphous iron-silicon oxide material is present. Further structural characterisation to probe the local environment of the atoms would be required to confirm this, which could be carried out using extended X-ray absorption fine structure spectroscopy, EXAFS, for example.

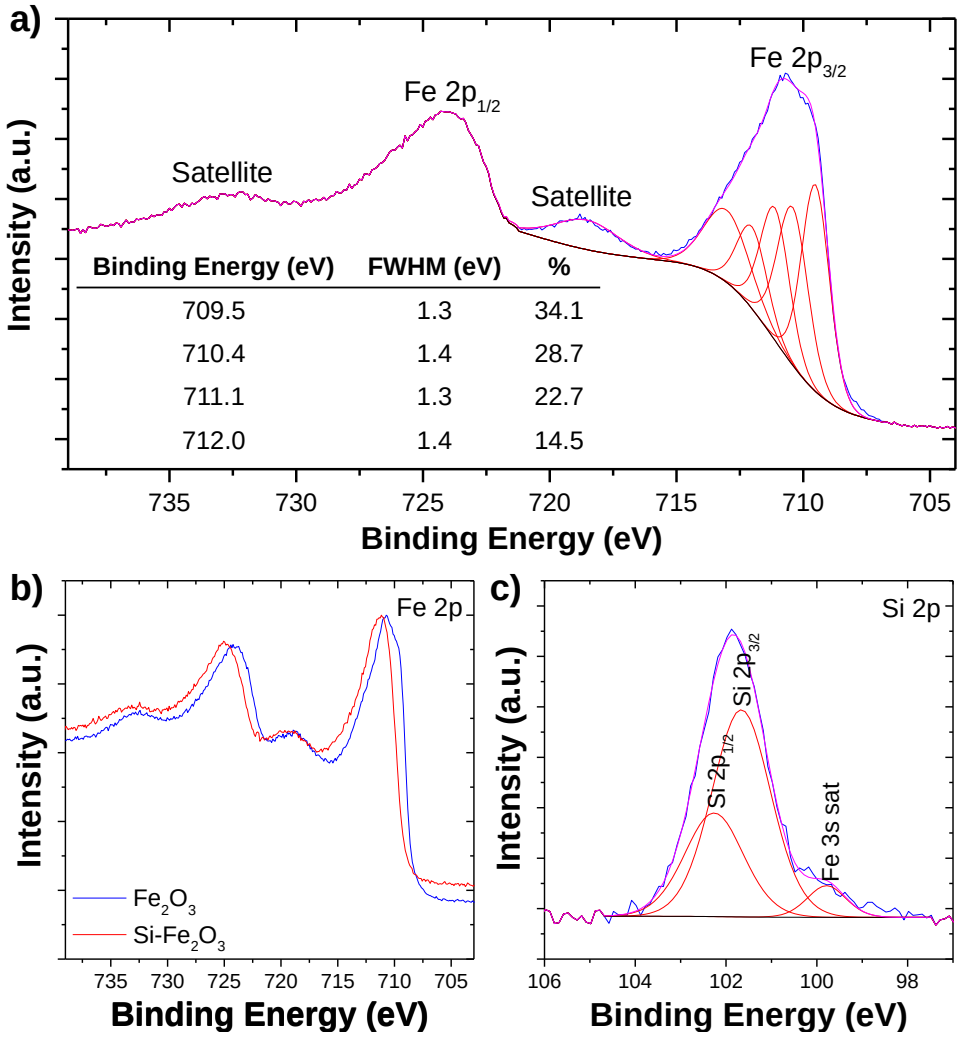

Figure 3.13 XPS of undoped and Si-doped Fe_2O_3 showing a) undoped Fe_2O_3 $2p_{3/2}$ peak fit using the Gupta and Sen multiplets,[58, 59] b) undoped and Si doped Fe_2O_3 2p region showing a shift to higher binding energy of the 2p peaks of Si doping, and c) Si 2p region for Si-doped Fe_2O_3

The optical characteristics of non-doped and Si-doped films deposited on glass were determined using UV-vis spectrometry. Spectra were captured in transmission mode and the absorbance was determined from Equation 1.7, shown in Figure 3.14.

Tauc plots were used to calculate the band gap of the material, Figure 3.14, which is usually considered to be indirect.[19]

The undoped iron oxide film had an indirect band gap of 2.1 eV, consistent with values typically reported.[1] A second transition was observable at 3.2 eV, which is attributable to a direct O 2p → Fe^{3+} 3d transition.[13] The Si doped Fe_2O_3 had much weaker absorption coefficients in the region of the hematite band gap ($\alpha<10^4$ cm^{-1}) thus the transition cannot be accurately modelled by Equation 1.9. This is due to the presence of an exponential tail which means fitting a tangent to a point within this tail will underestimate the band gap of the material.[66]

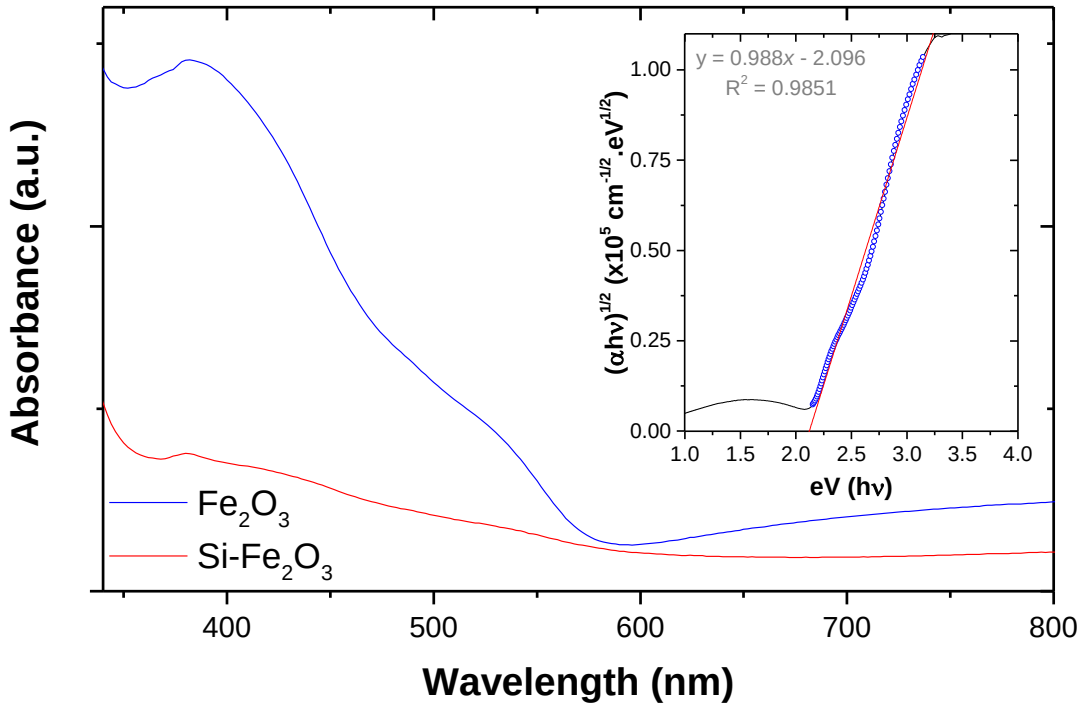

Figure 3.14 Absorbance spectra of Fe_2O_3 and Si-doped Fe_2O_3 deposited on glass and Tauc plot of Fe_2O_3 (inset)

3.3.1.2 Photoelectrochemical Testing

The photocurrent density as a function of applied voltage (under 3 sun AM1.5 irradiation in 1 M NaOH) produced by the samples deposited for 5 minutes on FTO was assessed and is presented in Figure 3.15a. It was found that on Si-doping the photocurrent at 1.23 V vs NHE was drastically reduced from 0.1 $mA.cm^{-2}$ for pristine Fe_2O_3 to 0.02 $mA.cm^{-2}$ for Si-doped Fe_2O_3. This can be accounted for by the

amorphous nature of the Si-doped film, high Si content and much lower absorption coefficient.

The effect of thickness on the photocurrent density generated was investigated and it was found that a deposition time of 2 min 30 s was optimal, giving a film thickness of 500 nm. This enhancement in photocurrent on reduction of the film thickness is likely due to a trade-off between light absorption and charge-carrier pathlength.[4] The best performing sample showed a photocurrent density of 0.6 mA.cm^{-2} at 1.23V vs NHE (0.4 mA.cm^{-2} at 1.23V vs NHE when tested under 1 sun) in NaOH, far outperforming the values reported by Grätzel et al for undoped hematite, who saw photocurrents of 10 μA cm^{-2} at 1.23 V vs NHE. The use of a higher plain flow of air (8 vs 2 L.min^{-1}) could be the cause of the relative increase in photocurrent, as it has been shown that altering the particle to precursor ratio can greatly improve the photocurrent in a Si-doped Fe_2O_3 system.[67] This photocurrent is also in line with that produced by several undoped Fe_2O_3 films deposited using ultrasonic spray pyrolysis (USP).[68, 69]

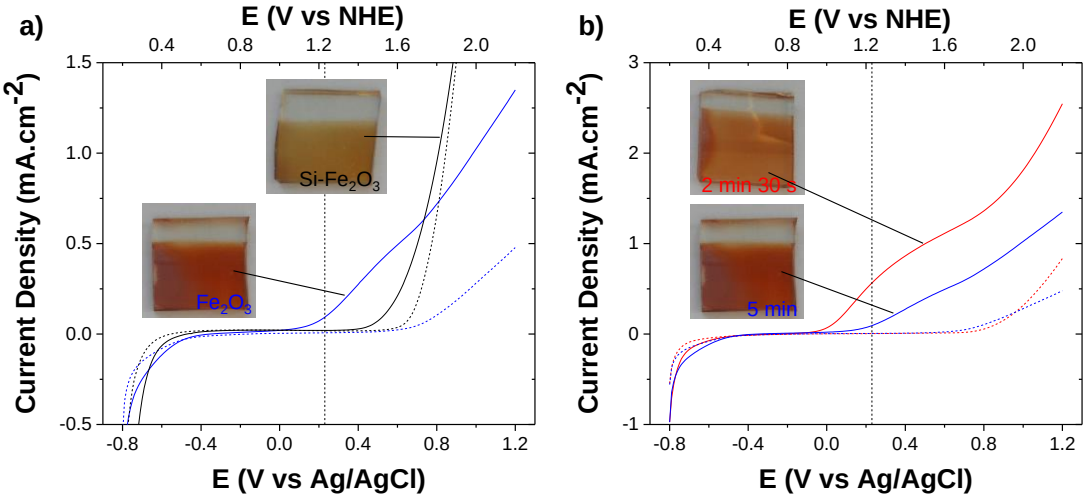

Figure 3.15 PEC measurements where solid = light current, dash = dark current of a) undoped and Si-doped Fe_2O_3 deposited for 5 min and b) undoped Fe_2O_3 deposited for 5 min and 2 min 30 s showing the effect of thickness on photocurrent. Samples were tested in 1 M NaOH under 3 sun AM1.5 irradiation.

3.3.2 Tandem PV/PEC device

Despite the moderate photocurrent at 1.23 V vs NHE achieved in the optimised undoped Fe_2O_3 sample deposited on FTO, the overall device efficiency is effectively negligible due to the large voltage input required for the onset of photocurrent (1000

mV), Equation 1.21. As a result, the deposition of Fe_2O_3 onto a triple junction a-Si solar cell was investigated, which is known to provide the large bias required for water oxidation by hematite.[45]

Iron oxide was deposited in a low temperature APCVD process, as described in 3.3.1.1, onto triple junction amorphous silicon solar cells, (cells begin to degrade when subjected to T > 300 °C),[70] purchased from Xunlight Corporation. This gave the overall hybrid PV/PEC device structure as illustrated in Figure 3.16. The 3jn a-Si cell has an ITO top contact but due to the processing temperature limitations of a-Si cells, this is usually deposited using a sputtering technique and is amorphous. As a result the directing effect of the hematite seen in films deposited on crystalline SnO_2 is not observed and XRD of the hematite film showed it to be amorphous, with no peaks attributable to hematite observable.

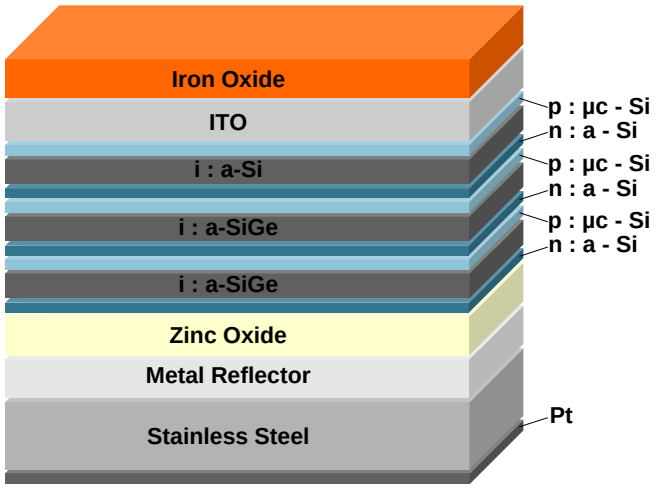

Figure 3.16 Design of the PV/PEC hybrid device

Raman spectroscopy was used to probe the bonding of the Fe_2O_3 layer in the Fe_2O_3/a-Si device. Firstly a spectrum of the uncoated 3jn a-Si cell was captured and can be seen in Figure 3.17. Amorphous silicon shows four distinct phonon bands at ~ 140, 300, 380 and 475 cm^{-1}, corresponding to transverse acoustic (TA), longitudinal acoustic (LA), longitudinal optical (LO) and transverse optical (TO) bands respectively.[71, 72] The sample displayed distinct peaks at 476 and 390 cm^{-1} corresponding to TO and LO phonon bands and weaker peaks at ~260 and 150 cm^{-1} corresponding to LA and TA phonon bands. After deposition of the Fe_2O_3, these bands were still observable, with no

distinct peaks attributable to hematite, indicating the amorphous nature of the film due to a lack of a directing effect from crystalline SnO_2.

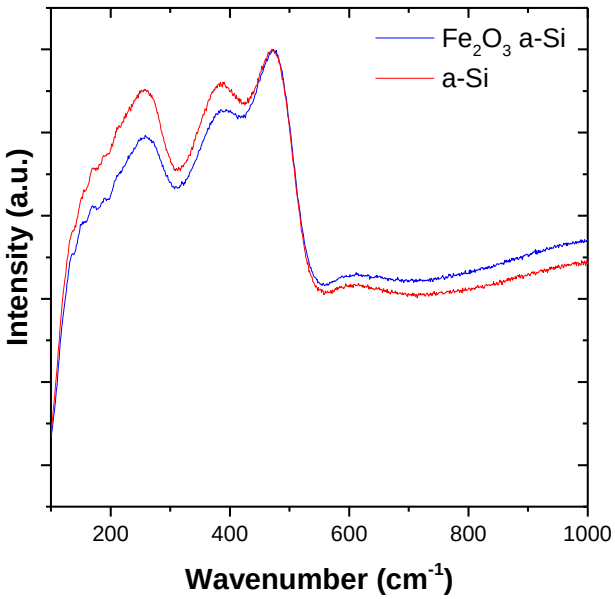

Figure 3.17 Raman of unmodified 3jn a-Si cell and Fe_2O_3 coated 3jn a-Si cell

SEM of the Fe_2O_3/ a-Si device showed the nanoparticulate microstructure of the Fe_2O_3 layer was retained when deposited on the a-Si cells, albeit with particles that are smaller in appearance, Figure 3.18.

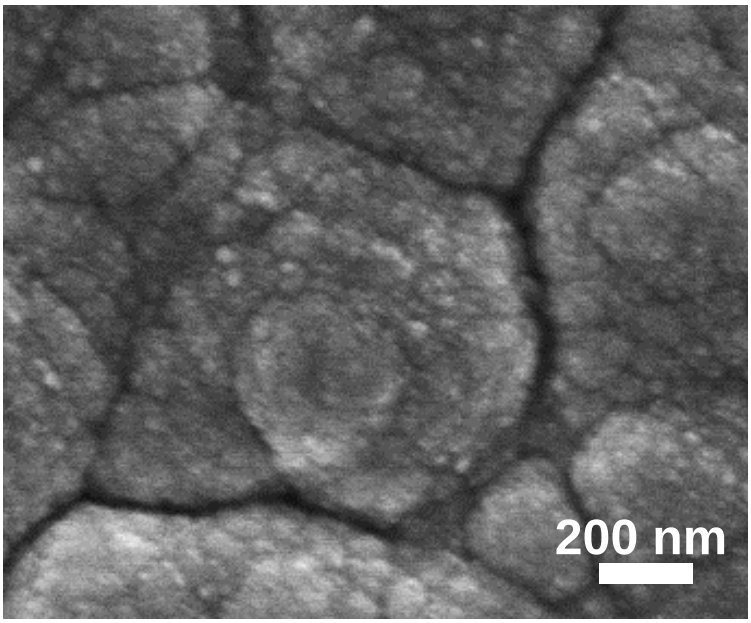

Figure 3.18 Top-down SEM of the Fe_2O_3/ a-Si device showing the nanoparticulate microstructure of the surface Fe_2O_3 layer

Since the Fe_2O_3 layer appeared amorphous from XRD and Raman analysis, XPS was used to determine the oxidation state of Fe in the film. The binding energies obtained were consistent with Fe in a 3+ state and the 2p peaks fit the Gupta and Sen multiplets well.[58, 59] The peak shape and binding energy of the Fe_2O_3/ a-Si film also matched the spectrum of Fe_2O_3 deposited onto FTO well, Figure 3.19. A slight shift in binding energy of the peaks (+0.04 eV) relative to the undoped Fe_2O_3 sample deposited on FTO was observed, likely due to the amorphous nature of the film leading to a slightly altered chemical environment.

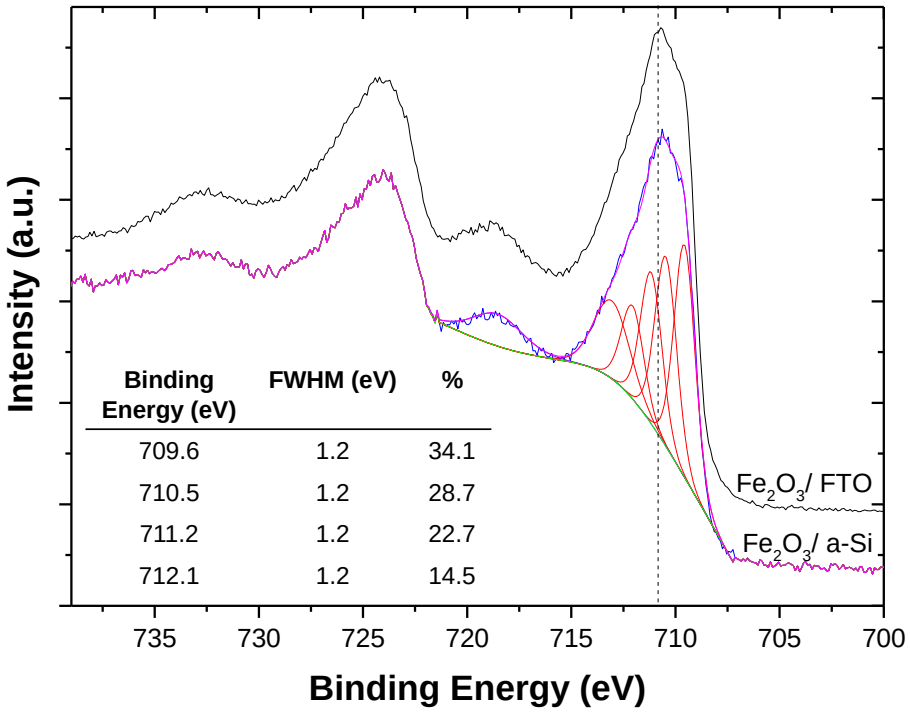

Figure 3.19 XPS of amorphous Fe_2O_3 deposited on triple junction amorphous silicon substrates and fit using the Gupta and Sen multiplets.[58, 59] The XPS spectrum of crystalline Fe_2O_3 deposited onto FTO is also shown for comparison, indicating that the amorphous Fe_2O_3 contains Fe in a 3+ state.

In order to predict the operating point of the device, a load-line analysis was carried out, which involves overlaying the photocurrent of the PEC component in the chosen electrolyte with the dry IV curve of the PV cell.[20] In this case, the photocurrent of the iron oxide when tested in K_2HPO_4 is selected as the device is unstable in NaOH, (likely due to the porous nature of the deposited iron oxide film). A comparison of the photocurrent generated by Fe_2O_3/FTO in 1 M NaOH (pH 13.6) and 0.1 M KPi (pH 9.4) is shown in Figure 3.20. It was observed that lower photocurrents were yielded in KPi (5 $\mu A.cm^{-2}$ at 1.23V vs NHE compared to 0.4 $mA.cm^{-2}$ when tested in NaOH). This is due to the milder pH of the KPi and is a well-known phenomenon, particularly for hematite whose charge carriers have a very short lifetime. At higher pH, OH^- effectively acts as a hole scavenger to form $OH^\bullet$ radicals allowing electrons to diffuse to the back contact.[14, 21, 73] Furthermore at a pH of 9.4, the surface of hematite is close to the point of zero charge, (pH = 8.6), but would be highly charged at a pH of 13.6 leading to higher band bending at the semiconductor/ electrolyte interface.[74]

The 3jn a-Si cell was found to perform with an overall efficiency of 5 % (j_{SC} = 5.5 $mA.cm^{-2}$, V_{OC} = 2.2 V, FF = 41.3 %). This is low compared to the best performing

samples in the literature, which have a record efficiency of 13.4 %,[75] showing clear scope for improvement of the device. After deposition of the iron oxide film on the a-Si cell, the overall efficiency of the cell was reduced to 1.4% (j_{SC} = 2.4 mA.cm^{-2}, V_{OC} = 1.9 V, FF = 30.4 %). This shunting effect is likely caused by shadowing of the 3jn a-Si cell by the Fe_2O_3 or by damage on heating to 280 °C during the deposition.

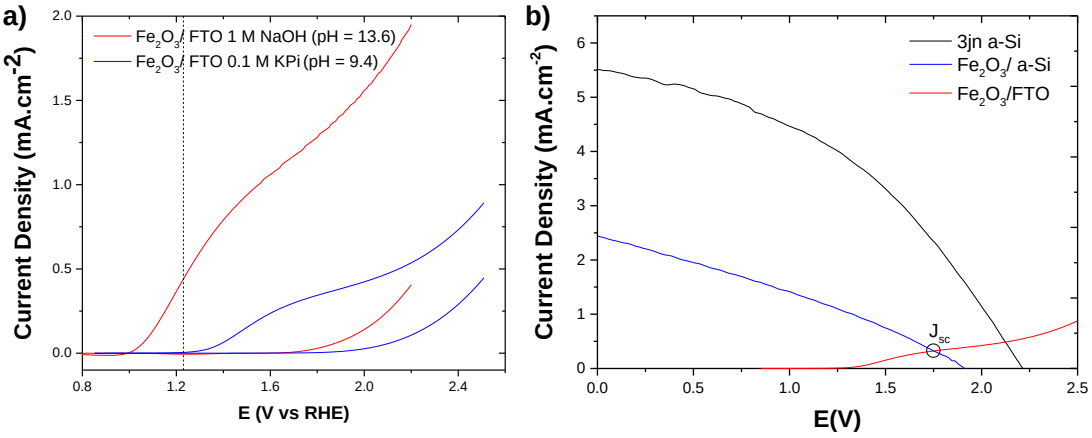

Figure 3.20 a) PEC of Fe_2O_3 in different electrolytes tested under 1 sun AM1.5 conditions (dash = dark curve, solid = illuminated curve) and b) load line analysis of photocurrent generated by Fe_2O_3 in KPi, 3jn a-Si cell and 3jn a-Si cell shadowed by Fe_2O_3

The net current is limited by the poorest performing component of the cell,[22] in this case the iron oxide PEC layer. Due to the relatively poor performance of the Fe_2O_3 (5 μA.cm^{-2} at 1.23 V vs NHE in 0.1 M K_2HPO_4) the predicted operating point of the hybrid cell is 0.32 mA.cm^{-2} at 0 V vs NHE (at the open circuit potential), Figure 3.20 or 0.4% solar-to-hydrogen (STH) efficiency.[76] After deposition of the iron oxide film on the 3jn a-Si substrate the photocurrent density was recorded and it was observed that the Fe_2O_3/a-Si tandem cell greatly outperformed the individual components, with a photocurrent of 1.04 mA.cm^{-2} at 1.23 V vs NHE, compared to 5 μA.cm^{-2} for the iron oxide and 15 μA.cm^{-2} for the unmodified 3jn a-Si cell. Despite the two order of magnitude performance enhancement, the Fe_2O_3/a-Si device does not operate at the predicted 0.32 mA.cm^{-2} at 0 V vs NHE and required another 550 mV bias in order to reach this value. The device performed relatively poorly as compared to similar systems in the literature, for example a Fe_2O_3/ a-Si tandem device reported by Ding et al, where the Fe_2O_3 layer was deposited on an FTO electrode coupled to an a-Si cell either in tandem or parallel.[45] They found that the device connected in a parallel (side-by-side)

configuration performed better due to the increased light absorption of the Si cell and their device performed ~3 times better at 0 V vs Ag/AgCl as compared to the system reported here. There are several reasons why this might be the case. Firstly in the system reported by Ding et al, the a-Si cell had a much higher efficiency than the cell used in this work, (about two times higher, however the true efficiency of their a-Si cell cannot be calculated since they did not report the FF, only the V_{OC} and J_{SC}). Secondly in the system reported by Ding et al, the Fe_2O_3 was not directly deposited onto the a-Si cell but onto FTO using chemical bath deposition followed by annealing. This meant their Fe_2O_3 layer would likely have had enhanced crystallinity as compared to the system here (however no XRD pattern for the hematite was reported), where the deposition temperature was limited by the low-temperature requirement of the a-Si cell. Furthermore, even the moderate heating of the a-Si cell in the work reported here may have resulted in efficiency losses of the a-Si cell, as is evident from Figure 3.20.

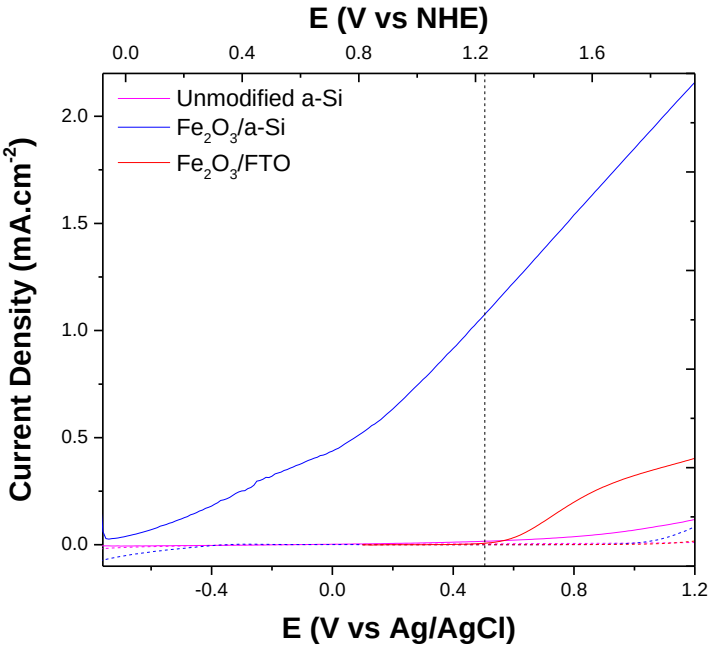

Figure 3.21 PEC in 0.1 M KPi (pH 9.4) of unmodified a-Si, tandem Fe2O3/ a-Si and Fe2O3 FTO tested under AM1.5 1 sun conditions

The effect of Fe_2O_3 layer thickness on the device performance was investigated using three different deposition durations of 1 minute 15 seconds, 2 minutes 30 seconds, and 5 minutes. From the growth rate of undoped Fe_2O_3 on FTO, Figure 3.11, these deposition times would be expected to give layer thicknesses of 250 nm, 500 nm

and 1 m respectively. It was observed that a deposition time of 2 min 30 s was optimal giving the highest photocurrent at 1 V vs NHE, Figure 3.22. This is thought to be due to a trade-off between absorption and charge carrier diffusion length.

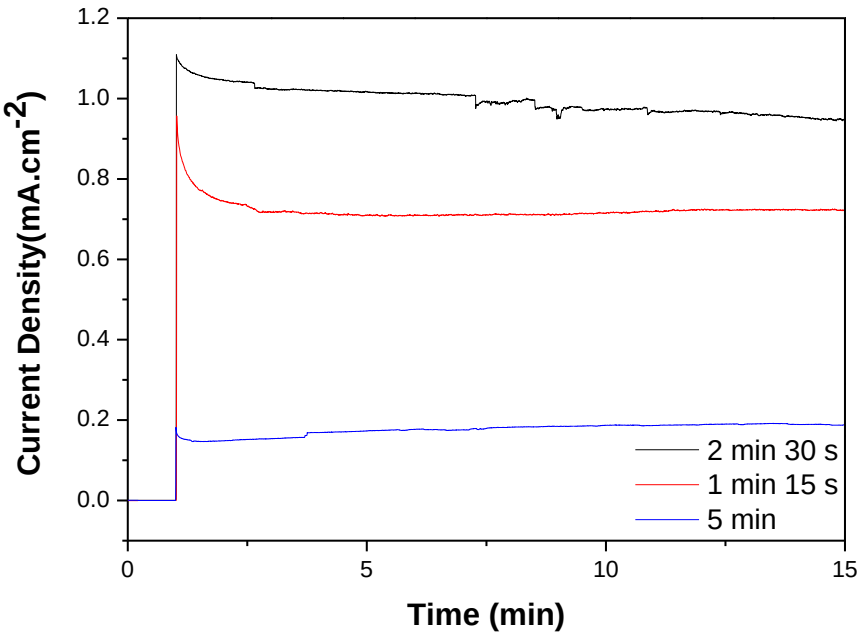

Figure 3.22 Chronoamperometry of Fe_2O_3/ a-Si with varying thickness at 1 V vs NHE

Chronoamperometry was carried out on the three different Fe_2O_3/ a-Si devices in 0.1 M KPi at 1 V vs NHE for an initial period of 15 minutes to determine how stable the devices were under operation, Figure 3.22. When the light is turned on, a current spike followed by a decrease down to a stable value, is observed. The initial current spike is caused by both a non-Faradaic process caused by the charging of the double layer and conversion of reaction intermediates already bound to the surface. The subsequent decrease is a consequence of mass transport limitation, which rapidly reaches a stable level. The devices were stable with minimal reduction in photocurrent. The photocurrent for the Fe_2O_3/ a-Si sample which had a Fe_2O_3 deposition time of 2 minutes 30 s did appear to fall slightly, but this was due to the build-up of bubbles on the Fe_2O_3 surface. The photocurrent was returned to its original value after switching the light source off and allowing the bubbles to leave the photocatalyst surface.

3.4 Conclusions

Non-doped and 'Si-doped' iron oxide films were deposited in a low temperature APCVD process using [$Fe(CO)_5$] and TEOS precursors. The non-doped films adopted the hematite structure and displayed substrate-directing effects depending whether they were deposited on glass or FTO coated glass, which promoted orientation in the (104) and (110) planes respectively. On Si doping, the films became amorphous and a high ratio of Si incorporation was observed. From XPS studies, the chemical environment of the Fe appeared to change and it was thought an amorphous iron-silicon oxide material was formed. Photoelectrochemical measurements of the Fe_2O_3 films deposited on FTO showed moderate photocurrents of 0.4 $mA.cm^{-2}$ at 1.23 V vs NHE when tested in 1M NaOH under 1 sun irradiation.

Fe_2O_3/ a-Si tandem devices were fabricated by directly depositing Fe_2O_3 films onto triple junction solar cells using APCVD. The films were amorphous but iron was confirmed to be Fe^{3+} from XPS results. Load line analysis predicted an operating point of 0.32 $mA.cm^{-1}$ for the device however an additional bias of ~550 mV was required to reach this. It is thought that this is due to the amorphous nature of the iron oxide film. Despite this, a photocurrent enhancement was seen for the tandem device as compared to the individual components. Utilisation of this device configuration in a practical system would require further development of the iron oxide film, however this work highlights the promise of PV/ PEC cells as potentially efficient water splitting devices. It was demonstrated that the PV cell is able to boost the performance of the PEC component and that low-cost metal oxide films can be used as a replacement for catalyst films deposited electrochemically.

3.5 References

1. T. Lindgren, L. Vayssieres, H. Wang and S. E. Lindquist, *Chemical Physics of Nanostructured Semiconductors*, 2003, 83-110.
2. E. L. Miller, R. E. Rocheleau and X. M. Deng, *Int. J. Hydrog. Energy*, 2003, 28, 615-623.
3. E. L. Miller, D. Paluselli, B. Marsen and R. E. Rocheleau, *Solar Energy Materials and Solar Cells*, 2005, 88, 131-144.
4. K. Sivula, F. Le Formal and M. Gratzel, *ChemSusChem*, 2011, 4, 432-449.
5. R. M. Cornell and U. Schwertmann, in *The Iron Oxides*, Wiley-VCH Verlag GmbH & Co. KGaA, 2004, DOI: 10.1002/3527602097.ch19, pp. 509-524.
6. R. M. Cornell and U. Schwertmann, in *The Iron Oxides*, Wiley-VCH Verlag GmbH & Co. KGaA, 2004, DOI: 10.1002/3527602097.ch1, pp. 1-7.
7. F. J. Morin, *Phys. Rev.*, 1951, 83, 1005-1010.
8. J. Engel and H. L. Tuller, *Physical Chemistry Chemical Physics*, 2014, 16, 11374-11380.
9. J. C. Launay and G. Horowitz, *Journal of Crystal Growth*, 1982, 57, 118-124.
10. R. L. Kurtz and V. E. Henrich, *Physical Review B*, 1987, 36, 3413-3421.
11. R. M. Cornell and U. Schwertmann, in *The Iron Oxides*, Wiley-VCH Verlag GmbH & Co. KGaA, 2004, DOI: 10.1002/3527602097.ch6, pp. 111-137.
12. L. A. Marusak, R. Messier and W. B. White, *J. Phys. Chem. Solids*, 1980, 41, 981-984.
13. V. R. Satsangi, S. Dass and R. Shrivastav, in *On Solar Hydrogen & Nanotechnology*, John Wiley & Sons, Ltd, 2010, DOI: 10.1002/9780470823996.ch13, pp. 349-397.
14. K. L. Hardee and A. J. Bard, *Journal of the Electrochemical Society*, 1976, 123, 1024-1026.
15. R. van de Krol, in *Photoelectrochemical Hydrogen Production*, eds. R. van de Krol and M. Grätzel, Springer US, 2012, vol. 102, ch. 2, pp. 13-67.
16. A. B. Murphy, P. R. F. Barnes, L. K. Randeniya, I. C. Plumb, I. E. Grey, M. D. Horne and J. A. Glasscock, *Int. J. Hydrog. Energy*, 2006, 31, 1999-2017.
17. R. W. Revie and H. H. Uhlig, in *Corrosion and Corrosion Control*, John Wiley & Sons, Inc., 2008, DOI: 10.1002/9780470277270.ch4, pp. 43-51.
18. T. W. Hamann, *Dalton Transactions*, 2012, 41, 7830-7834.
19. J. H. Kennedy and K. W. Frese, *Journal of the Electrochemical Society*, 1978, 125, 709-714.
20. A. Stavrides, A. Kunrath, J. Hu, R. Treglio, A. Feldman, B. Marsen, B. Cole, E. Miller and A. Madan, San Diego, CA, 2006.
21. B. M. Klahr and T. W. Hamann, *Journal of Physical Chemistry C*, 2011, 115, 8393-8399.
22. E. Miller, A. DeAngelis and S. Mallory, in *Photoelectrochemical Hydrogen Production*, eds. R. van de Krol and M. Grätzel, Springer US, 2012, vol. 102, ch. 7, pp. 205-273.
23. M. P. Dareedwards, J. B. Goodenough, A. Hamnett and P. R. Trevellick, *Journal of the Chemical Society-Faraday Transactions I*, 1983, 79, 2027-2041.
24. W. B. Ingler Jr and S. U. M. Khan, *Int. J. Hydrog. Energy*, 2005, 30, 821-827.
25. W. B. Ingler, J. P. Baltrus and S. U. M. Khan, *Journal of the American Chemical Society*, 2004, 126, 10238-10239.

26. C. Leygraf, M. Hendewerk and G. Somorjai, *Journal of Solid State Chemistry*, 1983, 48, 357-367.
27. N. T. Hahn and C. B. Mullins, *Chem. Mat.*, 2010, 22, 6474-6482.
28. C. Sanchez, M. Hendewerk, K. D. Sieber and G. A. Somorjai, *Journal of Solid State Chemistry*, 1986, 61, 47-55.
29. J. H. Kennedy, R. Shinar and J. P. Ziegler, *Journal of the Electrochemical Society*, 1980, 127, 2307-2309.
30. J. A. Glasscock, P. R. F. Barnes, I. C. Plumb and N. Savvides, *Journal of Physical Chemistry C*, 2007, 111, 16477-16488.
31. A. Kay, I. Cesar and M. Graetzel, *Journal of the American Chemical Society*, 2006, 128, 15714-15721.
32. S. D. Tilley, M. Cornuz, K. Sivula and M. Gratzel, *Angew. Chem.-Int. Edit.*, 2010, 49, 6405-6408.
33. J. Y. Kim, G. Magesh, D. H. Youn, J. W. Jang, J. Kubota, K. Domen and J. S. Lee, *Scientific Reports*, 2013, 3.
34. K. S. Joya, Y. F. Joya, K. Ocakoglu and R. van de Krol, *Angew. Chem.-Int. Edit.*, 2013, 52, 10426-10437.
35. P. Carmichael, D. Hazafy, D. S. Bhachu, A. Mills, J. A. Darr and I. P. Parkin, *Physical Chemistry Chemical Physics*, 2013, 15, 16788-16794.
36. O. Khaselev and J. A. Turner, *Science*, 1998, 280, 425-427.
37. S. Licht, B. Wang, S. Mukerji, T. Soga, M. Umeno and H. Tributsch, *J. Phys. Chem. B*, 2000, 104, 8920-8924.
38. J. Brillet, J.-H. Yum, M. Cornuz, T. Hisatomi, R. Solarska, J. Augustynski, M. Graetzel and K. Sivula, *Nat Photon*, 2012, 6, 824-828.
39. J.-H. Yum, E. Baranoff, F. Kessler, T. Moehl, S. Ahmad, T. Bessho, A. Marchioro, E. Ghadiri, J.-E. Moser, C. Yi, M. K. Nazeeruddin and M. Grätzel, *Nat Commun*, 2012, 3, 631.
40. J. Brillet, M. Cornuz, F. Le Formal, J. H. Yum, M. Gratzel and K. Sivula, *J. Mater. Res.*, 2010, 25, 17-24.
41. X. N. Peng, C. He, X. Fan, Q. Y. Liu, J. Zhang and H. Wang, *Int. J. Hydrog. Energy*, 2014, 39, 14166-14171.
42. N. Gaillard, Y. Chang, J. Kaneshiro, A. Deangelis and E. L. Miller, *Solar Hydrogen and Nanotechnology V*, 2010, 7770, 14.
43. E. L. Miller, R. E. Rocheleau and S. Khan, *Int. J. Hydrog. Energy*, 2004, 29, 907-914.
44. E. L. Miller, B. Marsen, D. Paluselli and R. Rocheleau, *Electrochem. Solid State Lett.*, 2005, 8, A247-A249.
45. C. M. Ding, W. Qin, N. Wang, G. J. Liu, Z. L. Wang, P. L. Yan, J. Y. Shi and C. Li, *Physical Chemistry Chemical Physics*, 2014, 16, 15608-15614.
46. http://www.xunlight.com/.
47. J. Ramanujam and A. Verma, *Materials Express*, 2012, 2, 177-196.
48. H. R. Orthner and P. Roth, *Mater. Chem. Phys.*, 2003, 78, 453-458.
49. S. Saremi-Yarahmadi, K. G. U. Wijayantha, A. A. Tahir and B. Vaidhyanathan, *Journal of Physical Chemistry C*, 2009, 113, 4768-4778.
50. J. D. Desai, H. M. Pathan, S. K. Min, K. D. Jung and O. S. Joo, *Semiconductor Science and Technology*, 2005, 20, 705-709.
51. J. D. Desai, H. M. Pathan, S. K. Min, K. D. Jung and O. S. Joo, *Appl. Surf. Sci.*, 2006, 252, 2251-2258.

52. R. H. Goncalves, B. H. R. Lima and E. R. Leite, *Journal of the American Chemical Society*, 2011, 133, 6012-6019.
53. S. H. Shim and T. S. Duffy, *Am. Miner.*, 2002, 87, 318-326.
54. A. M. Jubb and H. C. Allen, *Acs Applied Materials & Interfaces*, 2010, 2, 2804-2812.
55. D. L. A. de Faria, S. Venâncio Silva and M. T. de Oliveira, *Journal of Raman Spectroscopy*, 1997, 28, 873-878.
56. N. D. Phu, D. T. Ngo, L. H. Hoang, N. H. Luong, N. Chau and N. H. Hai, *J. Phys. D-Appl. Phys.*, 2011, 44, 7.
57. A. Furlani, M. V. Russo, G. Polzonetti, K. Martin, H. H. Wang and J. R. Ferraro, *Appl. Spectrosc.*, 1990, 44, 331-334.
58. R. P. Gupta and S. K. Sen, *Physical Review B*, 1974, 10, 71-77.
59. R. P. Gupta and S. K. Sen, *Physical Review B*, 1975, 12, 15-19.
60. A. P. Grosvenor, B. A. Kobe, M. C. Biesinger and N. S. McIntyre, *Surface and Interface Analysis*, 2004, 36, 1564-1574.
61. N. S. McIntyre and D. G. Zetaruk, *Analytical Chemistry*, 1977, 49, 1521-1529.
62. A. Barrie, I. W. Drummond and Q. C. Herd, *J. Electron Spectrosc. Relat. Phenom.*, 1974, 5, 217-225.
63. T. P. Nguyen and S. Lefrant, *J. Phys.-Condes. Matter*, 1989, 1, 5197-5204.
64. G. Hollinger, *Appl. Surf. Sci.*, 1981, 8, 318-336.
65. J. A. Taylor, G. M. Lancaster, A. Ignatiev and J. W. Rabalais, *J. Chem. Phys.*, 1978, 68, 1776-1784.
66. Z. Chen, T. Deutsch, H. Dinh, K. Domen, K. Emery, A. Forman, N. Gaillard, R. Garland, C. Heske, T. Jaramillo, A. Kleiman-Shwarsctein, E. Miller, K. Takanabe and J. Turner, in *Photoelectrochemical Water Splitting*, Springer New York, 2013, DOI: 10.1007/978-1-4614-8298-7_5, ch. 5, pp. 49-62.
67. M. Cornuz, M. Gratzel and K. Sivula, *Chem. Vapor Depos.*, 2010, 16, 291-295.
68. Y. Q. Liang, C. S. Enache and R. van de Krol, *International Journal of Photoenergy*, 2008, DOI: 10.1155/2008/739864, 7.
69. A. Duret and M. Gratzel, *J. Phys. Chem. B*, 2005, 109, 17184-17191.
70. S. Gatz, H. Plagwitz, P. P. Altermatt, B. Terheiden and R. Brendel, *Appl. Phys. Lett.*, 2008, 93, 3.
71. A. T. Voutsas, M. K. Hatalis, J. Boyce and A. Chiang, *J. Appl. Phys.*, 1995, 78, 6999-7006.
72. A. Zwick and R. Carles, *Physical Review B*, 1993, 48, 6024-6032.
73. N. Beermann, L. Vayssieres, S. E. Lindquist and A. Hagfeldt, *Journal of the Electrochemical Society*, 2000, 147, 2456-2461.
74. Y. Matsumoto, T. Yoshikawa and E. Sato, *Journal of the Electrochemical Society*, 1989, 136, 1389-1391.
75. S. Kim, J. W. Chung, H. Lee, J. Park, Y. Heo and H. M. Lee, *Solar Energy Materials and Solar Cells*, 2013, 119, 26-35.
76. Z. Chen, T. Deutsch, H. Dinh, K. Domen, K. Emery, A. Forman, N. Gaillard, R. Garland, C. Heske, T. Jaramillo, A. Kleiman-Shwarsctein, E. Miller, K. Takanabe and J. Turner, in *Photoelectrochemical Water Splitting*, Springer New York, 2013, DOI: 10.1007/978-1-4614-8298-7_2, ch. 2, pp. 7-16.

4 Photocatalyst Suspensions: BP

The previous experimental chapters of this thesis explored two different types of integrated photoelectrochemical array: the water splitting photodiode and a PV-PEC tandem device. This chapter will explore the application of a relatively neglected III-V semiconductor, boron phosphide, in a photocatalyst suspension. The use of photocatalyst suspensions for water splitting provide the cheapest route due to the simplicity of the reactor design and photocatalyst synthesis. III-V semiconductors have been studied extensively for photoelectrochemical applications and currently have the highest reported water splitting efficiencies in the literature.[1] Devices are typically comprised of III-V multijunctions (e.g. GaAs, $GaInP_2$) whose band-gaps can be compositionally tuned to absorb the maximum amount of the solar spectrum. Multijunction devices were developed by the PV community and allow efficiencies of the device to exceed the Shockley-Quiesser limit for a single p-n juction system,[2] (which is ~32% for a solar cell with the optimal band gap of 1.3 eV),[3] and are ideal for water splitting due to the high V_{OC} that can be achieved. Despite the high efficiency delivered by III-V multijunction systems, their implementation is limited by prohibitively high costs of fabrication and materials, in particular the incorporation of indium ($735/ kg in 2014) in InP, $GaInP_2$ etc.[4]

The synthesis of boron phosphide will be described using metathesis of relatively inexpensive and widely available precursors, along with the material's water splitting activity. Boron phosphide is an ideal candidate for photoelectrochemical water splitting due to a band-gap of 2.0 eV which straddles the water oxidation and reduction potentials, and due the inherent stability of the material.[5] A comprehensive and up to date review of the materials synthesis and properties of boron phosphide will be given due to the scarcity of such information in the literature, however an excellent review published in 2000 in the book *'Electric Refractory Materials'* can also be referred to for further information on boron phosphide.[6]

4.1 Introduction

4.1.1 Photocatalyst Suspensions

The cheapest and most simple approach toward photo-driven water splitting is the employment of a photocatalyst suspension as described in Section 1.4.2. In this scheme semiconductor particles are dispersed in solution and are not incorporated as part of an electrode. To increase the catalytic activity of the surface, one or two co-catalysts can be loaded onto the surface of the particle, Figure 4.1.

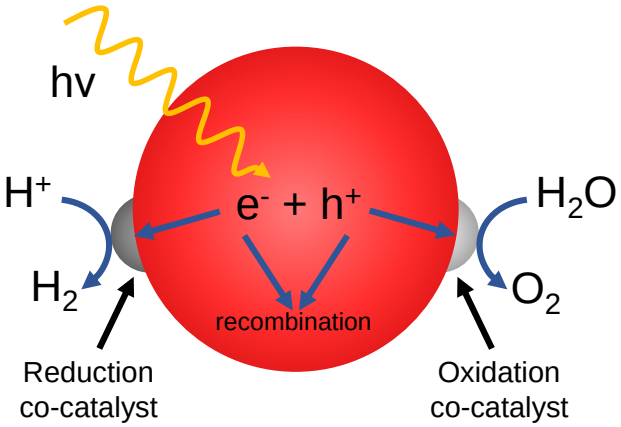

Figure 4.1 Photocatalyst particle loaded with oxidation and reduction co-catalysts

The particle size in the photocatalyst suspension is an important consideration for the overall STH efficiency of the reactor, since it affects the mechanisms by which light interacts with the particles and the overall charge transfer kinetics at the semiconductor/ electrolyte interface. Since in the case of a particle suspension, the optical path length of the semiconductor depends on the particle size, micron-sized particles are able to absorb more light than nanoparticulate materials and scatter light more effectively. Nevertheless, nanoparticles present the potential to exploit quantum size effects. First described by Brus,[7] spatial confinement of charge carriers to a volume less than their De Broglie wavelength results in a widening of the band gap. Although on first glance this band gap widening may seem undesirable for a PEC material, as a result the conduction band edge shifts positively with respect to H^+/H_2. This can decrease the required bias

potential and increase the STH efficiency of materials such Fe_2O_3, for which the conduction band is located below H^+/H_2.[8, 9]

Perhaps of greatest concern when using nanoparticulate photocatalysts is an absence of band bending at the semiconductor/ electrolyte interface. This is a result of the small number of ionised donors or acceptors and such particles cannot sustain a large built in electric field. The maximum attainable potential drop within a spherical semiconductor with radius R and a donor density N_D is given by:

$$\phi_{SC} = \frac{-eN_D R^2}{6\varepsilon_0 \varepsilon_r} \quad (4.1)$$

Since the electric field in a nanoparticle cannot play a significant role in the separation of photogenerated electrons and holes, charge transfer kinetics at the semiconductor/ electrolyte interface usually dominate the overall charge separation and recombination kinetics in nanoparticles. Fortunately, due to the small dimensions of the particles, charge-transfer pathways to the surface of the semiconductor are short and most carriers are able to reach the surface since the minority carrier diffusion length is much larger than the radius of the nanoparticle. Furthermore the large surface area per particle volume afforded by nanoparticles offers a distinct advantage over larger dimension materials and planar electrodes and lessens the co-catalyst requirement.

4.1.2 Boron Phosphide

Despite the wealth of research on the III-V semiconductor family, examples of the synthesis and characterisation of boron phosphide are amazingly scarce. Although the first report of BP was in 1891,[10] the lack of a simple synthetic technique to produce single crystals of the material, (along with complications in materials handling caused by the refractory hardness and brittleness of BP), has limited the utilisation of BP. A conventional Czochralski crystal growth method cannot be employed to form single crystals of BP as it decomposes to a lower phosphide at 1130 °C, well below the melting point of the material at 3200 °C.[11, 12]

Alternative methods to obtain single crystals of BP include flux growth of small single crystals from molten Cu or Ni, but this can lead to high levels of impurities in the

BP lattice.[13-15] Heteroepitaxy onto Si(100) substrates using CVD has also been investigated,[16] but the large lattice mismatch (16%) between Si and BP leads to a high defect density in the resultant material. Chemical vapour deposition of PX_3 and BX_3 (X = H, Cl, Br) also requires highly toxic precursors and high substrate temperatures (~900 – 1000 °C), necessitating the use of specialist equipment. [17-20]

4.1.2.1 Physical Properties of BP

Boron monophosphide, BP, is a III-V refractory semiconductor which adopts the zinc-blende structure and has a lattice parameter of 4.5383 Å,[5] (Figure 4.2). The small ionic radii and the similar electronegativity of the elements make the bonding in BP almost entirely covalent.[21] As a result BP is stabilised relative to the other III-V semiconductors and displays excellent thermal and chemical stabilities, resisting all common etchants.[22] The ionisation energy of boron, *I(B)*, strongly deviates from that of Ga and In but is quite comparable to P, leading to a small ionisation energy for boron phosphide, ΔI(BP), which is also thought to be responsible for the differences in physical properties as compared to other III-V semiconductors, some of which are displayed in Table 4.1.

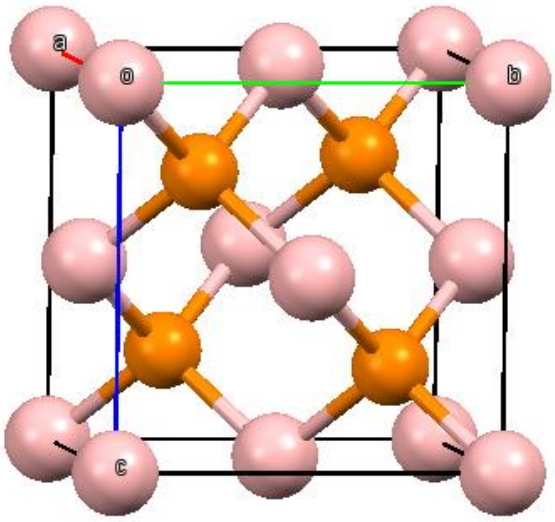

Figure 4.2 Unit cell of BP (37403-ICSD), boron = pink, phosphorus = orange

Boron phosphide is mechanically strong with a Vickers hardness similar to TiN,[5] has a high melting point of >2000 °C, (although due to a high phosphorus vapour pressure it decomposes to lower phosphide at >1100 °C),[12] and a high thermal

conductivity which has led to interest in the material for application in electronic devices in extreme environments.[23, 24]

	GaP	GaAs	InP	BP	BAs
Structure			Zinc Blende		
Space Group			F4-3m		
Lattice Constant (Å)	5.45	5.65	5.86	4.54	4.77
Density ($g.cm^{-3}$)	4.13	5.14	4.81	2.97	5.22
Mohs Hardness	5	4.5	6-7	9.5	-
Band Gap (eV)	2.26 (indirect)	1.42 (direct)	1.35 (direct)	2.0 (indirect)	1.46 (indirect)
Refractive Index	2.9	3.3	3.6	3.1	-
Electron Hall Mobility ($cm^2.V^{-1}.s^{-1}$ @298 K)	189	9340	6460	190	100-400
Hole Hall Mobility ($cm^2.V^{-1}.s^{-1}$ @298 K)	140	450	180	500	-
Thermal Conductivity *K* ($W.cm^{-1}.K^{-1}$)	0.77	0.45	0.68	3.5	2.1

Table 4.1 Physical properties of some III-V semiconductors[25-29]

Boron phosphide has an experimentally determined indirect band gap of 2.0 eV,[30-32] with direct transitions at ~5.0 eV, 6.9 eV and 8.0 eV from the reported reflectivity spectrum.[6, 33] The electronic structure of boron phosphide has been described theoretically and whilst many attempts at modelling the band gap have underestimated or overestimated the band gap,[34-37] a recent study by Ejembi et al was able to accurately model the band gap of BP using an ab-initio density functional theory calculation.[38] An indirect Γ-*X* band gap of 2.02 eV was obtained and similar to cubic diamond and silicon, the lowest conduction band for BP occurs slightly away from the X point due to its low iconicity, Figure 4.3. The various contributions of the orbitals to the valence and conduction bands were determined and it was seen that top group of the valence band is dominated by P 3p and B 2p states with minor contributions from B 2s states, whilst the bottom group of the valence band was predominantly P 2s in character. The conduction band was determined to be a hybrid of B 2p and B 3d states with contributions from P 3p states.

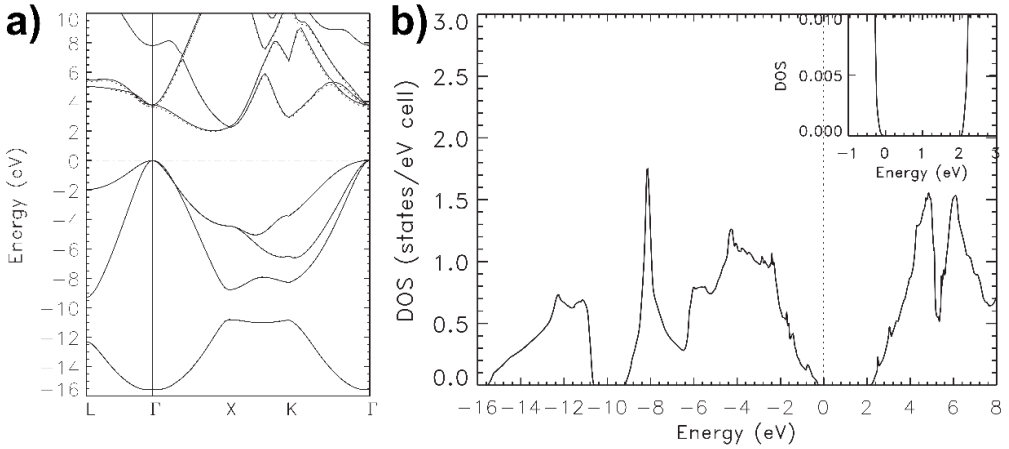

Figure 4.3 a) Electronic band structure and b) density of states of zinc-blende boron phosphide with the inset showing a calculated 2.02 eV indirect band gap. Reproduced with permission from[38]

Boron phosphide displays n-type or p-type conductivity depending on the atomic ratio of B and P; an excess of B leads to p-type conductivity and an excess of P leads to n-type conductivity.[39] Although BP has a lower electron mobility than many of the III-V semiconductors, it is thought that it could become a useful semiconductor material if controlled doping can be achieved.[6] Furthermore the charge carrier mobility of BP is far greater than commonly employed metal oxide semiconductors for water splitting, for example α-Fe_2O_3 which has electron and hole mobilities of 0.1 and 0.2 $cm^2.V^{-1}.s^{-1}$ respectively,[40] vs BP, which has electron and hole mobilities of 190 and 500 $cm^2.V^{-1}.s^{-1}$ respectively and so it is of great interest as a water splitting photocatalyst.

4.1.2.2 Boron Phosphide as a Photocalayst for Water Splitting

An interesting consequence of the small ionisation energy of boron, *I(B)*, is that the valence band of BP lies very deep in comparison to the other III-V semiconductors and is even found below the water oxidation potential at 1.23 V vs NHE, Figure 4.4. The band positions of BP were experimentally determined by Goossens and Schoonman using Mott-Schottky analysis (with an experimental accuracy of 0.05 eV) and were found to agree well with semi-empirical calculations using atomic electronegativities.[5] The band positions were found to obey the following equations:

$$E_c(BP) = (0.32 + 0.06 \,.\, pH)\ eV\ vs\ SCE$$

$$E_v(BP) = (-1.68 + 0.06 \,.\, pH)\ eV\ vs\ SCE$$

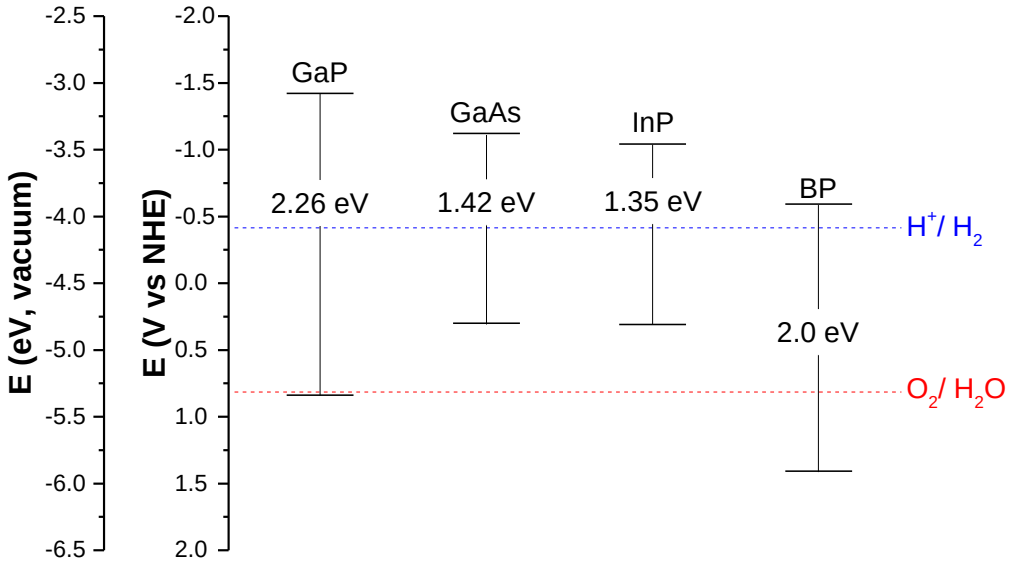

Figure 4.4 Conduction and valence band positions of some III-V semiconductors at pH = 7[5]

The theoretical ability of boron phosphide to both oxidise and reduce water, the inherent stability of the material and its band gap of 2.0 eV make BP an ideal candidate as a photoelectrochemical water splitting material. A maximum efficiency of 18 % could be obtained in a stand-alone device, (calculated from a band gap of 2.0 eV and assuming all solar photons are captured and converted without additional loss),[41, 42] exceeding the DOE 2015 target for a single material efficiency of 15 %.[43]

Boron phosphide was first investigated for use in a photoelectrochemical cell in 1979 (seven years after Honda and Fujishima's seminal paper on TiO_2 photoelectrolysis[44]) by Grantham, who patented a system utilising a BP photoelectrode submerged in an HBr electrolyte.[45] Although a BP-only photoelectrode was not fabricated as suggested in the patent, as proof of concept, an electrode consisting of a BP layer coated onto a GaAs substrate was operated galvanostatically (100 $mA.cm^{-2}$) in a 48% HBr electrolyte at 50 °C for 100 hours under 3 sun illumination with no signs of corrosion, though it was not stated how this was determined.

Honda and Fujishima later investigated the photoelectrochemical properties of a p-type single crystal of BP prepared using the flux method[14] in acidic solution.[46] Promising photocurrents of 14.4 $mA.cm^{-2}$ at -1 V vs SCE were markedly improved to 30.1 $mA.cm^{-2}$ at -1 V vs SCE on treatment of the electrode surface with a 3% ruthenium (III) chloride solution. The electrodes were stable under operation for 8 hours in 0.5 M H_2SO_4 with no evidence of deterioration. Action spectra of the p-BP electrodes showed

a threshold in the photocurrent response at 600 nm, agreeing with the 2.0 eV band gap known for BP. A 2-electrode cell was constructed incorporating a platinum counter electrode and a short-circuit current density of 2.4 mA.cm^{-2}, open circuit photovoltage of 0.45 V and a fill factor of 0.25 was observed. It was concluded that despite the desirable photoresponse and excellent stability of the BP electrodes, the overall conversion efficiency was too low to be of use in a practical device and further optimisation was needed.

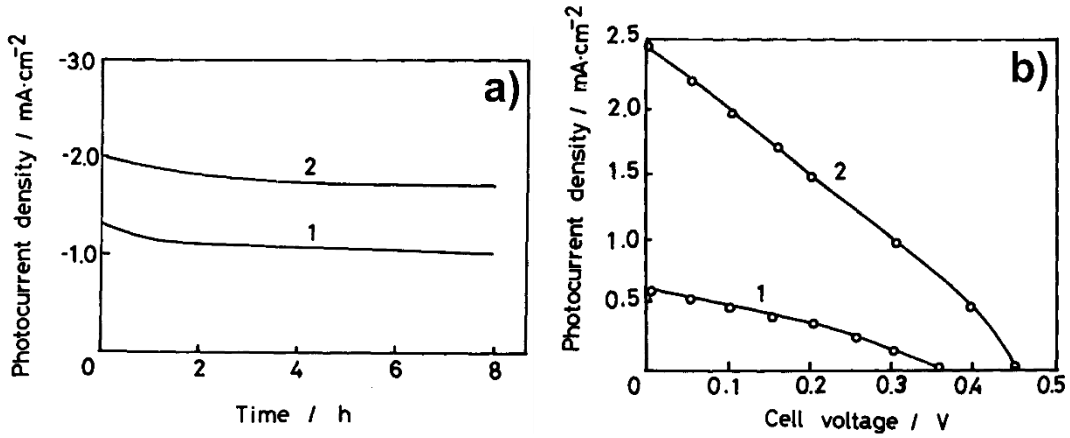

Figure 4.5 Photoelectrochemical characterisation of single crystal *p*-BP electrodes in 0.5 M H_2SO_4 under 500 W Xe irradiation where (1) = bare etched BP and (2) = etched BP treated with 3% $RuCl_3$ solution. a) Chronoamperometry of BP single crystal electrodes -0.4 V vs SCE and b) photocurrent-photovoltage characteristics of the cell Pt(H_2) /H_2SO_4 / /H_2SO_4 /p-BP[46]

Thin films of polycrystalline BP were investigated by Goossens et al, who carried out thermal CVD of PBr_3 and BBr_3 in a hydrogen atmosphere onto alumina substrates. The black films showed n-type conductivity with low resistivity and high donor density. Auger analysis showed no other elements but B and P were present and so it was concluded an excess of P was responsible for conduction in the layers. Photoelectrochemical measurements were carried out in 0.1 M H_2SO_4 under irradiation with a 450 W Xe lamp and maximum photocurrents of 0.5 mA.cm^{-2} were observed, with onset potentials varying between 0.1 and 0.5 V vs SCE depending on the sample. The poor photocurrent response was attributed to a high density of surface states, the presence of which were confirmed using transient measurements.[18] A substantial photocurrent was observable at subbandgap illumination, suggesting the presence of intragap states.

In order to improve the quality of the deposited BP film, heteroepitaxy onto a suitable substrate can be employed. In particular Si has attracted attention, as despite the large lattice mismatch (5.43 Å for Si vs 4.54 Å for BP), BP can be deposited epitaxially onto Si(100).[16, 47] The large difference between the lattice parameters induces stress in the interfacial region which is relaxed by twinning of the BP lattice,[48] and so the use of alternative substrates with better matched lattice parameters (such as SiC[49] or GaN[50]) may further improve the quality of the deposited BP films.

Degenerate n-Si/n-BP and non-degenerate p-Si/n-BP electrodes have been investigated for photoelectrochemical applications. Butler and Ginley deposited degenerate single crystalline n-type BP as a protective window material on n-type Si. The heterojunction n-Si/n-BP cells displayed excellent stability where $>10^4$ coulombs charge were passed through the cells without significant loss of efficiency, as compared to pristine Si where the current degraded to 0 after only 0.8 coulombs of charge was applied. Despite the excellent stability, the cells had poor efficiency values with nearly linear I-V curves and very low fill factors.[51]

Goossens et al compared n-Si/n-BP and p-Si/n-BP electrodes,[39, 52] and observed very different behaviour for the two types of heterojunction. The n-Si/n-BP electrodes produced small anodic photocurrents on the order of $\mu A.cm^{-2}$ with a photocurrent threshold of 2.0 eV, whereas the p-Si/n-BP electrodes produced large cathodic currents on the order of 10 $mA.cm^{-2}$ with a photocurrent threshold of 1.1 eV, Figure 4.6.

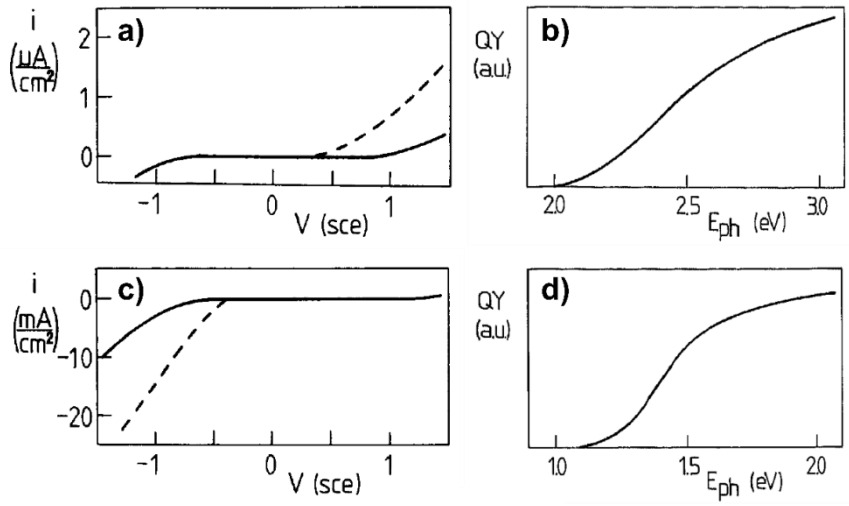

Figure 4.6 Current-voltage characteristics of a) n-Si/n-BP and b) p-Si/n-BP. The solid line corresponds to the dark photocurrent and the dashed the combined dark and light photocurrent. Reproduced with permission from[39]

The different behaviour of the n-Si/n-BP and p-Si/n-BP electrodes was accounted for by the band structure of the heterojunction. The conduction band of Si matches the conduction band of BP excellently, allowing conduction band electrons to pass easily through the Si/BP junction. However, the valence bands of Si and BP differ considerably. Valence band holes in Si face a 0.9 eV potential barrier at the Si/BP junction and recombine with electrons instead of crossing. The band structures of the n-Si/n-BP and p-Si/n-BP heterojunction configurations are presented in Figure 4.7.

When n-Si is used as the photoanode, photoholes in Si recombine at the n-Si/n-BP heterojunction with electrons from the BP conduction band converting energy from the photoexcitation into heat and decreasing the efficiency of the cell dramatically. However when p-Si is used as the photocathode, Si photoelectrons cross the p-Si/n-BP interface and drive the reduction reaction at the semiconductor electrolyte interface. The photoholes generated in BP are so few in number with respect to the numerous conduction band electrons that recombination is likely to take place before they reach the electrolyte.

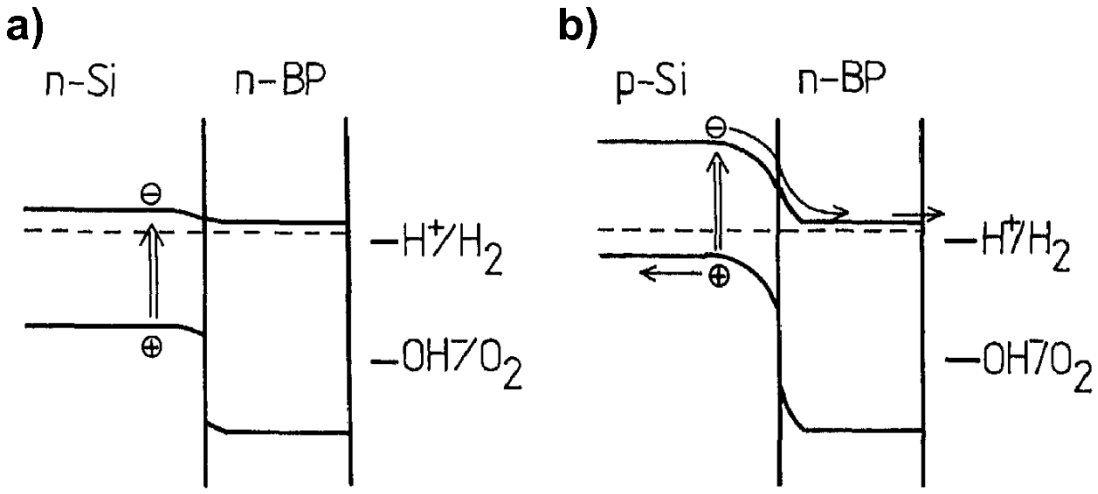

Figure 4.7 Band diagrams of degenerate n/n and non-degenerate p/n Si/BP junctions. Reproduced with permission from[52]

The p-Si/n-BP heterojunction photoelectrodes were operated under short-circuit conditions (Pt counterelectrode) in 1 M H_2SO_4 at -2 V (about -1.5 V vs SCE) under 100 $mW.cm^{-2}$ tungsten lamp irradiation. A photocurrent of 10 $mA.cm^{-2}$ was obtained and was stable for 1000 hours, when the experiment was terminated. At the end of the

experiment it was noted that a transparent conducting layer of hexagonal B_2O_3 had formed on the surface of the electrode.

It was observed that upon applying an external voltage, the bands in BP at the BP/electrolyte interface are bent but the electric field at the Si/BP junction is not influenced by external applied potential differences. When the potential barrier for the conduction band electrons in BP is absent or small, a cathodic reduction can occur. The necessary bias can be provided by a suitable redox electrolyte and a V^{2+}/V^{3+} redox couple was selected due to the -0.35 V vs SCE potential provided. Despite the large optical absorption of this electrolyte, a maximum short circuit current of 15 $mA.cm^{-2}$ was obtained with 80 $mW.cm^{-2}$ irradiation power. The open circuit potential was about 0.5 V and the fill factor was 0.5, yielding a conversion efficiency of 4-5%, greatly improved as compared to those of fluxed BP crystals.

Boron phosphide has also been investigated for use in a 'Gratzel' type photoelectrochemical cell, whereby a senisitizer is applied to a large surface area wide-gap semiconductor to maximise absorption.[53] Schroten et al deposited BP<111> whiskers (50-100 nm diameter) onto a graphite substrate using the vapour-liquid-solid (VLS) CVD technique employing a nickel catalyst.[54] They found that amorphous B_xP (B>3) could be applied *in-situ* as a sensitizer by simply altering the growth conditions once the BP nanowires had formed. The optical properties of the amorphous B_xP were investigated and with increasing boron content, a lowering of the band gap was observed. Photocurrent action spectra of BP whisker films on graphite showed a threshold of 2.0 eV, concordant to the optical bandgap of BP. When amorphous B_xP was applied to the whiskers, photocurrents at photon energies down to 1.5 eV were observed, demonstrating the sensitization principle of BP whiskers with amorphous BP. Although the sensitivity of the cell was extended to 1.5 eV, the photocurrent at photon energies above 2.1 eV dropped considerably due to a rise in internal resistance of the electrode and to electron-hole recombination at the BP/B_xP or B_xP/electrolyte interfaces. External quantum efficiencies were very low (3×10^{-3}) but the study remains interesting as a proof of principle in the use of amorphous B_xP as a sensitizer.

4.1.3 Synthesis of Boron Phosphide

4.1.3.1 Boron Phosphide Powder Synthesis

Ideally an inexpensive and scalable technique to synthesise BP in large quantities is required if the material is to be used for practical applications such as water splitting. The production of BP as a powder offers an interesting route to the photoactive material because inexpensive and low toxicity precursors can be used. The powder can then be employed in a particle suspension reactor, the lowest cost scheme for water splitting, as described in 1.4.2.[55] A number of routes to produce powder BP are displayed in Table 4.2 and will be discussed in detail.

	Reaction	T (°C)	Duration	Ref
(1)	$B + P \rightarrow BP$	1000	3 days	56
(2)	$PCl_3 + B + 3\ Na \rightarrow BP + 3\ NaCl$	350	10 hours	57
(3)	$PCl_3 + BBr_3 + 6\ Na \rightarrow BP + 3\ NaCl + 3\ NaBr$	300	12 hours	58
(4)	$PCl_3 + NaBH_4 \rightarrow BP + NaCl + 2\ HCl + H_2$	600	>6 hours	59
(5)	$PCl_3 + NaBF_4 + 6\ Na \rightarrow BP + 3\ NaCl + 4\ NaF$	400	6 hours	60
(6)	$BPO_4 + 4\ Mg \rightarrow BP + 4\ MgO$	>725	20-30 s	61

Table 4.2 Some reaction schemes to produce BP

In early studies BP was produced as a powder by direct interaction of the elements at high temperature,[12, 56, 62] however it could take up to 3 days at 1000 °C for the reaction to reach completion. More recently a low-temperature solvothermal route to produce nanocrystalline BP has been developed by Gu and co-workers.[57, 58] A boron source (B or BBr_3) was reacted with PCl_3 and an alkali metal in benzene solvent. Reactions were carried out in a sealed autoclave at temperatures between 300 and 350 °C but it was observed that materials were highly contaminated from carbonization of the benzene solvent.

Chen and co-workers were able to avoid C-contamination of BP by reacting PCl_3 with an excess of $NaBH_4$ at elevated temperatures (600 °C) in a sealed autoclave.[59] Uniformly sized nanoparticles of ~10 nm were obtained at temperatures greater than 550 °C and when $NaBH_4$ was in excess. An estimated pressure of 15 MPa was reached

in the autoclave during the reaction due to the vaporisation of PCl_3 and formation of H_2 during the decomposition of $NaBH_4$, which was stipulated to be an important factor in the formation of crystalline BP.

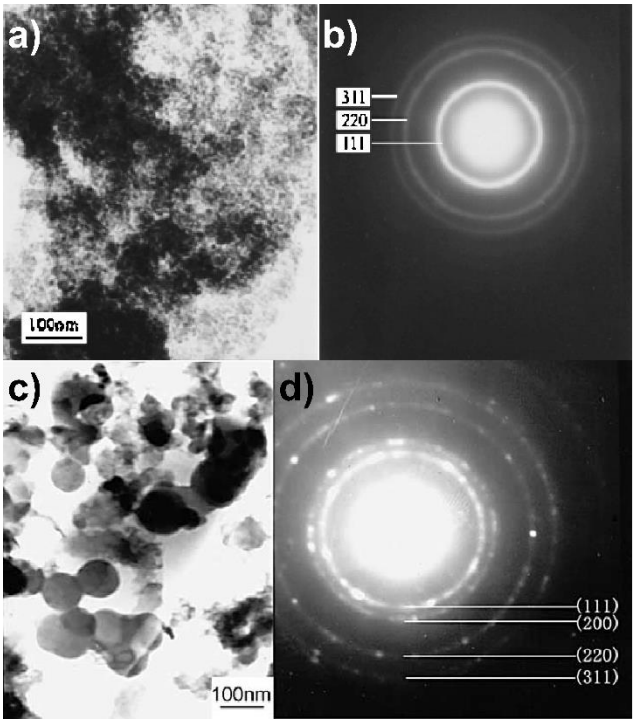

Figure 4.8 TEM images and the corresponding diffraction patterns of nanocrystalline BP produced by the reaction of PCl_3 with a) and b)[59] $NaBH_4$ and c) and d)[60] $NaBF_4$. In c) molten Na was used as an additional reductant which is thought to lead to the larger particle size. Reproduced with permission from and

Feng and co-workers used a similar reaction scheme but were able to avoid the potentially dangerous formation of hydrogen at elevated temperatures and pressures by reacting PCl_3 with $NaBF_4$ and a large excess of sodium.[60] The use of $NaBF_4$ as opposed to $NaBH_4$ also meant reactions were able to be carried under milder conditions (400 °C) due to the lower decomposition temperature of $NaBF_4$ vs $NaBH_4$ (384 vs 497 °C).[63] The authors proposed that the reaction proceeded *via* a co-reduction reaction of PCl_3 and BF_3 (produced from the decomposition of $NaBF_4$) at the liquid: Na interface. A mixture of spherical particles and 'worm-like' nanorods about 60-90 nm in dimension were obtained; much larger than the particles produced by Chen an co-workers likely due to higher rates of growth and lower rates of nucleation at the liquid Na surface.

A self-propagating high-temperature method of producing submicron BP powders was demonstrated recently by Mukhanov and co-workers, who pressed pellets

of a mixture of boron phosphate and magnesium and initiated the reaction by heating the pellet to ~1000 K with a gas flame.[61] During the reaction temperatures exceeding 1500 K were reached, leading to the partial decomposition of BP to B_2P_{12} (in concentrations of up to 30%). Sodium chloride was added as an inert diluent to reduce the temperature of the reaction front after, which a 98% ratio of BP to B_2P_{12} was achieved. After washing of the products to remove NaCl and a further heat treatment, polycrystalline 'bulks' of BP were obtained with a grain size of around 5-10 μm and a Vickers hardness approaching that of BP single crystals.

A method of producing size-controlled boron phosphide nanocrystals by the reduction of boron phosphate in a borophosphosilicate glass (BPSG) matrix was developed recently by Sugimoto and co-workers.[64] Boron phosphate and silicon were placed onto an SiO_2 target and co-sputtered onto a stainless steel substrate to give a film comprised of a mixture of Si, B, P and O. The films were then exfoliated from the substrate and annealed under nitrogen to form BP nanocrystals suspended in a BPSG matrix. The matrix could be dissolved in HF to leave the nanocrystals in suspension, which were sized between ~2-6 nm (determined by the ratio of BPO_4 sputtered into the film), Figure 4.9.

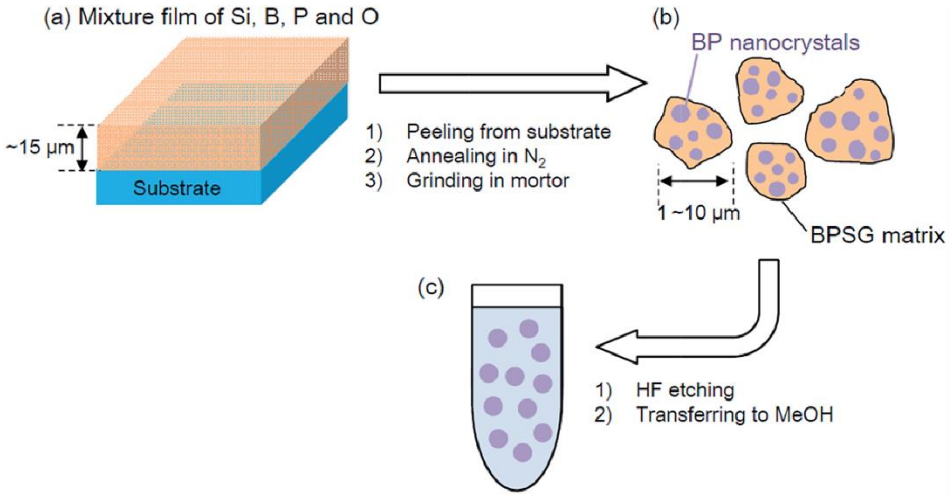

Figure 4.9 Synthesis of BP nanocrystals using boron phosphate reduction in a borophosphosilicate glass matrix. Reproduced with permission from[64]

Despite the small particle size afforded by the BPSG matrix approach, this example is not very scalable due to the expensive sputtering process utilised. The authors suggested an alternative route employing the reduction of H_3BO_3 and H_3PO_4 by hydrogen

silsesquioxane, however this technique must be optimised: in previous studies a large excess of Si was present resulting in heavily doped B and P Si nanoparticles.[65]

4.2 Experimental Methods

Preparation of BP powders: Boron phosphide powders were synthesised in sealed quartz ampoules using two different reaction schemes. To prevent oxidation of the boron phosphide product, reactions were carried out under vacuum following three nitrogen purges on a Schlenk line. Briefly, reactants were ground together in an agate mortar and loaded into quartz ampoules using a long-necked powder funnel. A Schlenk attachment was fit to the ampoules and following three nitrogen purges, ampoules were placed under vacuum and removed from the Schlenk line. Ampoules were sealed using a glass blowing torch, ensuring the reactants were well away from the heat source to avoid melting. Finally, the ampoules were placed into a muffle furnace and heated for 12 hours, Figure 4.10. In order to open the ampoules, a score was made at the middle point of the ampoule using a tungsten carbide knife. The ampoule was then snapped in half in a fume hood and the products treated according to the reaction.

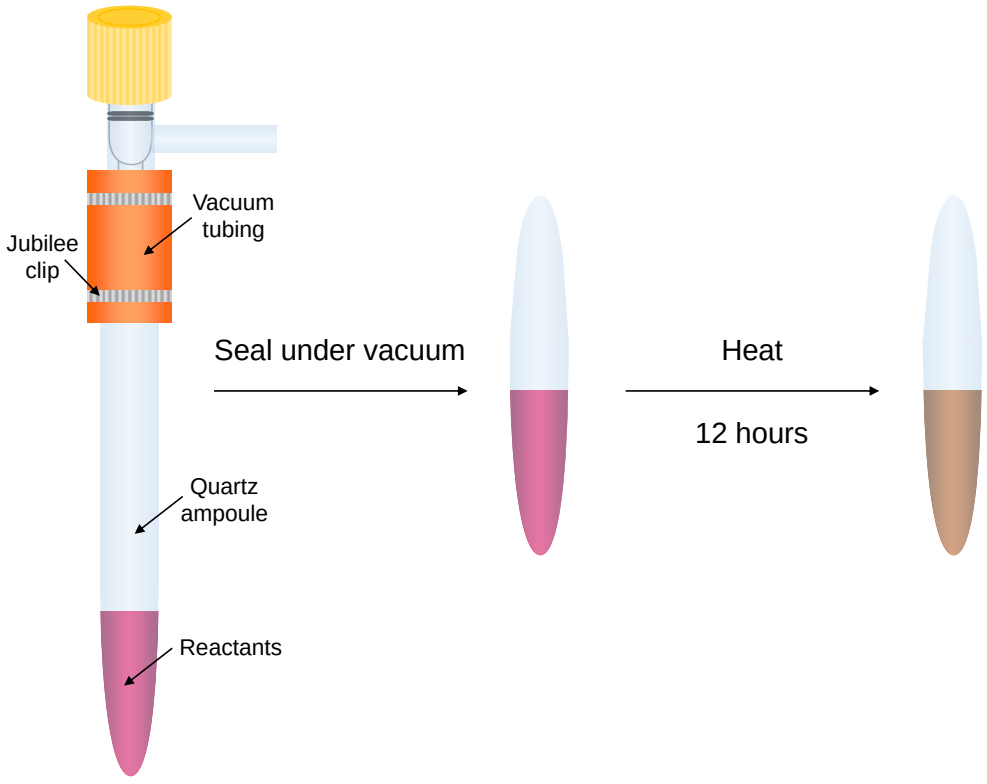

Figure 4.10 Ampoule fabricating procedure

In the first reaction scheme, the elements were simply combined and heated in a sealed quartz ampoule. 0.07 g, 6 x 10^{-3} moles boron (B, > 95%), purchased from Fluka, and a slight excess of red phosphorus 0.28 g, 9 x 10^{-3} moles (P, >95 %), purchased from BDH, were ground together and sealed in a quartz ampoule. The ampoule was placed in a furnace and heated at a rate of 10 °C/ min to 1000 °C, where is was held for 12 hours before switching the furnace off and cooling to room temperature. The brown product was recovered from the ampoule and analysed without any further processing.

In the second reaction scheme, a metathesis reaction of boron triiodide (BI_3, 95 %) and calcium phosphide (Ca_3P_2, 99%), was used, both purchased from Sigma Aldrich. CAUTION: calcium phosphide is highly moisture sensitive and liberates phosphine gas on contact with air which can ignite spontaneously. Metathesis reactions were carried out in sealed quartz ampoules, which had been prepared in a glove box. Firstly, 1.67 g of BI_3, (4.3 x 10^{-3} moles) was ground together with 0.39 g of Ca_3P_2 (2.13 x 10^{-3} moles) and loaded into a quartz ampoule. A Schlenk attachment was fit to the ampoule which was closed and brought out of the glove box to be attached to a Schlenk line. The ampoule was then sealed, placed into a furnace and heated at a rate of 10 °C/ min to 700 °C, where is was held for 12 hours before switching the furnace off and cooling to room temperature. The ampoule was opened in a fume hood to prevent inhalation of phosphine gas from any unreacted calcium phosphide. A fine brown powder was recovered from the ampoule and washed with 3 x 50 ml of deionised water. In order to retrieve the product between washes, centrifugation was used as the fine powder tended to become stuck in filter paper. Finally, the powder was freeze-dried to remove the water and avoid excessive heating of the material. The wet slurry was frozen with liquid nitrogen and placed in a freeze drier for ~ 24 hours. The dried product was weighed a yield of 130 mg, 72 %, was obtained.

Characterisation and analysis: To confirm the phase of the material made, powder X-ray diffraction was carried out. A Bruker D4 Bragg-Brentano theta-2-theta reflection geometry instrument with a Cu $K_{\alpha 1+2}$ source powered at 40 kV, 30 mA coupled with a post-sample graphite monochromator and scintillation counter detector was used. X-ray photoelectron spectroscopy (XPS) was used to determine the composition of the powder. Spectra were recorded on a Thermoscientific K-alpha spectrometer equipped with a monochromated Al K_α X-ray source and 180° double

focussing hemispherical analyser-128-channel detector. Survey spectra were recorded with energy of 200 eV and higher resolution spectra were recorded at 50 eV.

The powders were imaged using a JEOL 2100 HRTEM with a LaB_6 source at an acceleration voltage of 200 kV. The instrument was fit wit with an Oxford Instruments X-Max EDS detector. Micrographs were taken on a Gatan Orius CCD. Samples were prepared by drop-casting a suspension of the powder in ethanol solvent onto a 400 Cu mesh lacy carbon film TEM grid (Agar Scientific Ltd).

UV-vis spectra were obtained by loading the BP powder onto a microscope slide using a thin layer of vacuum grease. Spectra were recorded on a PerkinElmer Lambda 950 spectrometer in reflectance mode.

Functional testing: The ability of the powder to produce hydrogen was tested in 50 mL of a stirred sacrificial solution of 1:1 water : absolute ethanol. The ethanol was used as a hole scavenger and the remaining photogenerated electrons performed the reduction reaction. 0.1 g of powder was dispersed in solution in a sealed glass vessel equipped with a water cooled jacket and which was filled with 50 mL of sacrificial solution leaving a headspace of 15 mL. A 75 W xenon arc lamp equipped with an AM1.5G filter to simulate the sun's spectral output with an irradiance of 300 $mW.cm^{-2}$ was used to irradiate the powders. 250 μL of gas was collected from the headspace every 15 minutes for two hours and analysed using gas chromatography. In order to quantify the amount of hydrogen present, the counts were compared to a sample of pure hydrogen.

4.3 Results and Discussion

4.3.1 Physical Characterisation

Despite a wealth of literature on the synthesis of the III-V compounds, examples of synthetic techniques for the production of the lightest III-V phosphide compound, boron phosphide are relatively rare. In preliminary experiments, CVD depositions of BP using APCVD of boron tribromide, BBr_3 and triphenylphosphine, PPh_3 were attempted with little success. This is most likely due to the limitations of the reactor design utilised, in which a maximum temperature of 650 °C can be achieved. Other authors have obtained similar findings and it is thought that to deposit films of boron phosphide, temperatures in excess of 1000 °C are required.[66] As a result, two techniques were used to synthesise powders of boron phosphide. In the first, which had been adapted from the literature,[56, 67] the elements were simply combined and heated at 1000 °C for 12 hours:

$$B + P \rightarrow BP \tag{4.2}$$

A brown powder was recovered and analysed using powder X-ray diffraction. Although the desired phase of cubic boron phosphide was obtained, the presence of boron phosphate was also detected, along with peaks attributable to unreacted boron and unreacted phosphorus, Figure 4.11.

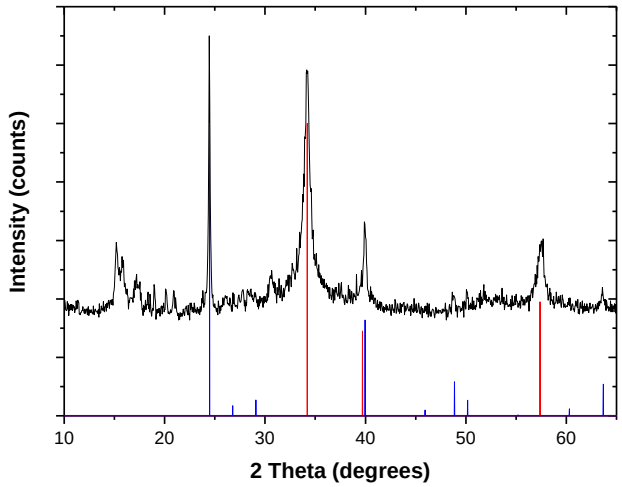

Figure 4.11 PXRD pattern of boron phosphide powder synthesised from the elements, where the measured pattern is shown in black. Standard diffraction peaks have also been included where red is boron phosphide (BP, 37403-ICSD) and blue is boron phosphate (BPO_4, 55083-ICSD)

The boron phosphate detected may indicate that the red phosphorus starting material used had become partially oxidised to phosphoric acid due to prolonged periods of storage,[68] or that some oxygen from the air was present during the reaction, despite the ampoule being sealed under vacuum following three nitrogen purges. Peaks which can be assigned to unreacted boron and phosphorus indicate the reaction had not yet reached completion (which according to the literature can take up to 3 days).[56] Separation of the BP product from these impurities is not trivial, especially boron, which is highly chemically inert.[69] Furthermore due to the long annealing step required for the reaction of B and P, the fabrication of BP using this technique is highly energy intensive process. As a result, an alternative reaction to synthesise BP was sought.

A metathesis reaction between boron triiodide and calcium phosphide (both selected for their availability and relative ease of handling) was carried out, which has not been reported in the literature before. Ampoules were prepared in a glove box before sealing under vacuum and were then heated to 700 °C for 12 hours:

$$2BI_3 + Ca_3P_2 \rightarrow 2\ BP + 3\ CaI_2 \qquad (4.3)$$

A fine brown powder was obtained, Figure 4.12, which was washed with water to remove the calcium iodide. After drying, the powder was analysed using PXRD which showed cubic boron phosphide was obtained, with no additional products detected, Figure 4.13.

Figure 4.12 Brown powder obtained from the metathesis reaction of BI_3 and Ca_3P_2

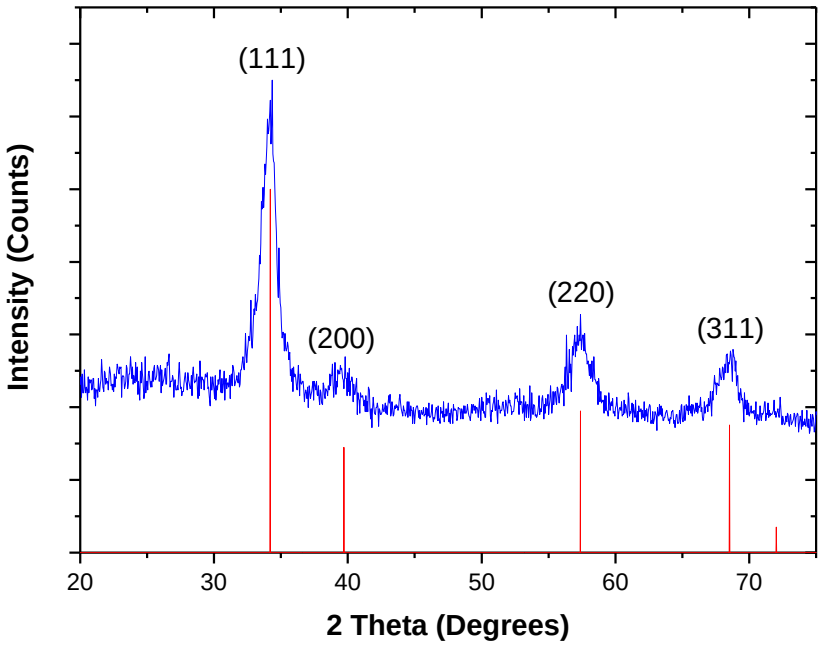

Figure 4.13 PXRD pattern of boron phosphide powder synthesised using a metathesis reaction, where the measured pattern is shown in blue. Standard diffraction peaks have also been included for boron phosphide (BP, 37403-ICSD)

The lattice parameters of the BP powder were calculated using the general structural analysis system (GSAS), where the pattern was fit employing a Reitveld model. A lattice parameter of a = b =c = 4.55 ± 0.001 Å was obtained, which compares well to values reported in the literature of 4.54 Å.[56] A unit cell volume of 94.16 $Å^3$ was calculated.

The crystallite size of the powder was estimated from the broadening of the BP (111) peak using the Scherrer Equation, (2.3),[70, 71] giving crystallite size of ~5 nm. TEM

images of the powder agreed well with the particle size calculated from the PXRD pattern, where individual particles of around 5 nm were observed, Figure 4.14. The selected area electron diffraction (SAED) pattern is also shown in Figure 4.14 and the diffraction rings from inner to outer show d spacings of 2.60, 1.64, and 1.38 Å and match BP (111), (220), and (311) planes respectively. The (200) reflection is not clearly observable in the SAED pattern due to coalescence with the intense (111) reflection. The broadening of the reciprocal lattice points and coalescence of the (111) and (200) reflections is due to the small crystallite size of the BP powder.[72]

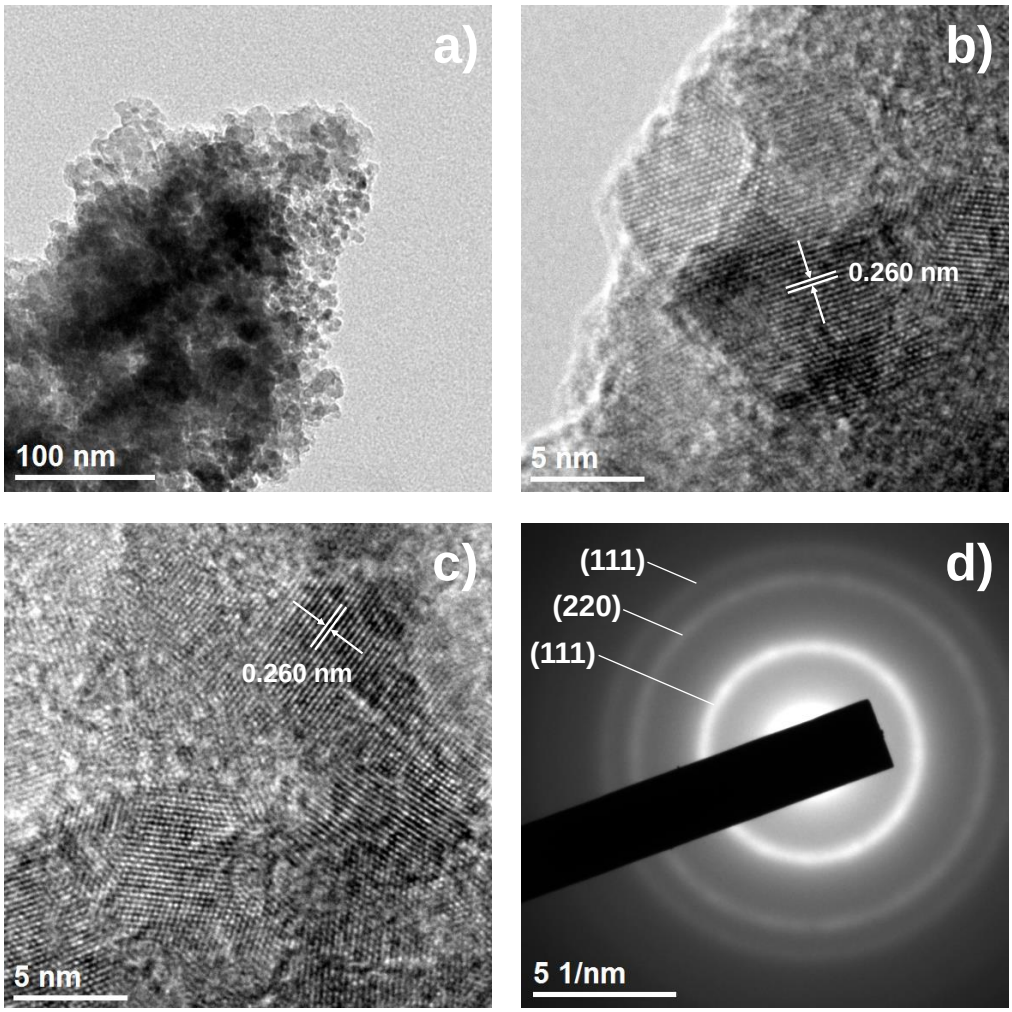

Figure 4.14 a) TEM, b) and c) HRTEM and d) SAED of BP powder synthesised using metathesis

The BP powder was analysed using XPS to determine the chemical environment and ratio of B:P. Survey spectra confirmed the presence of B and P, as well as adventitious carbon and oxygen. Two peaks were observable in the O 1s region, one at

a binding energy of 533.5 eV which can be attributed to oxygen arising from adventitious organic material,[73] and one at a binding energy of 531.0 eV which is likely due to a surface oxide on the BP. The $2p_{3/2}$ and $2p_{1/2}$ peaks were fit with a splitting of 0.86 eV,[74, 75] and modelled using a mixed Gaussian-Lorentzian function, Figure 4.15a. The predominant P 2p peaks were located at binding energies of $2p_{3/2}$ = 130.5 eV and $2p_{1/2}$ = 131.4 eV, matching values reported in the literature for BP well.[57, 76] A second set of 2p peaks at higher binding energies of P $2p_{3/2}$ = 133.0 eV and $2p_{1/2}$ = 133.9 eV were observable in much smaller quantity, with an area ratio of around 1:10 as compared to the P phosphide peak. This can be attributed to a surface oxide. Fitting of the B 1 s peak in BP is complicated by the presence of the P 2s peak in the same region, a fact almost universally overlooked in the literature where a single broad peak is ascribed to B 1s.[58-60, 77] The peaks were fit by determining the ratio of the P 2p and P 2s peaks to one another from the relative sensitivity factors to estimate the area of the P 2s peak. Four peaks were found in the region, two at lower binding energy associated with the phosphide P 2s and B 1s peaks and two smaller area peaks at higher binding energy associated with P 2s and B1s surface oxide peaks, Figure 4.15b. The P2s phosphide peak was assigned as the peak at 188.3 eV and the B1s as thee peak at 189.2 eV by the relative areas and by comparison to compounds of similar chemical environments.[78, 79] For the BP, a ratio of 1:1 B:P was calculated from the areas of the B1s and P2p peaks.

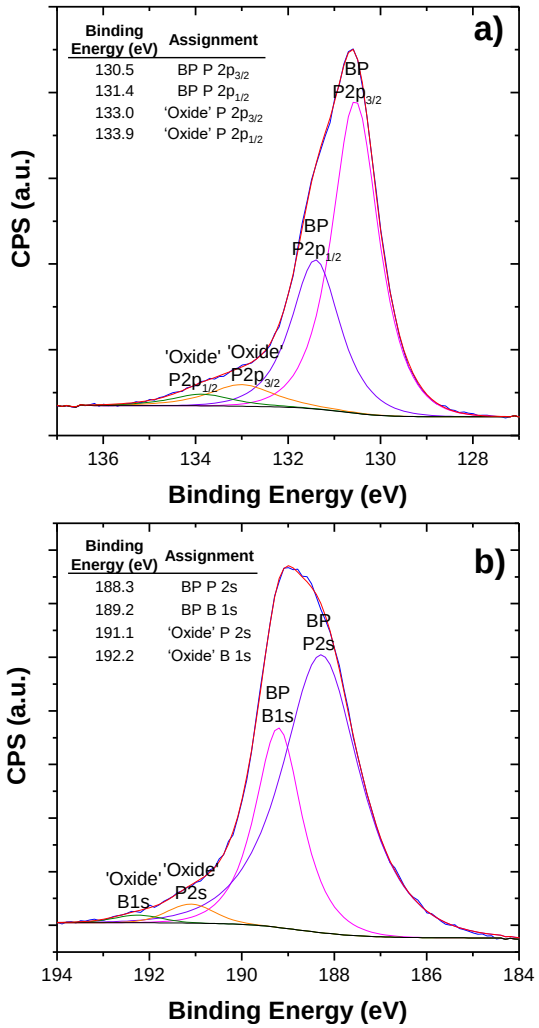

Figure 4.15 XPS spectra of boron phosphide powder synthesised using a metathesis reaction showing a) the P 2p envelope and b) the B 1s envelope

UV-vis spectra were obtained by loading the powder onto a glass slide and measuring the reflectance of the sample. As transmission in solid powder samples is very low, the actual absorption coefficient cannot be measured directly. The Kubelka Munk remission function $F(R)$ is used to represent the absorption coefficient α, and is calculated from the reflectance of the solid sample, with s the scattering coefficient.

$$F(R) = \frac{(1-R)^2}{2R} = \frac{\alpha}{s} \tag{4.4}$$

Assuming the scattering coefficient s is constant across the given wavelength range, the function *F*(R) is proportional to the absorption coefficient α, and so can represent the absorbance of the solid sample, Figure 4.16.

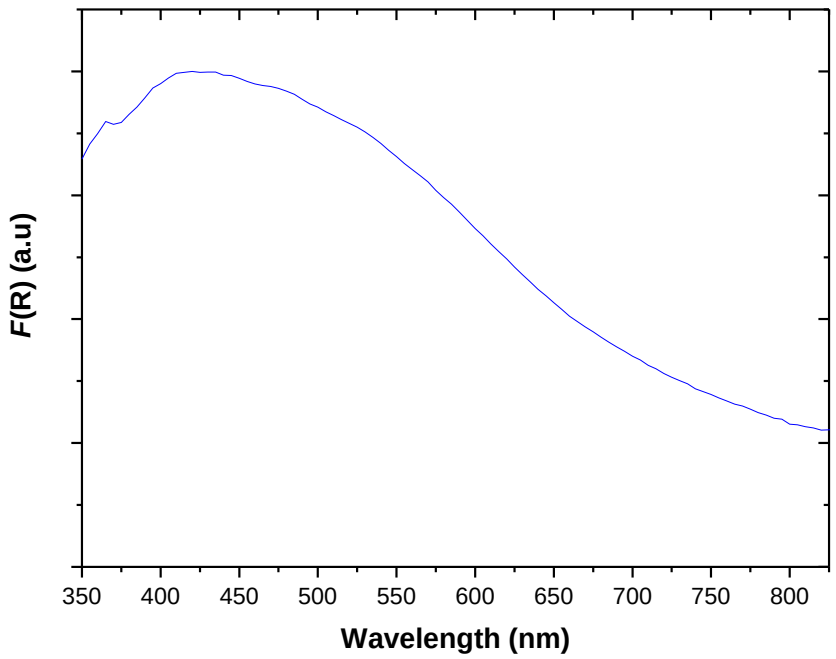

Figure 4.16 UV-vis absorbance spectra (converted from diffuse reflectance spectra) for BP powder

The UV-vis spectrum of the BP powder showed a broad absorption in the visible region agreeing with the material's brown colour.

4.3.2 Photocatalytic Water Reduction

The ability of the BP powder to reduce water at neutral pH was tested by dispersing 100 mg powder in a sacrificial solution of 1:1 water: ethanol, where ethanol acts as a hole scavenger. Prior to switching the light on, the powder was held in the dark for one hour with no H_2 production observed. The powder was then irradiated with AM1.5 light at 3 sun intensity for a duration of 4 hours and the gas produced analysed using gas chromatography, Figure 4.17.

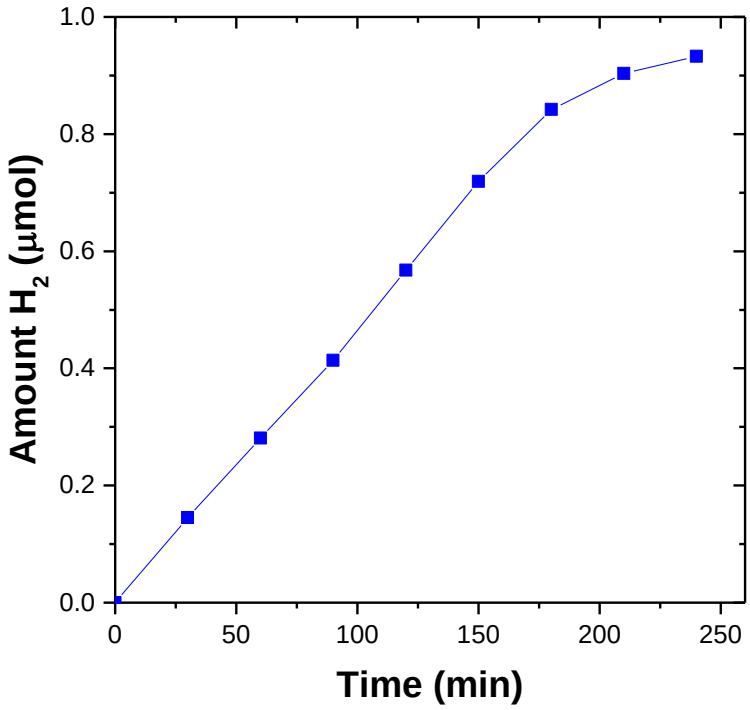

Figure 4.17 18 Photocatalytic production of hydrogen by boron phosphide powder in acidified sacrificial solution and AM1.5 irradiation of 3 sun intensity

For the first 3 hours, a steady hydrogen production rate of ~70 μL.g^{-1}.hr^{-1} was observed, which decayed to ~55 μL.g^{-1}.hr^{-1} in the final hour of testing. This decrease in photoactivity could be due to one of two factors, either to an inherent instability of the BP material as observed in the III-Vs in general,[80] or to the nanoparticulate scale of the BP powder. Nanoparticulate catalysts have a higher surface energy than bulk materials which can reduce their lifetime as catalysts.[81] It is likely that the small size of the particle and high surface energy plays a larger role in the chemical instability of the material in this instance, as BP is known to have excellent chemical stability and has been shown to be stable under photoelectrochemical testing conditions previously.[46] This rate of hydrogen production is comparable to similar systems in the literature, for example GaP nanorods grown using a solution-liquid-solid technique, for which a hydrogen production rate of ~200 μL.g^{-1}.hr^{-1} were observed under visible light illumination in a water methanol solution,[82] and a suspension of InP powder in 0.5 M Na_2SO_3, for which a hydrogen evolution rate of 30 μL.g^{-1}.hr^{-1} under 250 W high pressure Hg lamp irradiation.[83]

4.4 Conclusions

Powders of boron phosphide were synthesised using a metathesis reaction of boron triiiodide and calcium phosphide, both selected for their relative ease of handling. The powders were confirmed to be cubic BP from PXRD and a particle size of 5 nm was calculated. XPS spectra of the powders showed a 1:1 ratio of B:P and the presence of a surface oxide was also observed. In photocatalytic tests, the BP powder showed an initial hydrogen production rate of ~70 $\mu L.g^{-1}.hr^{-1}$, which decayed to 56 $\mu L.g^{-1}.hr^{-1}$ in the final hour of testing. The decrease in hydrogen production rate was thought to be attributable to the small particle size rather than an inherent instability of the BP material.

This preliminary study has shown the promise of BP as a water splitting material however further development of the synthetic technique to produce BP is required as well as further study into the inherent properties of the material.

4.5 References

1. O. Khaselev and J. A. Turner, *Science*, 1998, 280, 425-427.
2. W. Shockley and H. J. Queisser, *J. Appl. Phys.*, 1961, 32, 510-&.
3. C. A. Nelson, N. R. Monahan and X. Y. Zhu, *Energy Environ. Sci.*, 2013, 6, 3508-3519.
4. A. C. Tolcin, in *Mineral Commodity Summaries 2015*, ed. U. G. Society, 2014, p. 2.
5. A. Goossens and J. Schoonman, *Journal of the Electrochemical Society*, 1992, 139, 893-900.
6. K. Yukinobu, in *Electric Refractory Materials*, CRC Press, 2000, DOI: doi:10.1201/9780203908181.ch22 10.1201/9780203908181.ch22.
7. L. E. Brus, *J. Chem. Phys.*, 1984, 80, 4403-4409.
8. L. Vayssieres, C. Sathe, S. M. Butorin, D. K. Shuh, J. Nordgren and J. H. Guo, *Adv. Mater.*, 2005, 17, 2320-+.
9. M. Fondell, T. J. Jacobsson, M. Boman and T. Edvinsson, *Journal of Materials Chemistry A*, 2014, 2, 3352-3363.
10. H. Moissan, *Comptes rendus hebdomadaires des séances de l'Académie des sciences*, 1891, 113, 726-729.
11. J. L. Peret, *Journal of the American Ceramic Society*, 1964, 47, 44-46.
12. F. V. Williams and R. A. Ruehrwein, *Journal of the American Chemical Society*, 1960, 82, 1330-1332.
13. T. L. Chu, J. M. Jackson and R. K. Smeltzer, *Journal of the Electrochemical Society*, 1973, 120, 802-806.
14. Y. Kumashiro, T. Yao and S. Gonda, *Journal of Crystal Growth*, 1984, 70, 515-518.
15. Y. Kumashiro, S. Misawa and S. Gonda, *Denki Kagaku*, 1983, 51, 217-218.
16. Y. Kumashiro and Y. Okada, *Appl. Phys. Lett.*, 1985, 47, 64-66.
17. P. Groot, J. H. F. Grondel and P. J. Vanderput, *Solid State Ionics*, 1985, 16, 95-98.
18. A. Goossens, E. M. Kelder and J. Schoonman, *Berichte Der Bunsen-Gesellschaft-Physical Chemistry Chemical Physics*, 1989, 93, 1109-1114.
19. E. M. Kelder, A. Goossens, P. J. Vanderput and J. Schoonman, *Journal De Physique*, 1989, 50, 567-574.
20. H. M. Manasevit, W. B. Hewitt, A. J. Nelson and A. R. Mason, *Journal of the Electrochemical Society*, 1989, 136, 3070-3076.
21. B. Bouhafs, H. Aourag, M. Ferhat and M. Certier, *J. Phys.-Condes. Matter*, 1999, 11, 5781-5796.
22. T. Mizutani, H. Asano, T. Nishinaga and S. Uchiyama, *Japanese Journal of Applied Physics*, 1977, 16, 1629-1633.
23. Y. Kumashiro, *J. Mater. Res.*, 1990, 5, 2933-2947.
24. O. A. Golikova, *Physica Status Solidi a-Applied Research*, 1979, 51, 11-40.
25. R. J. D. Tilley, in *Understanding Solids*, John Wiley & Sons, Ltd, 2005, DOI: 10.1002/0470020849.ch15, pp. 473-490.
26. L. I. Berger, *Semiconductor Materials*, CRC Press, 1996.
27. G. Li, The University of Tennessee, 2013.
28. in *CRC Handbook of Metal Etchants*, CRC Press, 1990, DOI: doi:10.1201/9781439822531.ch2 10.1201/9781439822531.ch2, pp. 75-960.

29. in *Handbook of Inorganic Compounds, Second Edition*, CRC Press, 2011, DOI: doi:10.1201/b10908-2
10.1201/b10908-2, pp. 1-476.
30. R. J. Archer, E. E. Loebner, R. Y. Koyama and R. C. Lucas, *Phys. Rev. Lett.*, 1964, 12, 538-&.
31. V. A. Fomichev, I. I. Zhukova and I. K. Polushina, *J. Phys. Chem. Solids*, 1968, 29, 1025-1032.
32. S. Dalui, S. Hussain, S. Varma, D. Paramanik and A. K. Pal, *Thin Solid Films*, 2008, 516, 4958-4965.
33. C. C. Wang, M. Cardona and A. G. Fischer, *Rca Review*, 1964, 25, 159-167.
34. B. Bouhafs, H. Aourag and M. Certier, *Journal of Physics: Condensed Matter*, 2000, 12, 5655.
35. P. Rodríguez-Hernández, M. González-Diaz and A. Muñoz, *Physical Review B*, 1995, 51, 14705-14708.
36. S. Q. Wang and H. Q. Ye, *Journal of Physics: Condensed Matter*, 2002, 14, 9579.
37. L. A. Hemstreet and C. Y. Fong, *Physical Review B*, 1972, 6, 1464-1480.
38. J. I. Ejembi, I. H. Nwigboji, L. Franklin, Y. Malozovsky, G. L. Zhao and D. Bagayoko, *J. Appl. Phys.*, 2014, 116, 103711.
39. A. Goossens and J. Schoonman, *Electrochimica Acta*, 1995, 40, 1339-1344.
40. A. J. Bosman and H. J. Vandaal, *Advances in Physics*, 1970, 19, 1-&.
41. Z. Chen, T. Deutsch, H. Dinh, K. Domen, K. Emery, A. Forman, N. Gaillard, R. Garland, C. Heske, T. Jaramillo, A. Kleiman-Shwarsctein, E. Miller, K. Takanabe and J. Turner, in *Photoelectrochemical Water Splitting*, Springer New York, 2013, DOI: 10.1007/978-1-4614-8298-7_1, ch. 1, pp. 1-5.
42. in *The Physics of Solar Cells*, DOI: doi:10.1142/9781848161269_0002, pp. 17-39.
43. T. G. Deutsch, in *DOE Hydrogen and Fuel Cells Program 2014 Annual Progress Report*, 2014, pp. 48-52.
44. A. Fujishima and K. Honda, *Nature*, 1972, 238, 37-+.
45. US 4227977 United StatesFri Feb 08 01:33:53 EST 2008IFI; EDB-81-050030English, 1980.
46. J. Lee, A. Fujishima, K. Honda and Y. Kumashiro, *Bulletin of the Chemical Society of Japan*, 1985, 58, 2634-2637.
47. K. Shohno, H. Ohtake and J. Bloem, *Journal of Crystal Growth*, 1978, 45, 187-191.
48. Y. Hirai and K. Shohno, *Journal of Crystal Growth*, 1977, 41, 124-132.
49. G. L. Li, J. K. C. Abbott, J. D. Brasfield, P. Z. Liu, A. Dale, G. Duscher, P. D. Rack and C. S. Feigerle, *Appl. Surf. Sci.*, 2015, 327, 7-12.
50. M. Odawara, T. Udagawa and G. Shimaoka, *Appl. Surf. Sci.*, 2005, 244, 289-292.
51. D. S. Ginley, R. J. Baughman and M. A. Butler, *Journal of the Electrochemical Society*, 1983, 130, 1999-2002.
52. A. Goossens, E. M. Kelder, R. J. M. Beeren, C. J. G. Bartels and J. Schoonman, *Berichte Der Bunsen-Gesellschaft-Physical Chemistry Chemical Physics*, 1991, 95, 503-510.
53. B. O'Regan and M. Gratzel, *Nature*, 1991, 353, 737-740.
54. E. Schroten, A. Goossens and J. Schoonman, *Journal of the Electrochemical Society*, 1999, 146, 2045-2048.
55. J. R. McKone, N. S. Lewis and H. B. Gray, *Chem. Mat.*, 2014, 26, 407-414.
56. P. Popper and T. A. Ingles, *Nature*, 1957, 179, 1075-1075.
57. Y. L. Gu, H. G. Zheng, F. Guo, Y. T. Qian and Z. P. Yang, *Chemistry Letters*, 2002, DOI: 10.1246/cl.2002.724, 724-725.

58. Y. L. Gu, L. Y. Chen, Y. T. Qian and W. Q. Zhang, *Bulletin of the Chemical Society of Japan*, 2003, 76, 1469-1470.
59. L. Y. Chen, Y. L. Gu, L. Shi, J. H. Ma, Z. H. Yang and Y. T. Qian, *Chemistry Letters*, 2003, 32, 1188-1189.
60. X. Feng, L. Y. Shi, J. Z. Hang, J. P. Zhang, J. H. Fang and Q. D. Zhong, *Materials Letters*, 2005, 59, 865-867.
61. V. A. Mukhanov, P. S. Sokolov, Y. Le Godec and V. L. Solozhenko, *J. Superhard Mater.*, 2013, 35, 415-417.
62. J. A. Perri, S. Laplaca and B. Post, *Acta Crystallographica*, 1958, 11, 310-310.
63. *Lange's handbook of chemistry / [edited by] James G. Speight*, New York
London : McGraw-Hill Professional, New York
London, 16th ed. edn., 2005.
64. H. Sugimoto, M. Fujii and K. Imakita, *RSC Adv.*, 2015, 5, 8427-8431.
65. H. Sugimoto, M. Fujii and K. Imakita, *Nanoscale*, 2014, 6, 12354-12359.
66. R. Binions, Doctor of Philosophy, University College London, 2006.
67. B. Stone and D. Hill, *Phys. Rev. Lett.*, 1960, 4, 282-284.
68. B. G. L and S. Skolnik, Google Patents, 1951.
69. A. W. Laubengayer, D. T. Hurd, A. E. Newkirk and J. L. Hoard, *Journal of the American Chemical Society*, 1943, 65, 1924-1931.
70. A. L. Patterson, *Phys. Rev.*, 1939, 56, 978-982.
71. J. I. Langford and A. J. C. Wilson, *J. Appl. Crystallogr.*, 1978, 11, 102-113.
72. D. Williams and C. B. Carter, in *Transmission Electron Microscopy*, Springer US, 2009, DOI: 10.1007/978-0-387-76501-3_16, ch. 16, pp. 257-269.
73. T. Scientific, XPS Interpretation of Oxygen, http://xpssimplified.com/elements/oxygen.php, Accessed 11th November 2015.
74. I. M. Vitomirov, A. Raisanen, L. J. Brillson, C. L. Lin, D. T. McInturff, P. D. Kirchner and J. M. Woodall, *J. Vac. Sci. Technol. A-Vac. Surf. Films*, 1993, 11, 841-847.
75. A. B. McLean, *Surface Science*, 1989, 220, L671-L678.
76. M. Pelavin, D. N. Hendrickson, J. M. Hollander and W. L. Jolly, *The Journal of Physical Chemistry*, 1970, 74, 1116-1121.
77. S. W. King, M. French, M. Jaehnig, M. Kuhn and G. Xu, *Ecs Journal of Solid State Science and Technology*, 2012, 1, P250-P253.
78. D. N. Hendrickson, J. M. Hollander and W. L. Jolly, *Inorg. Chem.*, 1970, 9, 612-615.
79. R. Franke, T. Chassé, P. Streubel and A. Meisel, *J. Electron Spectrosc. Relat. Phenom.*, 1991, 56, 381-388.
80. T. W. Deutsch, H.; Chen, Z.; Ardo, S.; Hu, S.; Sunkara, M.; Esposito, D.; Li, Y.; Boettcher, S., in *NREL White Papers on Materials for Photoelectrochemical Water Splitting*, ed. U. DOE, Energy.gov, 2013.
81. D. M. Fabian, S. Hu, N. Singh, F. A. Houle, T. Hisatomi, K. Domen, F. Osterloh and S. Ardo, *Energy Environ. Sci.*, 2015, DOI: 10.1039/C5EE01434D.
82. J. W. Sun, C. Liu and P. D. Yang, *Journal of the American Chemical Society*, 2011, 133, 19306-19309.
83. T. Ohmori, H. Mametsuka and E. Suzuki, *Int. J. Hydrog. Energy*, 2000, 25, 953-955.

5 Conclusions and Further Work

This thesis explored three different types of water splitting device. The first experimental chapter of this thesis explored the application of TiO_2 and doped TiO_2 in one type of integrated photoelectrochemical array: the water splitting photodiode. Boron doped and boron-nitrogen co-doped TiO_2 films were deposited using chemical vapour deposition of titanium(IV) chloride, ethyl acetate, triisopropyl borate and t-butyl amine, which to the authors' knowledge is the first example of thin film B- and B,N-doped TiO_2 made using APCVD. The films were analysed using XRD and Raman spectroscopy and were crystalline TiO_2 with no additional phases present. The samples deposited at lower temperature (500 and 550 °C) were anatase and rutile at higher temperatures (600 °C). Raman spectroscopy revealed a shift in the E_g anatase band for B-doped samples, attributed to the presence of the dopant and decrease in crystallite size as compared to undoped samples. The band gap of the TiO_2 films was observed to decrease on B-doping and increase on B,N-codoping.

The composition of the films was analysed using XPS and coupled with a contraction in the unit cell observed by calculation of lattice parameters of the films, it was thought the B dopant was incorporated into the TiO_2 lattice in an O-substitutional position, and the N was doped in an interstitial position. Remarkable rates of hydrogen production were observed in the B-doped films when compared to non-doped samples as well as having more favourable photocurrent profiles, however the presence of N seemed to drastically reduce the rate of hydrogen production. It would be of interest in further work to attempt alternative dopant precursors to t-$BuNH_2$ as the composition and dopant environment of N-doped films has been shown to be highly dependent on the preparation method.[1] In light of this boron doped TiO_2 APCVD films of low cost could be manufactured on a reel-to-reel process for photodiodes, which could be used for water reduction and oxidation but nitrogen co-doping using this method is not recommended.

In the second experimental chapter, a different type of integrated array was explored: the PV-PEC tandem device. Non-doped and 'Si-doped' iron oxide films were deposited in a low temperature APCVD process using [$Fe(CO)_5$] and TEOS precursors. The non-doped films adopted the hematite structure and displayed substrate-directing

effects depending whether they were deposited on glass or FTO coated glass, which promoted orientation in the (104) and (110) planes respectively. On Si doping, the films became amorphous and a high ratio of Si incorporation was observed. From XPS studies, the chemical environment of the Fe appeared to change and it was thought an amorphous iron-silicon oxide material was formed. Photoelectrochemical measurements of the Fe_2O_3 films deposited on FTO showed moderate photocurrents of 0.4mA.cm^{-2} at 1.23 V vs NHE when tested in 1M NaOH under 1 sun irradiation.

Fe_2O_3/ a-Si tandem devices were fabricated by directly depositing Fe_2O_3 films onto triple junction solar cells using APCVD. The films were amorphous but iron was confirmed to be Fe^{3+} from XPS results. Load line analysis predicted an operating point of 0.32 mA.cm^{-1} for the device however an additional bias of ~550 mV was required to reach this. It is thought that this is due to the amorphous nature of the iron oxide film. Despite this, a photocurrent enhancement was seen for the tandem device as compared to the individual components. Utilisation of this device configuration in a practical system would require further development of the iron oxide film, however this work highlights the promise of PV/ PEC cells as potentially efficient water splitting devices. It was demonstrated that the PV cell is able to boost the performance of the PEC component and that low-cost metal oxide films can be used as a replacement for catalyst films deposited electrochemically.

The final experimental chapter explored the application of boron phosphide in a photocatalyst suspension. Powders of boron phosphide were synthesised using a metathesis reaction of boron triiiodide and calcium phosphide, both selected for their relative ease of handling. The powders were confirmed to be cubic BP from PXRD and a particle size of 5 nm was calculated. XPS spectra of the powders showed a 1:1 ratio of B:P and the presence of a surface oxide was also observed. In photocatalytic tests, the BP powder showed an initial hydrogen production rate of ~68 μL.g^{-1}.hr^{-1}, which decayed to 56 μL.g^{-1}.hr^{-1} in the final hour of testing. The decrease in hydrogen production rate was thought to be attributable to the small particle size rather than an inherent instability of the BP material.

All three systems suffered from pit-falls inherent to the device type, or the photocatalyst material explored. Although the TiO_2 films employed in the water splitting photodiode were robust and outperformed similar systems in the literature, the band gap reduction on B-doping was not sufficient to obtain the ideal band gap for water

splitting, between 1.9-2.03 eV.[2, 3] It is the opinion of this author that the limitations of the wide band gap of TiO_2 will not be overcome as to achieve sufficient narrowing of the band gap, a high dopant density is required, introducing defects and recombination centres. It is unlikely that TiO_2 will find commercial application for water splitting, unless it is used as a thin protecting layer and not as a light absorber.[4] The water splitting photodiode in its simplest form is also unlikely to be used in a commercial system due to the V_{OC} limitations of using a single semiconductor for water splitting. It may be of interest to investigate multilayer photodiode devices, however selecting appropriate semiconductors with favourable band alignments and stabilities remains a challenge.

Although interesting, the PV-PEC devices fabricated were not efficient enough to warrant further exploration. Hematite suffers from too many limitations to be used in a commercial device, even when coupled with a PV cell to provide the additional bias required for water splitting. Although the utilisation of a photocatalyst top-layer in such a device results in the formation of a semiconductor-electrolyte junction which is favourable for charge carrier separation, it is much more profitable to simply employ an efficient water oxidation or reduction catalyst in such a device,[5] or to completely remove the light harvesting portion of the device from solution and connect it to an anode and cathode submerged in electrolyte in a hybrid PV+electrolyser type of system.[6]

The last, and least explored system due to time limitations probably holds the most promise. Boron phosphide has an ideal band gap for water splitting and is known to have excellent stability as a photoelectrode for water splitting.[7] Due to equipment limitations, films of boron phosphide were not able to be explored. The powders investigated were too small in diameter to provide long term stability for a practical system. Powder photocatalysts, though cheap are unlikely to be used for commercial water splitting due to the danger of generating oxygen and hydrogen in the same compartment and the additional chemical (and thus energy) input required for sacrificial water splitting.

With more time allocated, this author would explore films of BP deposited on a substrate with compatible lattice parameters. One of the major limitations of the work on thin film BP in the literature so far is that it has predominantly been deposited in Si(100) substrates which has a 16% mismatch in lattice parameter as compared to BP. Recent studies on boron phosphide for use as a solid-state thermal neutron detector showed that by using a substrate with a better matched lattice parameter, SiC which has

a {0001} basal plane which offers only 4.5% mismatch with BP {111}, high quality films could be deposited which displayed epitaxial growth at the interface.[8] A reduction in defects would improve the photocurrent output from a BP film due to a reduction in recombination at these defects. Alloying of BP with BAs could also be explored and the production of a multijunction device BP/ BP_xAs_{1-x}/ BAs would promote the high V_{OC} needed for water splitting. Boron arsenide has a band gap of 1.5 eV, similar lattice parameter to BP (0.4777 vs 0.45383 nm) and has shown to have promise as a water splitting photoelectrode.[9] In this way, a new earth abundant water splitting system is devised, which could also have application as a solar cell.

5.1 References

1. R. Asahi, T. Morikawa, H. Irie and T. Ohwaki, *Chem. Rev.*, 2014, 114, 9824-9852.
2. R. van de Krol and M. Grätzel, in *Photoelectrochemical Hydrogen Production*, eds. R. van de Krol and M. Grätzel, Springer US, 2012, vol. 102, ch. 1, pp. 3-11.
3. A. B. Murphy, P. R. F. Barnes, L. K. Randeniya, I. C. Plumb, I. E. Grey, M. D. Horne and J. A. Glasscock, *Int. J. Hydrog. Energy*, 2006, 31, 1999-2017.
4. E. Verlage, S. Hu, R. Liu, R. J. R. Jones, K. Sun, C. Xiang, N. S. Lewis and H. A. Atwater, *Energy Environ. Sci.*, 2015, 8, 3166-3172.
5. S. Y. Reece, J. A. Hamel, K. Sung, T. D. Jarvi, A. J. Esswein, J. J. H. Pijpers and D. G. Nocera, *Science*, 2011, 334, 645-648.
6. T. J. Jacobsson, V. Fjallstrom, M. Edoff and T. Edvinsson, *Energy Environ. Sci.*, 2014, 7, 2056-2070.
7. J. Lee, A. Fujishima, K. Honda and Y. Kumashiro, *Bulletin of the Chemical Society of Japan*, 1985, 58, 2634-2637.
8. G. L. Li, J. K. C. Abbott, J. D. Brasfield, P. Z. Liu, A. Dale, G. Duscher, P. D. Rack and C. S. Feigerle, *Appl. Surf. Sci.*, 2015, 327, 7-12.
9. S. J. Wang, S. F. Swingle, H. Ye, F. R. F. Fan, A. H. Cowley and A. J. Bard, *Journal of the American Chemical Society*, 2012, 134, 11056-11059.